EFFECT OF LENGTH SCALES ON MICROSTRUCTURE EVOLUTION DURING SEVERE PLASTIC DEFORMATION

by

Saurabh Basu

B. Tech., National Institute of Technology, Trichy, 2005

M.S., University of Pittsburgh, Pittsburgh, 2011

Submitted to the Graduate Faculty of

Swanson School of Engineering in partial fulfillment

of the requirements for the degree of

Doctor of Philosophy

University of Pittsburgh

2014

UNIVERSITY OF PITTSBURGH

SWANSON SCHOOL OF ENGINEERING

This dissertation was presented

by

Saurabh Basu

It was defended on

August 15, 2014

and approved by

Amit Acharya, Ph.D., Professor

Department of Civil and Environmental Engineering

Carnegie Mellon University

Bopaya Bidanda, Ph.D., Ernest E. Roth Professor

Department of Industrial Engineering

Jörg M. K. Wiezorek, Ph.D., Associate Professor

Department of Mechanical Engineering and Materials Science

Youngjae Chun, Ph.D., Assistant Professor

Department of Industrial Engineering

Dissertation Director: M. Ravi Shankar, Ph.D., Associate Professor

Department of Industrial Engineering

EFFECT OF LENGTH SCALES ON MICROSTRUCTURE EVOLUTION DURING SEVERE PLASTIC DEFORMATION

Saurabh Basu, Ph.D.

University of Pittsburgh, 2014

Effect of length scales on microstructure evolution during Severe Plastic Deformation (SPD) was studied by machining commercial purity metals: Ni 200, Oxygen Free High Conductivity (OFHC) Cu and Al 1100. By performing Orientation Imaging Microscopy (OIM) in the chips created, a switch over in microstructure evolution in small length scales was demonstrated. In this, microstructure refinement during SPD was replaced by an anomalous lack of refinement in small length scales. This switchover was found to be rampant in OFHC Cu, followed by Ni 200 but almost absent in Al 1100. It was hypothesized that the switchover is a consequence of a coupled effect of high strain gradients and small deformation volumes.

In order to quantify the switchover, flow of material in the deformation zone of machining was characterized *in-situ* using SEM based Digital Image Correlation (DIC). For doing this, a deformation stage capable of machining within the chamber of a Scanning Electron Microscope (SEM) was designed and fabricated. It was seen that OFHC Cu develops a sharp deformation zone during machining followed by a significantly more diffuse deformation zone in Ni 200 and then Al 1100. It was hypothesized that the switchover kicks in when the dimensions

of the deformation zone approach those associated with Geometrically Necessary Boundaries that form during SPD. Criteria for the aforementioned switchover based on this hypothesis were verified for Ni 200.

Effect of pre-deformation was studied by rolling Ni 200 samples prior to machining. It was seen that pre-deformation instigates the aforementioned switchover in microstructure evolution, reasons for which were discussed. A phenomenological model for predicting microstructure statistics resulting from SPD on Ni 200 in small length scales was setup. Contrary to common perception, it was shown that larger strain gradients giving rise to larger crystallographic curvatures instigate the aforementioned switchover resulting in lack of microstructure refinement.

TABLE OF CONTENTS

LIST OF TABLES

LIST OF FIGURES

PREFACE

I would like to thank the National Science Foundation – USA (award # 0856626, 1233909) and the II-VI block gift program for their generous support and funding. Special thanks are due to my adviser, Dr. M. Ravi Shankar. I have learnt so much from him, most importantly and hopefully to ask the right questions. I am also grateful to Dr. Bopaya Bidanda for his warm support. It went a long way in making me feel that I am covered. Special thanks to Professors, Dr. Jörg M.K. Wiezorek and Dr. Amit Acharya for seeing me through so many technical challenges and showing me the light each time. I am also very grateful to Dr. Youngjae Chun for his insights in applied research.

The fruition of this research to this day rests on the extended support of the machine shop at the Swanson School of Engineering. I wish to convey my dearest regards to Bob Barr and Scott McPherson for going out of their way in helping me so many times. I wouldn't have been able to finish my PhD without the support of Albert Stewart and his trust in me while I was making endless modifications to the Scanning Electron Microscope.

I wish to thank my colleagues for inspiring and supporting me in countless ways. Thank you Subhodeep Moitra (the 'guru') for turning me on to graduate school, Dr. Shashank Shekhar ('sarkar') for coming through for me even in seemingly impossible situations and to Marzyeh Moradi (morax) for so many things that made life easier.

My most heartfelt thanks go to my family (my mother and sister) for their support and encouragement and instilling a fighting spirit in me, which helped me, push through many tough times. I couldn’t have finished the work without them.

I will always be indebted to my father who motivated me to believe in myself, through good times and bad. I wish he were around to witness this.

This effort is dedicated to my mother.

1.0 INTRODUCTION

With a growing impetus for miniaturization, understanding the micro-mechanics during plastic deformation of small sized machine elements has assumed an important role. Here, decreasing volumes coupled with increasing surface areas often begin to manifest in altered material behavior whereby conventional theories break down. Such phenomena have been studied for more than a decade now and several nonconformities within the small length scale regime have been discovered. By performing several deformation experiments employing a host of deformation geometries, it has been shown that small sized specimens have larger yield strengths, which are stochastic in nature. Additionally, plastic flow in small length scales is discontinuous, the dynamics of which are governed by self-organized criticality. Apart from these, another effect arising out of imposed strain gradients has been extensively studied and shown to contribute to size-affected enhancement of strength and microstructure evolution.

The focus in these studies has primarily been on phenomena taking place in small strain regimes. A significant knowledge gap therefore exists in manufacturing relevant scenarios, commonly involving Severe Plastic Deformation (SPD) as limited progress has been made on understanding mechanical behavior and microstructure evolution during SPD in small sized samples.

Microstructure evolution during SPD involves a complex interplay dislocation generation and storage, frequently accompanied by twinning and often results in Ultra-Fine Grained (UFG)

microstructures. However, this trajectory of microstructure evolution which is common in samples with > mm^3 volumes will likely be affected by hitherto unrecognized mechanisms in μm^3 regimes. The purpose of work described in this thesis is to delineate the role played by some intrinsic (e.g. pre-strain, etc.) and extrinsic (geometrical, volumetric) parameters on microstructure evolution during SPD in small length scales. In trying to adhere to manufacturing relevant scenarios, machining (a common simple shear based manufacturing process) was chosen as the deformation geometry. Three different industry relevant polycrystalline metals were used for performing experiments: Ni 200, Oxygen Free High Conductivity (OFHC) Cu and Al 1100.

The thesis is organized in five primary sections. The first section provides an introduction to plastic deformation, familiarizing the reader with conventional and established theories of microstructure evolution/mechanical behavior during plastic deformation. This section also provides an overview of mechanics associated with machining. The second section provides a detailed description of the experimental techniques that were developed in the course of this work, along with a description of experiments performed for this work. The third section provides a detailed description of all results obtained. The fourth section discusses the results and lays out primary insights obtained from this research. The fifth section describes some possible future directions for this research.

2.0 LITERATURE REVIEW

Plastic deformation in crystalline metals predominantly takes place through the flow of linear defects called dislocations. Depending on the crystallography of the metal under consideration, dislocations are restricted to flow on certain (close packed) crystallographically defined planes in certain (close packed) crystallographically defined directions at room temperature. The planes coupled with directions constitute slip systems. For e.g., in a Face Centered Cubic (FCC) metal, there are 12 slip systems:

$\{111\}[\bar{1}10],\{111\}[10\bar{1}],\{111\}[0\bar{1}1],\{\bar{1}11\}[110],\{\bar{1}11\}[101],\{\bar{1}11\}[01\bar{1}],\{1\bar{1}1\}[110],\{1\bar{1}1\}[10\bar{1}],\{1\bar{1}1\}[011],\{11\bar{1}\}[1\bar{1}0],\{11\bar{1}\}[101],\{11\bar{1}\}[011]$,

where {hkl}[uvw] denote the {hkl} plane containing the [uvw] direction. The concentration of dislocation within a body is quantified as the dislocation density: $\rho = \frac{l_{dislocation}}{V}$, where $l_{dislocation}$ is the total length of dislocations within the body and V is the volume of the body. A fully annealed metallic body which has not undergone any plastic deformation features dislocation densities between 10^{13} m^{-2} and 10^{14} m^{-2}. However, upon progressive imposition of plastic deformation, dislocation densities increase and saturate at ~ 10^{16} m^{-2}.

Microstructure of the material evolves during SPD by a complex interplay of dislocations involving accumulation, storage and annihilation [1, 2]. This directly affects the mechanical behavior of the material, which shows distinct flow curve characteristics depending on the amount of strain imposed. Based on the underlying microstructure evolution mechanics at play,

the flow curve of a material is therefore often demarcated within stages I through IV (sometimes V), signifying four (five) distinct behavioral regimes [1] (Fig. 1a). These behaviors manifest in different strain hardening rates Fig. 1b. At room temperature, imposition of SPD often results in a UFG (nano-crystalline) microstructure featuring mean grain sizes < 1000 nm (< 100 nm). Some established mechanisms of microstructure evolution in FCC metals are described in this section, focusing on each stage separately.

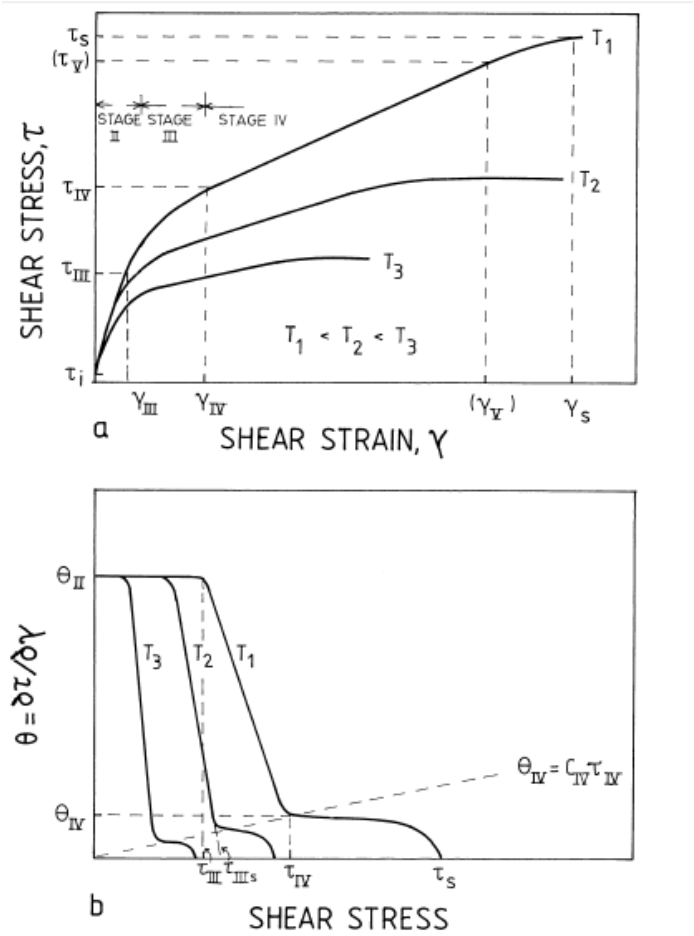

Figure 1: Schematic of (a) stress vs. strain and (b) strain hardening vs. stress curves for FCC metals [1].

2.1 STAGES OF MICROSTRUCTURE EVOLUTION

2.1.1 Stage I

Stage I refers to the onset of plastic deformation in single crystals and is accommodated by dislocations flowing on only one activated slip system. This stage is often called 'easy glide' because of limited dislocation interaction and small work hardening coefficient ($\sim G/10000$) where G is the shear modulus. Note that work hardening in this stage is often ignored [1]. The onset of plastic deformation in polycrystalline metals however happens through stage II (described next). The slip system that is activated in stage I has the highest Cross Resolved Shear Stress (CRSS) where CRSS is defined as the stress acting on the corresponding slip plane in the respective direction. Stage I of plastic deformation naturally leads into stage II when the CRSS on other slip systems rises and they are activated.

2.1.2 Stage II

Multiple slip systems are activated in stage II of plastic deformation and linear strain hardening is observed. A near universal strain hardening coefficient of ($\sim G/200$) is seen across many metals (including common FCC materials, *e.g.* Ni, Cu, Al, etc.) [1]. Due to interacting dislocations across different slip systems, dislocation tangles are formed in stage II of plastic deformation. The progressive formation of such tangles during the imposition of plastic deformation obstructs the flow of dislocations necessitating an increase in the flow stress to

sustain plastic flow. When a threshold stress is reached, dislocations begin to cross-slip which is believed to mark the initiation of stage III [1].

2.1.3 Stage III

Apart from the previously noted activation of cross-slip marking its initiation, stage III also features formation of dislocation cells. Cells refer to domains within a crystal (of size δ) that are surrounded by boundaries that are composed of dislocations. Cell boundaries therefore feature high dislocation density, whereas cell interiors feature low dislocation densities. There is some evidence that suggests that cross slip plays an important role in the formation of dislocation cells [3]. Stage III also features parabolic hardening which implies a decreasing hardening rate with increasing amounts of imposed effective strains. This decrease in hardening rates is caused by cross slip events which are an easier energetic route to sustain plastic deformation. Because cross slip events are thermally activated, deformation mechanics in Stage III is heavily influenced by the prevalent thermo-mechanics (temperature and strain rate).

2.1.4 Stage IV

The predominant feature of stage IV plastic deformation is a linear hardening rate, albeit much smaller in magnitude than in stage II ($\sim 2\times10^{-4}G$). Additionally, the work hardening rate in Stage IV is linearly dependent on the flow stress of the material undergoing plastic deformation. By the end of stage III, a well-defined dislocation cell-structure forms in the volume undergoing plastic deformation. Through stage IV, this cell-structure undergoes further refinement whereby the dislocation cell size δ becomes smaller progressively, with the imposition of strain [2].

It must be noted that the dislocation annihilation rate continues to increase through the deformation history of a FCC metal with increasing dislocation densities [2]. These events are probabilistic and refer to dislocations of opposite signs coming close and annihilating each other. This has important consequences on the evolving dislocation cell size because of the principal of similitude which imposes $\delta\sqrt{\rho_i} = Const.$ where ρ_i is the mobile dislocation density within the cells [1]. The principle of similitude implies that an increase of dislocation density in the volume undergoing deformation will effectively result in a decrease in the cell size. However, an increasing dislocation density must simultaneously result in an increasing annihilation rate, implying an increase in the cell size. Therefore, at some point during imposition of SPD (within stage IV), the rate of decrease of dislocation cell size due to increasing dislocation densities matches rate of its increase due to annihilation of dislocations [2]. This results in a saturation of the mean dislocation cell size whereby no further evolution of the dislocation cell structure results beyond this point in the material's deformation history.

2.2 DISLOCATION STRUCTURES

It was mentioned in the previous section that dislocation cells begin to form at the onset of stage III in plastic deformation. Dislocation cell boundaries are composed of several different kinds of dislocation structures. This section provides a description of the various kinds of dislocation structures that form during the course of plastic deformation. Figure 2 shows a schematic of a dislocation structure.

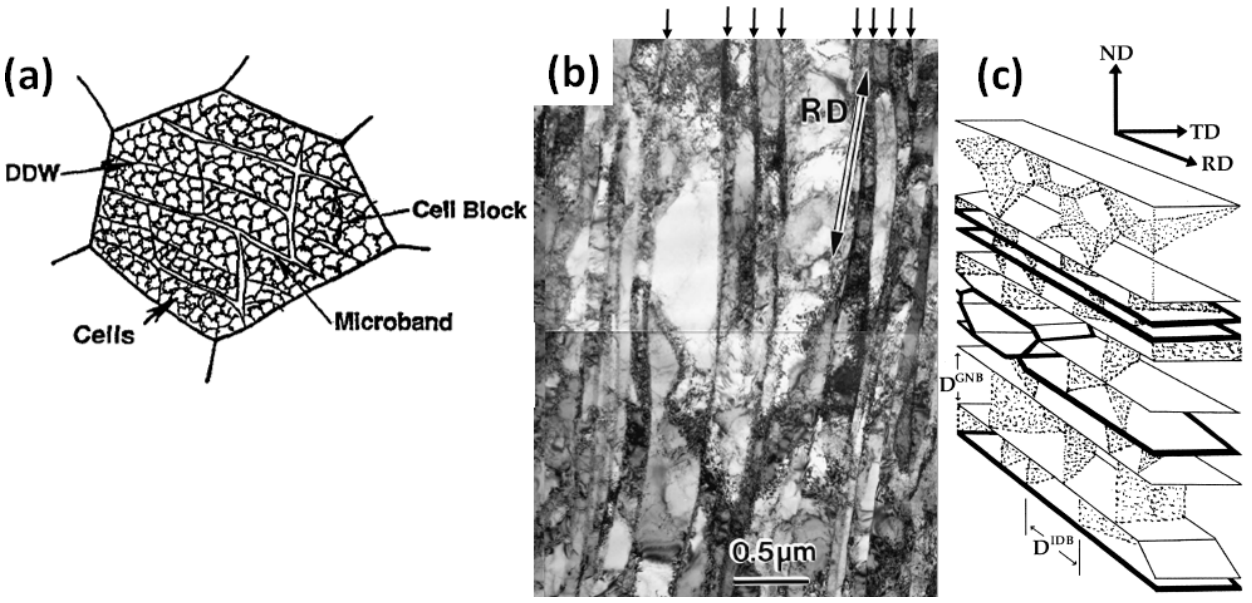

Figure 2: Dislocation structures which form in (a) Small strains and (b) Large Strains during rolling. Arrows show Lamellar Boundaries (LB). RD refers to Rolling Direction. (c) Schematic of 3D dislocation structures which format at large strains during rolling.

Dislocation boundaries are broadly classified into two types:

2.2.1 Incidental Dislocation Boundary (IDB)

IDBs are formed by mutual and statistical trapping of dislocations. The boundaries separate regions that are almost dislocation free and slightly rotated with respect to each other. The mean misorientation of IDBs rises monotonically with strain.

2.2.2 Geometrically Necessary Boundary (GNB)

GNBs are formed between two adjacent domains as a consequence of activation of different slip systems or due to activation of the same slip systems to different extents in the domains. This

often happens because of global strain gradients which might be imposed macroscopically through the employed deformation geometry. However, in several cases, strain gradients might arise internally and locally, e.g. close to hard particles in precipitate treated alloys, near grain boundaries, etc. Apart from these distinguishing features, GNBs feature a significantly larger rate of mean misorientation rise with respect to strain imposed compared with IDBs.

Progressive formation of IDBs and GNBs results in refinement of microstructure of material undergoing plastic deformation and leads to the formation of cells. With the imposition of strain, the misorientation of boundaries of the cells increases progressively. By repetition of the same process, a UFG microstructure results after imposition of SPD. There are several sub-classifications of GNBs depending on the microstructure in their neighboring regions and they are as follows:

2.2.3 Dense Dislocation Wall (DDW)

DDWs are dislocation structures that surround cell blocks. Their spatial alignments are dictated by the prevailing macroscopic deformation geometry. Cell blocks here refer to a contagious cluster of cells in which the same sets of slip systems are activated to sustain plastic flow. It must be noted that only IDBs are present within cell blocks. Therefore, it is only close to a DDW that a GNB might surround a cell block [4].

2.2.4 Lamellar Boundary (LB)

LBs are extended, nearly planar GNBs that outline a long bamboo shaped cell block and are arranged in consecutive rows, almost parallel to each other with sandwiched cell structures.

Furthermore, LBs are known to form in the direction of deformation when large strains have been imposed ($\varepsilon > 1$) [5].

2.2.5 Micro Band (MB)

MBs are plate like regions formed by two closely spaced cell blocks.

2.2.6 Sub-Grain (SG)

SGs refer to dislocation free volumes with boundaries featuring medium to high misorientation with respect to neighbors. A misorientation of larger than 2° is often used to differentiate between a cell and a sub-grain (less than 2° for the former). It is postulated that in response to the strain imposed on the volume undergoing deformation, IDBs between cells in a cell block evolve and exhibit increasing misorientation between neighboring volumes. When a sufficient misorientation is reached, these IDBs start behaving as GNBs whereby different slip systems are activated in the neighboring volumes at which point, the cells might be called SGs [6]. The classification of dislocation structures described in this section is well established by rigorous experimentation [4]. However, few attempts at first principal based modeling of the intricacies of mechanics associated with formation of several of the aforementioned dislocation structures have been made. On the other hand, phenomenological approaches are often adopted for practical reasons.

2.3 MICROSTRUCTURE REFINEMENT: DYNAMIC RECRYSTALLIZATION

The process of formation of new grains is known as recrystallization. Here grain refer to domains that are surrounded by boundaries featuring misorientation > 15˚. When recrystallization is not accompanied by plastic deformation, it is classified as Static Recrystallization (SRX) [7]. A well-known example of this process is the formation of new grains during heat treatment after deformation. However, when recrystallization happens during deformation, it is classified as Dynamic Recrystallization (DRX). Here, recrystallization may be a result of high temperatures prevalent in the material undergoing deformation (*viz.* hot deformation). In this case, new grains nucleate in regions of high local dislocation density (e.g. necklace structures in grain boundaries [7]) whereby the recrystallization process is classified as Discontinuous (Discontinuous Dynamic Recrystallization (DDRX)). However, when new grains are created as a consequence of microstructure refinement, the recrystallization process is classified as Continuous (Continuous Dynamic Recrystallization (CDRX)). CDRX has three commonly known variants which are described in the following paragraphs.

CDRX in its simplest form involves progressive formation and evolution of IDBs and GNBs. In this manner new grains are created which sub-divide further during imposition of strain, eventually resulting in UFGs. A distinguishing feature between microstructures resulting from CDRX and DDRX is the evolution of a well-defined deformation geometry based crystallographic texture in the former in contrast with a more random crystallographic texture from the latter. An example of this is Particle Stimulated Nucleation (PSN) of randomly oriented grains [8]. In-fact, this feature can been used to successfully identify whether CDRX or DDRX was active during plastic deformation. A description of crystallographic textures is provided in the next section.

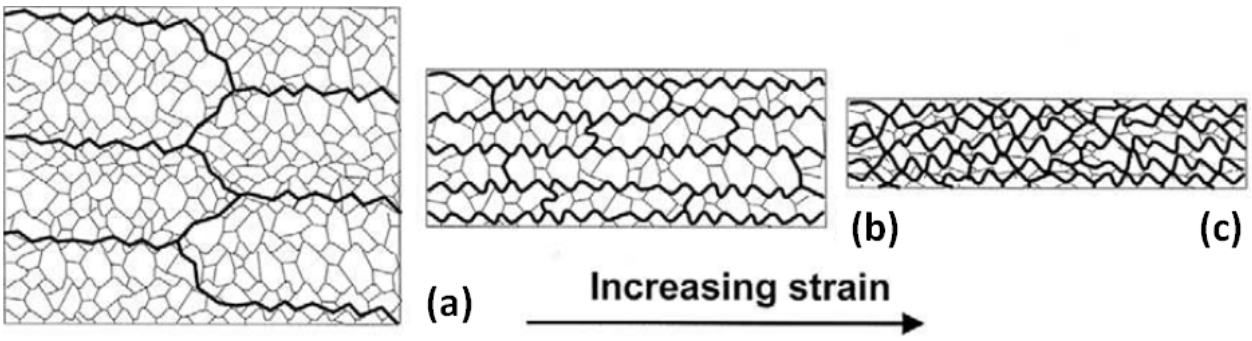

Figure 3: Geometric Dynamic Recrystallization (GDRX). By imposition of strain, the initial grain structure (a) is (b) flattened whereby Grain Boundaries on the opposite sides of the grain come closer. Serrations develop in the grain boundaries due to variation in boundary tension on GBs. When the average distance between the GBs approaches the characteristic length of the dislocation stricture, the grains pinch of into many grains.

A variant of CDRX is Geometric Dynamic Recrystallization (GDRX). As the name suggests, GDRX is morphologically driven and depends on the shape of the grains within the volume undergoing deformation. The mechanism of GDRX is illustrated in Fig. 3. Figure 3a shows a polycrystalline bulk while undergoing deformation. The shape of the workpiece changes during imposition of shear deformation as shown (Fig. 3b), resulting in flattening of the grains in the polycrystalline bulk. It must be noted that during this time, CDRX as described in the previous paragraph simultaneously results in dislocation structures, cells and sub-grains within the volume. Interplay of grain boundary tensions arising from neighboring cells, coupled with dynamic recovery of dislocation densities coaxes serrations in the boundaries of the flat grain. With the progressive imposition of shear, the grains become progressively flatter whereby the serrations on the opposite faces of the grain come close to each other. On reaching a threshold, the long serrated flat grain is pinched off in the serrations whereby several grains are created from one single flattened grain (Fig. 3c). A consequence of the geometrical nature of this variant

of GDRX is that the size of the grains resulting from the process matches closely with the mean cell size. In-fact, this criterion has been successfully utilized in quantifying the progression of GDRX across several thermomechanical conditions during SPD [9].

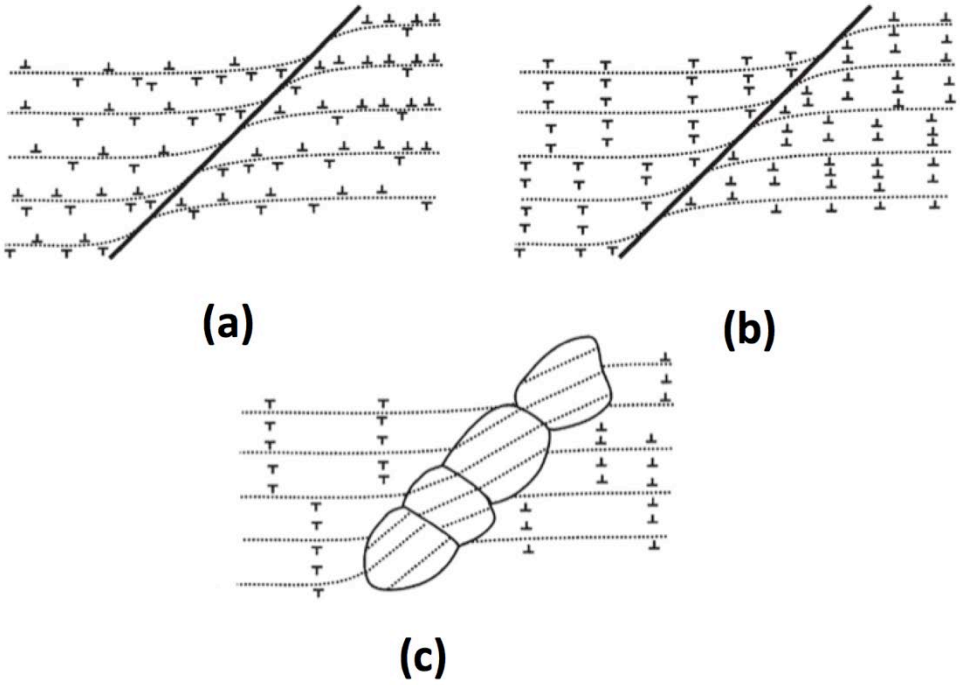

Figure 4: Rotational Recrystallization (RDRX) showing (a) inhomogeneous deformation and (b) resulting lattice rotation near Grain Boundaries and (c) subsequent formation of new grains.

The third variant of CDRX is the Rotational Dynamic Recrystallization (RDRX). Mechanism of RRX involves progressive rotation of sub-grains close to pre-existing grain boundaries whereby misorientation gradient develops between the center and the edge of a grain. This is shown in Fig 4. Progressive rotation of small segments close to the grain boundary results in a necklace structure. The mechanism is believed to be caused by inhomogeneous plasticity and dynamic recovery at grain boundaries [7]. An iteration of this mechanism results in a

homogenous UFG microstructure. This mechanism is common in geological minerals and materials where slip is restricted, e.g. in Mg where due to anisotropy, only basal slip is possible at room temperature.

Microstructure resulting from deformation is a consequence of all the different variants of DRX. Therefore, post-mortem identification of mechanism of microstructure evolution active during deformation is generally, a difficult task. However, owing to the significantly different underlying mechanism, microstructures resulting from Discontinuous and Continuous DRX can be differentiated by analyzing their crystallographic textures. The next section provides an overview of crystallographic textures and their evolution during deformation.

2.4 CRYSTALLOGRAPHIC TEXTURES

Crystallographic textures refer to non-uniform distribution of crystallographic orientations in a polycrystalline aggregate. They correspond to a distribution of points in a 3D orientation space, also known as the Orientation Distribution (OD), sometimes the Orientation Distribution Function (ODF). It should be noted that crystallographic textures result from several orientations put together and signify preferred orientations resulting from the thermomechanical history of the material under consideration.

2.4.1 Pole figures

Pole figures are 2D representations of orientation points in space. More specifically, pole figures show the 2D projection of density of the specified crystallographic orientations drawn in the 3D

Euler space. The projection may be stereographic, equal area or equal angle although the stereographic projection is used most often. Pole figures are readily empirically measurable using X Ray Diffraction and facilitate easy representation of crystallographic textures. This makes them an important tool because of ease of sample preparation for XRD when compared with other techniques of crystallographic texture analysis like OIM using Scanning Electron Microscopy (SEM) based Electron Back Scattered Diffraction (EBSD), explained in the next chapter).

2.4.2 Orientation Distribution Function (ODF)

Crystallographic textures are defined as non-uniform distributions of orientations featured by a poly-crystalline aggregate within the orientation space. One may then signify ODF as $f(g)$ where g is a point within the orientation space. Using this, the physical volume fraction of orientations containing orientations within a certain region $\Delta\Omega$ of the orientation space is given by [10]:

$$\frac{\Delta V}{V} = \frac{\int_{\Delta\Omega} f(g)dg}{\int_{\Omega_0} f(g)dg} \qquad (1)$$

It is customary to use $f(g) = 1 \forall g$ for uniform ODFs whereby $f(g)$ is also called Multiples of Random Distribution (MRD).

2.4.3 Evolution of crystallographic textures during simple shear

It was described in section 2.0 that plasticity in FCC metals takes place predominantly by flow of dislocations within the $(111)<110>$ slip systems. Simple shear crystallographic textures constitute a high concentration of (111) planes and $<110>$ directions aligned with the plane and direction of simple shear, respectively. Using this heuristic, theoretical simple shear textures can be produced as show in Fig. 5. It was seen by performing Equal Channel Angular Pressing (a simple shear based deformation process) experiments that ODF and pole figures predicted by the aforementioned heuristic matches the experimentally observed crystallographic textures very closely [11, 12].

The principal texture components which form during simple shear develop along three principal fibers. These fibers, also called the $f1$, $f2$ and the $f3$ fiber form during simple shear deformation and are indicative of simple shear type textures. The ideal locations of these fibers are indicated along the lines shown in Fig. 5. The $f1$ fiber starts from the $A_{1\theta}^{*}$ traveling through the $A_{\theta}/\overline{A}_{\theta}$ and ending at the $A_{2\theta}^{*}$ component. These components belong to the $\{111\}_{\theta}$ partial fiber which solely constitutes the $f1$ fiber. Refer Table I for the idealized locations of these components. The intensity of components distributed along the fiber are often much larger near the $A_{1\theta}^{*}$ component compared to the $A_{2\theta}^{*}$ component as seen in ODFs obtained empirically during simple shear deformation processes like ECAP [11].

The $f2$ fiber constitutes the $<110>_{\theta}$ partial fiber which includes the C_{θ}, $B_{\theta}/\overline{B}_{\theta}$ and $A_{\theta}/\overline{A}_{\theta}$ components, as well as the $\{111\}_{\theta}$ partial fiber which includes the $A_{\theta}/\overline{A}_{\theta}$ and the $A_{1\theta}^{*}$

component. The $f3$ fiber which is symmetrical with respect to the $f2$ fiber includes the C_θ, $B_\theta \diagup \overline{B}_\theta$ and $A_\theta \diagup \overline{A}_\theta$ in the $<110>_\theta$ partial fiber and the $A_\theta \diagup \overline{A}_\theta$ and the $A^*_{2\theta}$ components in the $\{111\}_\theta$ fiber.

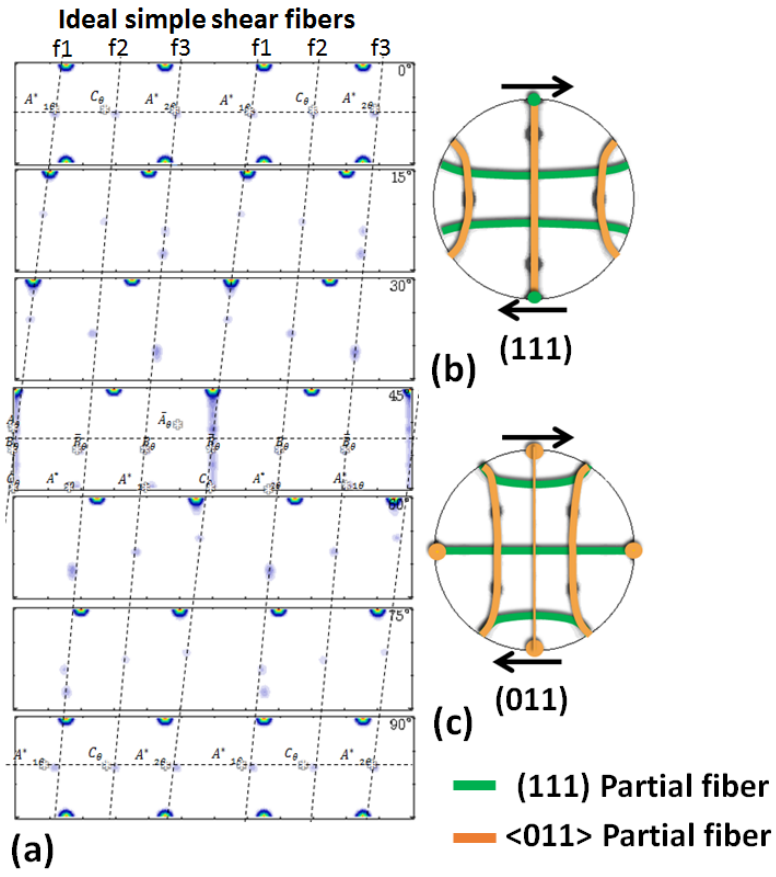

Figure 5: (a) Theoretical ideal ODF from simple shear deformation process. The dotted lines show f1, f2 and f3 fibers respectively. Corresponding (b) (111) and (c) (011) pole figure showing (111) and <011> partial fibers. Note arrows for direction of simple shear deformation.

Table I: Machining parameters and corresponding empirically measured and simulated (FEM) thermomechanical conditions of chip. Therotical estimates of temperatures using the model given in Ref. [2] are also reported.

PSM	Rake angle α	Speed V (mm/s)	Chip Strain (ε)	IR Temp. (K)	Model Temp. (K)	Chip Strain FEM (ε)	Surface Strain FEM (ε)
40L	40^o	50	2.6	324	321	3.4	3.2
40M	40^o	550	2.1	335	367	2.6	3.95
20L	20^o	50	5.9	342	346	5.9	3.6
20M	20^o	550	3.9	378	412	3.9	3.2
0L	0^o	50	8.7	322	363	12.7	5.8
0M	0^o	550	5.9	-	454	5.3	5.1

2.4.4 Evolution of crystallographic textures during rolling

Rolling is a commonly used manufacturing process, which is often approximated as compression in the Normal Direction (ND) and tension in the Rolling Direction (RD). The textures obtained during rolling have been extensively studied and detailed descriptions can be found in Ref. [10]. Owing to the aforementioned deformation geometry, rolling textures often resemble pure shear textures when looked at from the Transverse Direction (TD). Typical rolling textures are shown in Fig. 6 These textures were produced by a Visco Plastic Self Consistent model based simulation of rolling pure Cu to effective strain of 1.

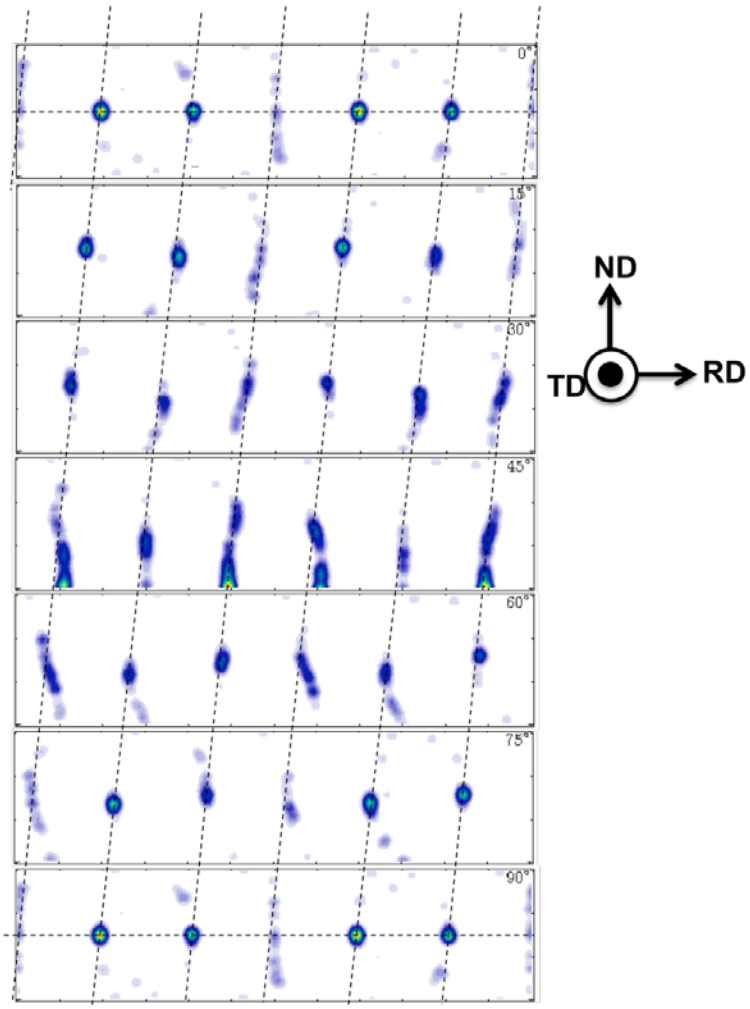

Figure 6: Rolling ODF. The inset on the right shows the physical reference orientation with respect to which the ODF is plotted.

2.5 DEFORMATION IN SMALL LENGTH SCALES

The effect of volume of deformation on mechanical behavior is often causally classified as intrinsic or extrinsic. Intrinsic size effects refer to those arising from length scales that are associated with material under consideration, e.g. precipitate size, twin spacing, grain size, mean dislocation spacing, etc. On the other hand, extrinsic size effects result from length scales that are

associated with size of the sample undergoing deformation [13]. This section provides an overview of some intrinsic and extrinsic size effects that have been shown to influence mechanical behavior and microstructure evolution during plastic deformation. For the present context, these size effects have been classified as those arising from strain gradients and those arising purely due to smaller deformation volumes, in which strain gradients do not play a role. The effect of strain gradients on microstructure evolution will be described in detail in this section due to its strong association with the work described in this thesis.

2.5.1 Size effects due to deformation volume

The effect of deformation volume on mechanical behavior of materials has been recognized for over a decade using mechanical tests on miniature samples. By performing compression tests on micro-pillars, it has been repeatedly shown that the yield strength of the materials is not an intrinsic property as classically held but is inversely proportional to the volume undergoing deformation $\frac{\sigma}{G} \propto \left(\frac{d}{b}\right)^{n}$ [14]. Here, σ is the yield strength, G is the shear modulus, d is the diameter of the pillar undergoing compression and b is the modulus of Burger's vector. The proportionality constant n has been shown to be -0.64 for FCC materials [15] and between, -0.34 and -0.80 for BCC materials in compression and tension [13]. The difference in exponents has been attributed to fundamentally different characteristics of microstructure evolution featured by the respective crystallographic families (FCC and BCC, respectively) [16]. The inverse relationship between yield strengths and size has been attributed to a number of different reasons (especially in FCC metals). In micro-pillars with diameters smaller than 1 μm, it has been shown that plasticity is dislocation nucleation governed [13]. Owing to the small volumes involved and

inherently statistical nature of dislocation networks, it is possible that micro-pillars in the aforementioned spatial regime are completely dislocation free. In such a situation, dislocations ought to be nucleated from the surface of the micro-pillars in order to sustain plastic deformation. Apart from this, it has been shown that when sample dimensions are small, dislocations tend to escape from the volume of the micro-pillars (through its surface) undergoing deformation whereby dislocation multiplication by activation of cross slip involving pinning and subsequent activation of Orowan loops does not happen.

Owing to reasons described in the previous paragraph and the Self-Organized Critical nature of dislocation systems, plastic flow has been shown to be an inherently discrete process during micro-pillar compression tests [17]. This implies that plastic flow during compression tests takes place in discrete bursts of dislocations. These bursts are interposed with intermittent elastic regimes. The magnitudes of these discrete strain bursts have been shown to be power law distributed. Additionally, it has been seen that the recorded yield strengths during plastic deformation are inherently stochastic, due to Single Armed Dislocation (SAD) sources operative within volume of micro-pillars undergoing compression where SADs refer to singly pinned dislocations [18]. Several of the aforementioned results have been verified using other deformation geometries like tension and bending [19] and the general consensus has been a strong extrinsic influence of size on mechanical behavior of materials, often summarized anecdotally as ‘smaller is stronger’.

Some work has been done on evolution of dislocation networks within small sized samples during micro-pillar experiments. By performing post-mortem Transmission Electron Microscopy (TEM) of slices from micro-pillars after compression tests, it has been shown that rate of dislocation storage increases in small sized specimens during plastic deformation [20].

Somewhat controversial results have been obtained with respect to dislocation structures that form during compression tests in micro-pillars. In samples with diameters smaller than ~ 0.5 μm, it has been shown using Laue diffraction that GNBs do not form [21]. However in larger samples (diameter > 1 μm), GNBs have been shown to form accompanied by gradual rotation of the Compression Axis [22].

It must be noted that the aforementioned discussion summarizes results obtained by imposition of moderated levels of effective strain ($\varepsilon < 0.5$). Limited work has been performed on microstructure evolution involving refinement in these studies.

2.5.2 Effects due to Strain Gradients (SGs)

In order to understand the effect of strain gradients on the ensuing mechanical behavior, we adopt a similar approach as that in Ref. [23]. Consider the following displacement field:

$$u_1 = \frac{1}{2}\kappa x_2^2, u_2 = 0, u_3 = 0$$

The displacement field is shown in in Fig. 7a. Accommodation of macroscopic displacement fields by slip planes (Fig. 7b) results in a final crystallographic state, shown in Fig.7c. No crystallographic reorientation takes place here, evident by comparing Figs.7b and 7c. However, in a different situation (Fig. 7d), accommodation of the macroscopic displacement field results in crystallographic curvature and concomitant formation of GNBs as shown in Figs. 7e and 7f. The Geometrically Necessary Dislocation (GND) density ρ results here to insure geometrical compatibility. ρ_G is often approximated as $\frac{1}{b}\frac{\partial \gamma}{\partial x}$ where b is magnitude

of the Burger's vector and $\frac{\partial \gamma}{\partial x}$ is gradient of the shear strain. GND density is often measured empirically using SEM/TEM based Orientation Imaging Microscopy (OIM).

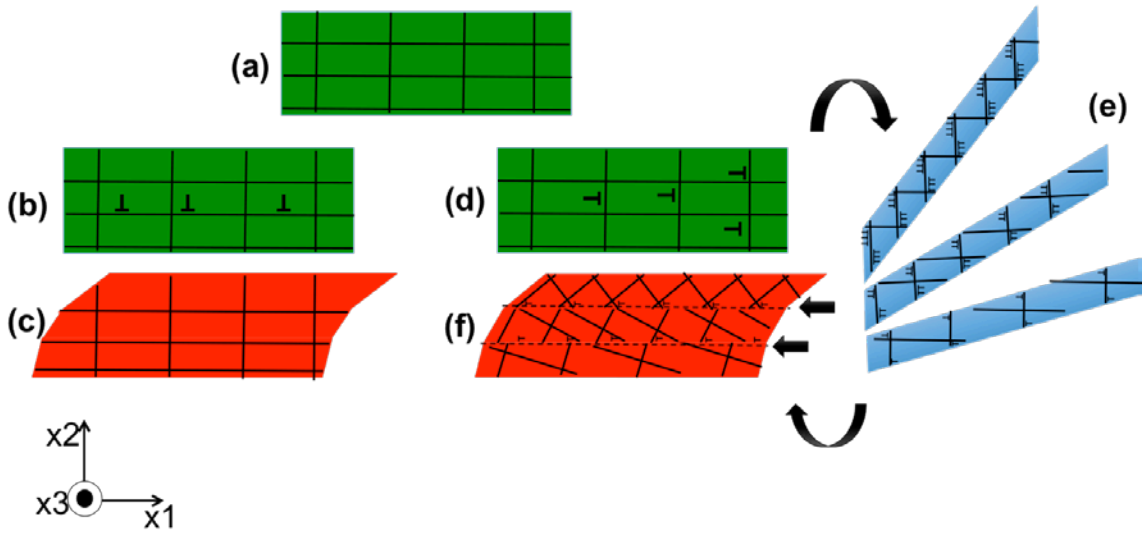

Figure 7: Microstructural state of body before deformation. (b) Accommodation of displacement field $u_1 = \frac{1}{2}\kappa x_2^2, u_2 = 0, u_3 = 0$ by flow of dislocations on horizontally oriented slip places. (c) No resulting crystallographic curvature in this case. (d) Accommodation of same displacement field by flow of dislocations in vertically oriented slip planes. (e) Intermediary state. (f) Final state showing concomitant formation of crystallographic curvature and GNBs (dotted lines pointed using black arrows). Inset on bottom left shows reference axis.

It is evident from the previous paragraph that strain gradients in a polycrystalline material will invariable results in GNDs resulting in a rise in total dislocation density. In turn this will result in enhancement of strength of the material governed by the Taylor's relation ($\sigma = \alpha G b \sqrt{\rho_G + \rho_S}$) where ρ_S refers to the Statistically Stored Dislocation (SSD) density [24]. It has also been shown that in presence of strain gradients (due to faster accumulation of GNDs), microstructure evolution involving grain refinement happens much faster [25]. Effects arising

due to SGs have been often studied using nano indentation experiments where $\rho_G \propto \frac{1}{d}$ where d is the indentation depth. Interestingly, $\sigma = \alpha G b \sqrt{\rho_G + \rho_S}$ implying $\sigma = \alpha G b \sqrt{\rho_S} \sqrt{1 + \frac{\rho_G}{\rho_S}}$ or $\sigma = \sigma_0 \sqrt{1 + \frac{\rho_G}{\rho_S}}$. This suggests that in a pre-strained material where ρ_S is larger, higher ρ_G (larger SGs) are necessary to induce an effect in the resulting mechanical behavior.

Strain gradients may arise from the imposed deformation geometry or as a consequence of the microstructure of the material undergoing deformation. For e.g. strain gradients are commonly observed in materials containing hard particles. Here, because of the enhanced GND density, rate of microstructure evolution increases in the presence of strain gradients. This has been evidence from a comparison of deformation microstructures of hard precipitate containing alloys with their solution treated counterparts [26]. Due to strain gradients in the former, microstructure evolution involving refinement was quicker in the former as opposed to the latter.

2.6 MACHINING

Machining is a deformation process involving a wedge shaped tool T (refer Fig. 8) which is advanced against a workpiece S at a speed V. When this happens, material in the regime a_0 is simply sheared in the deformation zone to form the chip. When the thickness of the workpiece (along Z) is $>> a_0$, plane strain conditions result in the deformation zone. In this case, the effective strain imposed on the material forming the chip is given by:

$$\varepsilon = \frac{\cos\alpha}{\sqrt{3}\sin\varphi\cos(\varphi-\alpha)} \tag{2}$$

where α is the rake angle of the tool and φ is the shear angle (angle between SP and X in Fig. 8). φ depends on the thermomechanical conditions prevalent in the deformation zone and the material (S) undergoing deformation and is given by:

$$\varphi = \frac{a_0/a_c \cos\alpha}{1 - a_0/a_c \sin\alpha} \tag{3}$$

The aforementioned thermomechanical conditions in turn depend on the speed (V) of tool advance and a_0. It is common to encounter SPD strains (>>1) when machining FCC metals like Cu [2], Ni [27], Al [26] and even some hard to deform materials like Ti [28]. The direction of tool advance is maintained perpendicularly with respect to its edge for machining experiments performed in this research. This geometry is chosen because it allows for a characterization of the thermomechanics of deformation via *in-situ* imaging and analytical/computational methods (Refer section 3.1). Also, this geometry remains directly relatable to that in an array of machining-processes, including milling, turning, drilling etc., which are all characterized by the removal of a preset depth of material using a wedge-shaped tool.

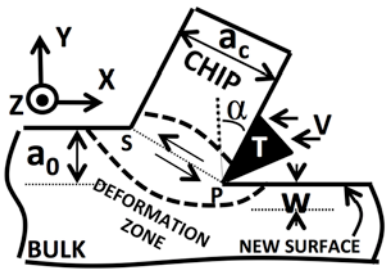

Figure 8: Schematic of the machining process.

As a consequence of the SPD imposed, material forming the chip undergoes severe refinement, featuring a UFG microstructure. Additionally, owing to the deformation geometry, the final microstructures in the chip also feature simple shear textures. The deformation zone of machining also penetrates into the workpiece underneath the tool edge, therefore leaving deformed microstructure in its wake [29, 30]. The contiguity of the deformation zones giving rise to the chip and the freshly generated surface results in microstructures being mirrored between them [28].

It must be noted that material forming the chip undergoes plastic deformation progressively as it traverses through the deformation zone due to the advancing tool. This implies existence of an associated spatial strain gradient along pathlines near the deformation zone. The amplitude of this strain gradient is inversely proportional to the thickness of the deformation zone which is conventionally approximated as $h = 0.1l$ [31] where l is the length of the deformation zone ($= \frac{a_0}{\sin \varphi}$). This implies that the amplitude of the strain gradients increase as a_0 becomes smaller. Consequently, effects arising out of strain gradients begin to play an increasingly important role as a_0 is decreased.

Additionally, when a_0 is decreased, the thickness of the deformation zone begins to approach the characteristic length associated with the dislocation structures described in section 2.2. Because of this, microstructure evolution during SPD can be expected to be significantly influenced resulting in novel mechanisms. By performing ultra-microtomy on metallic materials followed by TEM investigation of the resulting chips, it was shown that lamellar structures begin to appear on the exposed surface of the chip that were attributed to dislocation avalanche events

in the deformation zone during machining [32]. These events were hypothesized to be thermally activated due to high strain rates prevalent during machining with small a_0 values [33]. Furthermore, the morphology of dislocation structures was shown to match with the topographical features on the exposed surface of the chip. While presumably important, the implications of these lamellar features parts fabricated by machining has not been studied. Furthermore, statistics associated with these features have not been researched.

3.0 EXPERIMENTAL TECHNIQUES

(Contents from this chapter were used in other publications, proceedings and project reports.)

Several experimental methods were employed in the course of this research for deformation, simultaneous (*in*-situ) characterization and post-mortem microstructure characterization. This chapter provides a detailed description of all the experimental techniques used in this research. The author of the thesis established all experimental techniques unless noted otherwise.

3.1 MACRO-SCALE MACHINING

Macro-scale machining involving large samples with thickness > 2 *mm* and $a_0 \geq\sim 100 \mu m$ was performed in a linear slide (Baldor). The setup is shown in Fig. 9. In-situ characterization of the deformation field while performing machining was performed using Digital Image Correlation (DIC). Equivalently identified as Particle Imaging Velocimetry (PIV), DIC is an *in-situ* non-contact technique of measuring object flow. The technique relies on a source of illumination for visual recognition and tracking of the object of interest that might be in relative motion with respect to its surroundings. Illumination is derived from a light source when the associated length scales of the problem at hand are large (>~1 μm). The process is automated using software that

obtains necessary input as a sequence of digital images. This section of the dissertation provides details of the DIC technique developed/utilized in this research.

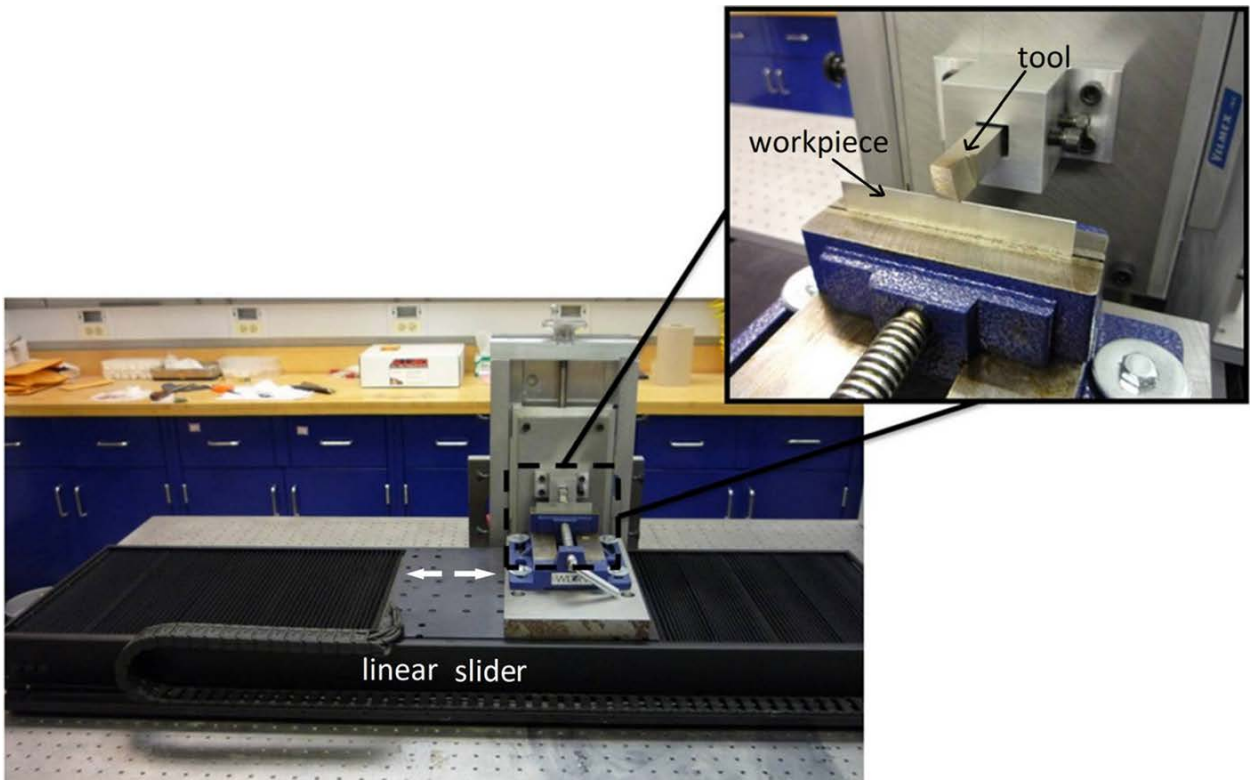

Figure 9: Linear setup for performing macro-scale machining. The open un-occluded deformation zone facilitates *in-situ* measurement of thermomechanical conditions during machining [34].

3.1.1 *In-situ* mechanical characterization

DIC was utilized for *in-situ* measurement of deformation mechanics (strain ε and strain rate $\dot{\varepsilon}$) during machining across several process parameters over a range of length scales. Here, length scales refer to the thickness of the deformation zone (h) of machining. Depending on a_0, h varies

as $l/10$ where l is the length of the deformation plane ($=a_0/\sin\varphi$, φ being the shear angle). Hardware for DIC in larger length scales ($a_0 \geq\sim 100\mu m$) included a PCO 1200 HS high speed Charged Couple Device (CCD) camera, equipped with a K2/S long working distance microscope lens for which, illumination was provided using a Cole Parmer high intensity fiber optic illuminator (part # 41723). The setup is illustrated in Fig. 10. Machining was performed in a liner configuration using a Baldor linear induction motor stage. Input was gathered for DIC by recording the flow of material close to the deformation zone during machining. The success of DIC is heavily dependent on availability of a concentrated speckle pattern in the deformation zone during machining which was enhanced by lightly spraying the side of the workpiece with black spray paint and subsequently illuminating.

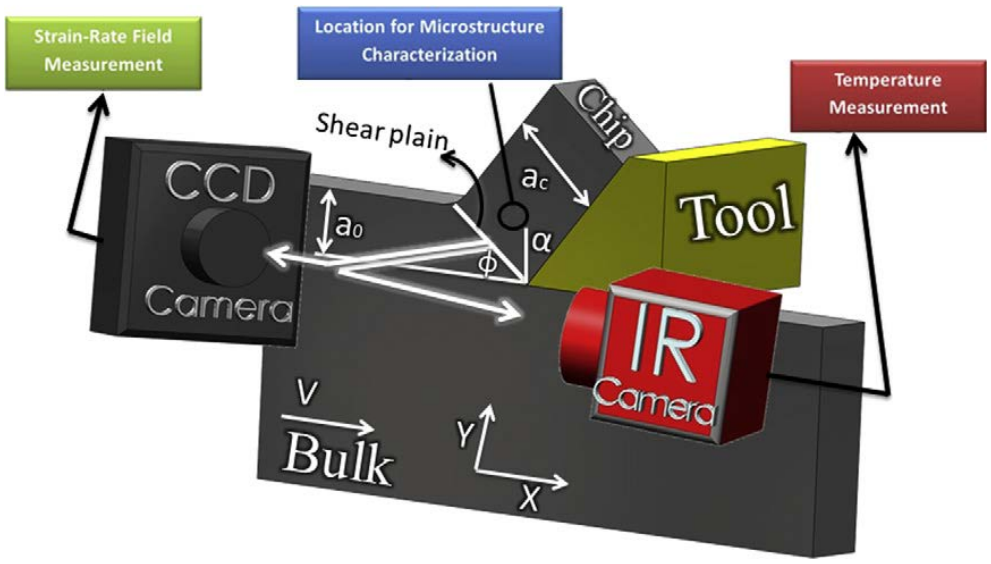

Figure 10: Setup for performing *in-situ* thermo-mechanical characterization using DIC and IR thermography. Note location of post-mortem microstructure characterization. The bulk was connected to the linear stage (Fig. 9), which was driven at speed V after engaging the tool.

3.1.1.1 Algorithm The cross correlation heuristic was used to determine the movement of asperities over an image pair within the sequence captured during machining. Cross correlation field for an image pair is defined as:

$$\Phi_k(m,n) = \sum_{j=1}^{q}\sum_{i=1}^{p} f_k(i+i_0, j+j_0).g_k(i+m, j+n) \tag{4}$$

Here, $f_k(x,y)$ and $g_k(x,y)$ represent the normalized intensities of the coordinate point (x,y) in the first and the second image of the pair k in the sequence, respectively. By finding the maxima in the correlation field $\Phi_k(x,y)$, final position of asperity in the second image (m,n) representing the asperity at (i_0, j_0) in the original image can be found. For doing this, dimensions of an interrogation window (q,p) were defined. The same procedure was repeated for a grid of points (i_0, j_0) in the original image ($f_k(x,y)$) whereby a displacement field in the region of interest was produced.

For calculating the strain rate tensor field $\underline{D}^p$, the displacement field was differentiated spatially and temporally, as $\underline{D}^p = \begin{bmatrix} \frac{\partial^2 u}{\partial x \partial t} & 1/2\left(\frac{\partial^2 u}{\partial y \partial t} + \frac{\partial^2 v}{\partial x \partial t}\right) \\ 1/2\left(\frac{\partial^2 u}{\partial y \partial t} + \frac{\partial^2 v}{\partial x \partial t}\right) & \frac{\partial^2 v}{\partial y \partial t} \end{bmatrix}$, where u and v are displacements in the X and Y (Fig. 8) directions, respectively, and ∂t represents the time between consecutive images in the sequence. Subsequently, the effective strain rate filed was calculated using the formula, $\dot{\varepsilon}^p = \sqrt{\frac{2}{3}\underline{D}^p : \underline{D}^p}$ where ':' refers to the inner product. Plane strain conditions were ensured by maintaining the thickness of the work piece (in the Z direction in Fig. 8) at $>> 10a_0$.

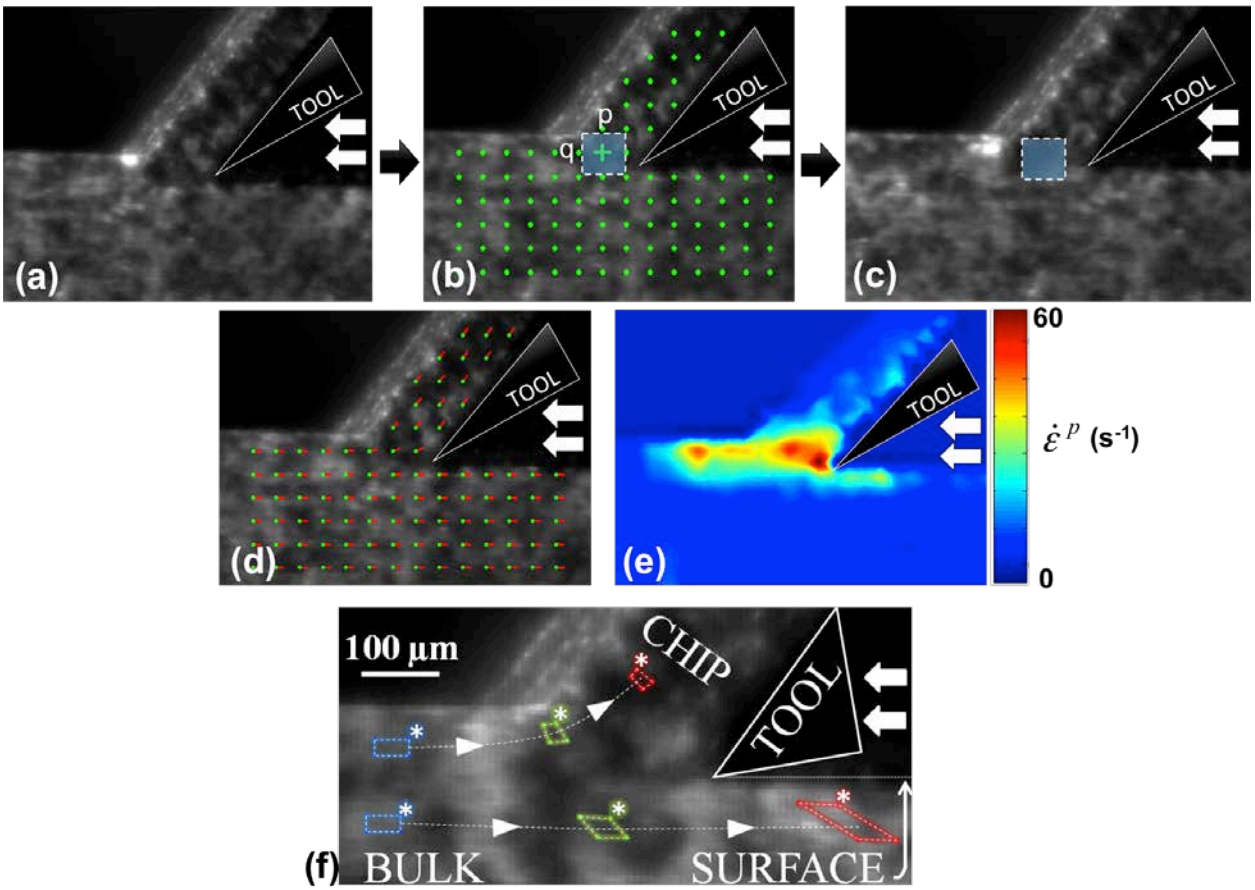

Figure 11: (a) through (c) show sequence of images acquired using high speed CCD camera. Digital Image Correlation is performed on grid of points shown in (b). For this, an interrogation window of dimension p×q was chosen around each point in the grid (blue square in (b)) and position of respective points in the next image within the sequence was found from maxima in the correlation field. For doing this, the correlation field was calculated with respect to the aforementioned interrogation window and a similar in the same location in the next image (c). Results were utilized to produce a displacement field (d), which was differentiated to find the strain rate field (e) and the material pathlines (f).

On instances in which the pathline of a material points during machining was being sought, the position of the original point was continuously updated whereby (i_0, j_0) served as the origin point for image pair k, (m,n) served as the origin point for image pair $k+1$ and so on. For calculating the effective strain ε accumulated, numerical time integration of the effective strain rate field was performed over the aforementioned pathline, given by:

$$\varepsilon = \oint_{\Gamma} \dot{\varepsilon}_p dt \tag{5}$$

where dt was the time between the image pairs in the sequence and Γ refers to the pathline and $\dot{\varepsilon}_p$ refers to the effective strain rate that the material point experience at time t in the pathline. It will be seen in the software that the *normxcorr2* function in MATLAB was used to calculate the cross correlation. Calculation of the cross correlation field is optimized in MATLAB using the fact that Equation 4 can also be interpreted as a convolution, thereby using Fast Fourier Transforms (FFT) to obtain the convolution.

3.1.1.2 Implementation This section of the chapter elucidates use of the software in order to perform DIC for obtaining displacement, strain rate and strain fields near the deformation zone during machining of Oxygen Free High Conductivity Cu at large length scales (a_0 = 150 μm). A High Speed Steel tool with a rake angle (α) =40˚ was used. The speed of advancement of the tool was V=10 mm/s. The setup described in Section 3.0 of this chapter was used for obtaining raw data for performing DIC viz. a PCO 1200 HS high speed camera for recording material flow due to the advancing tool in a sequence of images. The side of the work piece was sprayed with black spray paint followed by white light illumination by which a highly concentrated speckle pattern was obtained which facilitated the DIC. Figs. 11a through 11c illustrate the sequence of images. A grid was defined (Fig. 11b) and by performing DIC on points therein, a displacement field was composed as shown in Fig. 11d. Differentiating this displacement field, the strain rate field was produced as shown in Fig. 11e. A detailed description of the associated software implementation is given in Appendix A. The same displacement field can be utilized to find the pathlines close to the deformation zone (Fig. 11f).

3.1.2 *in-situ* thermal characterization

The protocol for in-situ thermal characterization of the deformation zone of machining was established by S. Abolghasem and theoretical details of the process can be found in Ref. [2]. The temperature field in the deformation zone was measured using calibrated Infra-Red (IR) thermography. For this, a calibration curve was first generated. This was done by coating the side of a thick Cu plate uniformly with black stove paint and then heating the plate to temperatures between 300 K and 573 K in steps of 5 K. The plate was subsequently observed with a FLIR 325A IR camera, which produced a characteristic number of counts for each temperature. A thermocouple attached to the plate was used to measure the temperature concurrently. Recording the temperature and tallying with corresponding count readings from the IR camera produced the calibration curve. Subsequently before performing machining, the side XY of the work piece (Fig. 10) was also coated with same black stove spray paint. Thereafter, IR thermography of the deformation zone was performed during machining and frames from the same were converted to temperature field using the aforementioned calibration curve. Theoretical temperature rise in the deformation zones of PSM were also calculated using Oxley's extended model [2].

3.2 EXTENSION TO SMALLER LENGTH SCALES

In order to extend the aforementioned procedure to smaller length scales, machining was performed inside the chamber of a Philips XL 30 Scanning Electron Microscope (SEM) using an apparatus designed for this (Figs. 12a, 12c, 12d). While doing this, material flow close to deformation zone of machining was recorded in a sequence of secondary electron images. As

specified previously, successful DIC entails presence of a concentrated speckle pattern in the region of interest. A low accelerating voltage (10KV) was used whereby physical asperities on the surface of the work piece would be amenable to producing sharper contrast in the secondary electron images. Machining was performed using a nominally sharp single crystal diamond tool with a rake angle $\alpha=0^{\circ}$ was used. The speed of advance of the tool was set at a low 150 μm/s to avoid thermo mechanically coupled temperature rise due to heat dissipation during plastic work.

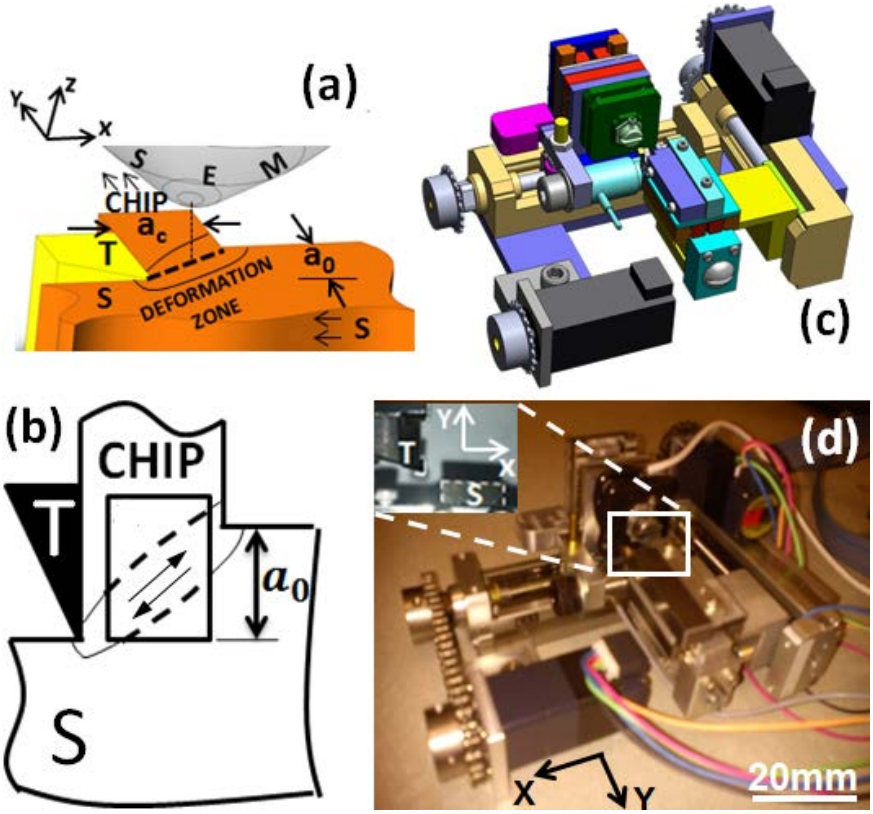

Figure 12: (a) Schematic illustrating Large Strain Machining inside the sample chamber of a Scanning Electron Microscope. Dashed line shows the location of idealized deformation plane. (b) Simple shear deformation (double arrows) during Large Strain Machining. The square refers to location on which Orientation Imaging microscopy was performed. (c) Deformation stage schematic. (d) Deformation stage assembly.

3.2.1 *in-situ* micromachining

In order to characterize material flow within the deformation zone during machining with $a_0 \leq\sim 10\mu m$, orthogonal machining was performed within the chamber of a SEM using the apparatus shown in Fig. 13. The apparatus is a general-purpose, multi-axial, micro and nano scale material manipulation and deformation device. It can be utilized inside the sample chamber of a Scanning Electron Microscope (SEM) to observe record and analyze *in-situ*, associated micro and nano-scale phenomena. The design enables detailed characterizations at high magnifications in the SEM, via *in-situ* secondary and backscattered electron imaging. The device is also capable of other imaging techniques including *in-situ* Orientation Imaging Microscopy (OIM) by Electron Back Scattered Diffraction (EBSD), etc. However, these advanced features were not used for this research.

Machining was performed on this device by first gripping the work piece with a miniature mechanical vise mounted on the device (Fig. 13). The Region of Interest (ROI) on the work piece is positioned under the electron beam of the SEM for observation using the goniometer of the SEM (Fig. 12a). The work piece is thereafter deformed by supplying power to the 2-Dimensional electronic/electrical drive mechanism of the device that imparts micro/nano motion to the work piece and/or machine tool as needed for deformation. The consequential force signature picked by the load cell (Fig. 13) is sent out through voltage lines to a computer and recorded. The device locks on to the goniometer of the SEM allowing for tilting the entire setup mandatory for some microstructural measurements (ex. ~70° for EBSD).

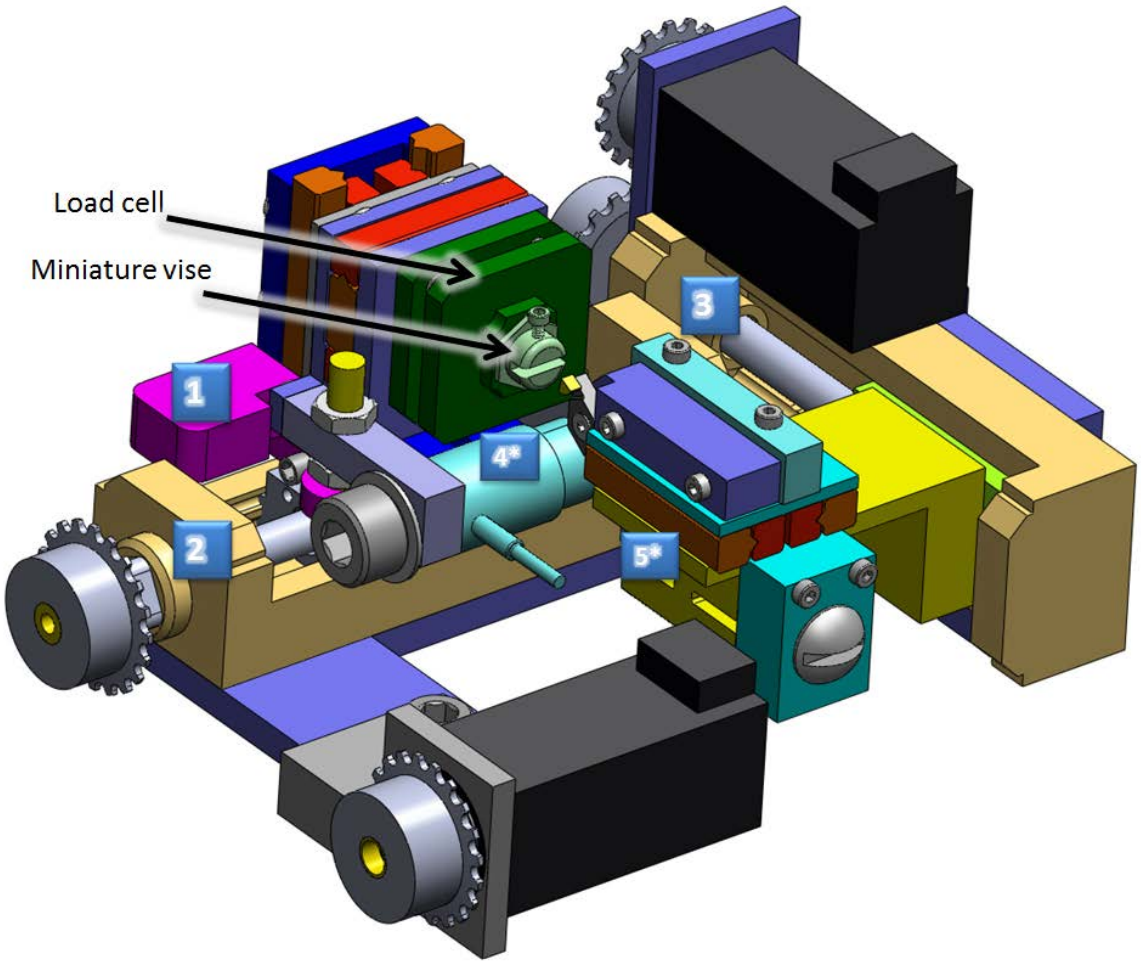

Figure 13: Schematic of micromachining device showing location of Z actuator at 1, X/Y mechanical and piezo actuators at 3/2 and 5/4, respectively.

The device chassis consists of an L shaped frame made with rigid non-magnetic steel (4004) that rests directly on the SEM goniometer when mounted (Fig. 14). Macro-scale motion of the device along the X and Y direction of the SEM goniometer was made possible by two mechanical actuators from Nippon Bearing (NB part no. BG1501A-75H/R0) that are mounted on the 'L' chassis respectively. These are driven by two stepper motors respectively from Oriental Motors (Part # CRK513PAP-H100 (Package); PK513PA-H100S (Motor); CRD5103P (Driver)). These are coupled with the NB actuators using a miniature chain and sprocket sub assembly

purchased from Stock Drive Parts/Sterling Assembly (Part # A6Y 7MM 050 (Chain); A 6X 7M1418 (X direction sprocket); A 6X 7M1420 (Y direction sprocket)).

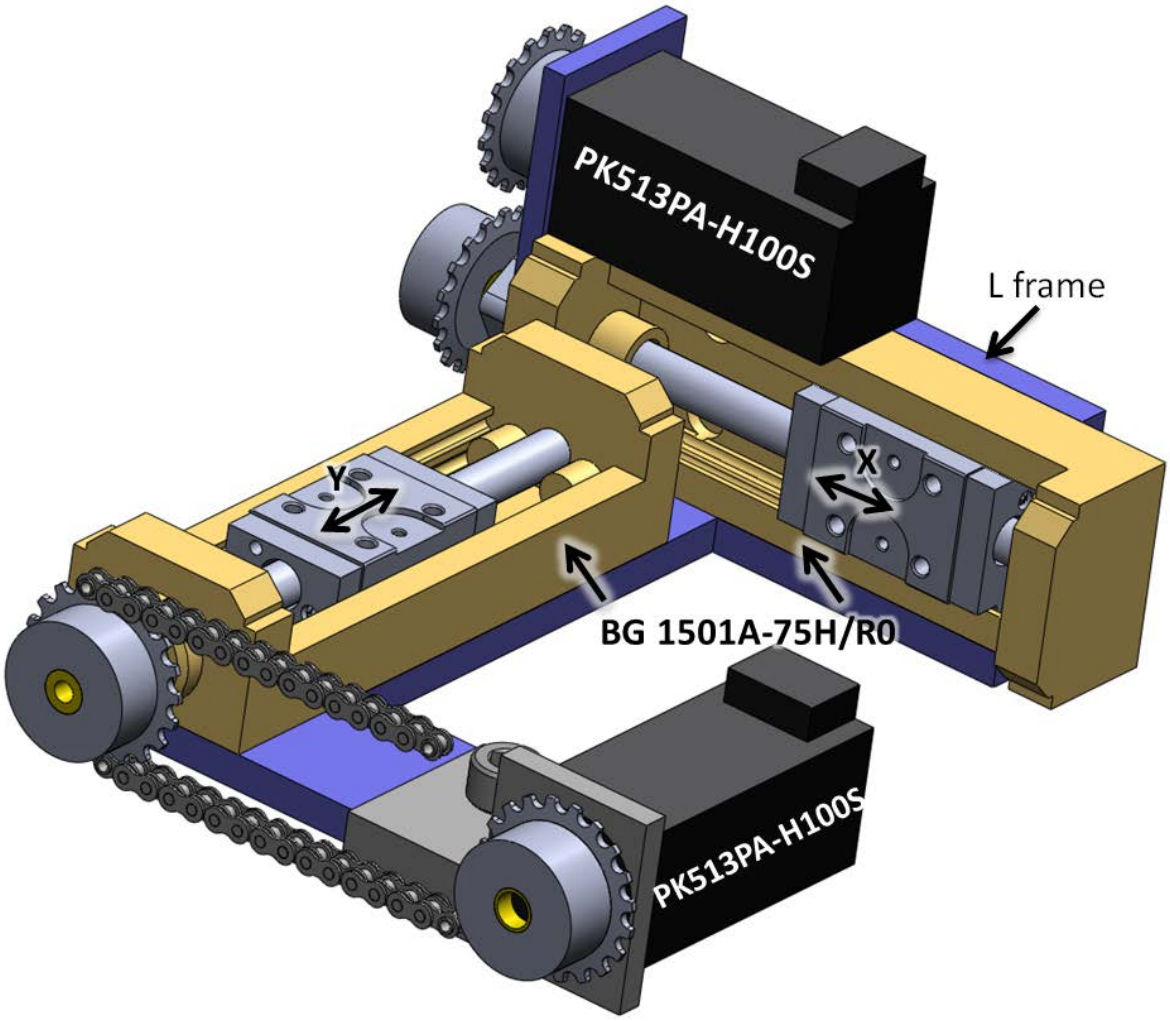

Figure 14: Schematic revealing chassis (L frame) of the micro-machining device.

The assembly is modular at three-four levels, involving different levels of features/sub-assemblies; the aforementioned forming the first level. A second level of modularity lies in the design/organization of sub-assemblies mounted on the 2 NB actuators. The Y direction sub-

assembly is devoted to positioning/control of the load cell leading to a miniature mechanical vise whereas the X axis sub assembly is meant to minister a second mechanical vise or a machine tool as needed.

The Y direction subassembly is also based on an L shaped frame made with Al alloy (6061-T6); (Fig. 15) material was chosen as a compromise between possible device rigidity and weight of the completely assembled apparatus. Mounted on this is a pair of sliders purchased from NB (Part # NV2030-5Z) along the vertical (Z) direction of the goniometer that would effectively impart a Z directional degree of freedom (DOF) to the load cell sub-assembly. This scheme of organization makes it possible to move the complete Y direction sub-assembly (including the Z degree mechanism) using a stepper motor and therefore imparts planar macroscopic YZ degree of freedom to the load cell sub assembly (Z direction motor not shown).

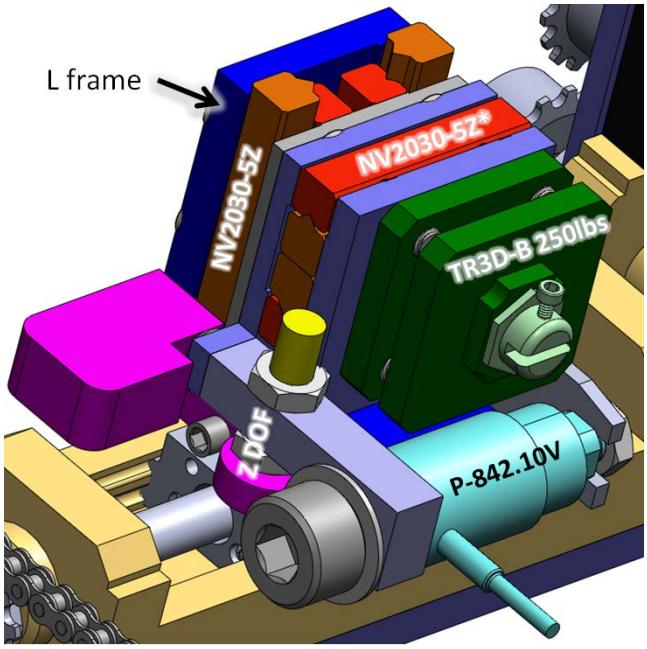

Figure 15: Y direction sub-assembly of micro machining device.

Another level of modularity in the above subassembly is devoted to microscopic motion (< 10 μm) of the vise mounted on the load cell with sub nanometer resolution along the Y direction on the aforementioned 'Z' sliders. This is achieved using a Piezo actuator purchased from Physik Instrumente (Part # P-842.10V) and another similar pair of sliders from NB (Part # NV2030-5Z*). The slider gives the extra separable relative degree of freedom needed for this microscopic motion. The load cell purchased from Michigan Scientific Corporation (Part # TR3D-B 250 lbs) is mounted on a little stage that is driven along the slides by the piezo actuator. A miniature vise is attached to the load cell for grasping the work piece for deformation and subsequent force measurements.

The X directional sub-assembly is devoted to microscopic motion (< 10 μm) of the second vise/machine tool along the X-axis of the SEM goniometer. This features a U shaped frame (Fig. 16) with one arm housing a piezo actuator (part # P-840.10V) and the second arm fastened to the 'X' NB actuator. The piezo actuator drives a miniature breadboard guided by similar NB slides. The breadboard table may be used to bolt a vise/tool holder as required for the specified deformation configuration.

Fig. 17 provides a signal chain for the micromachining device described. The specified electrical/electronic components interact with each other by using current/voltage lines that run through an electrical feed through purchased from FEI (Part # FP 6822/10). The feed through electrically links the SEM interior to its exterior where stepper motor power supplies/drivers/controllers, piezo amplifiers and user interface of the device are located.

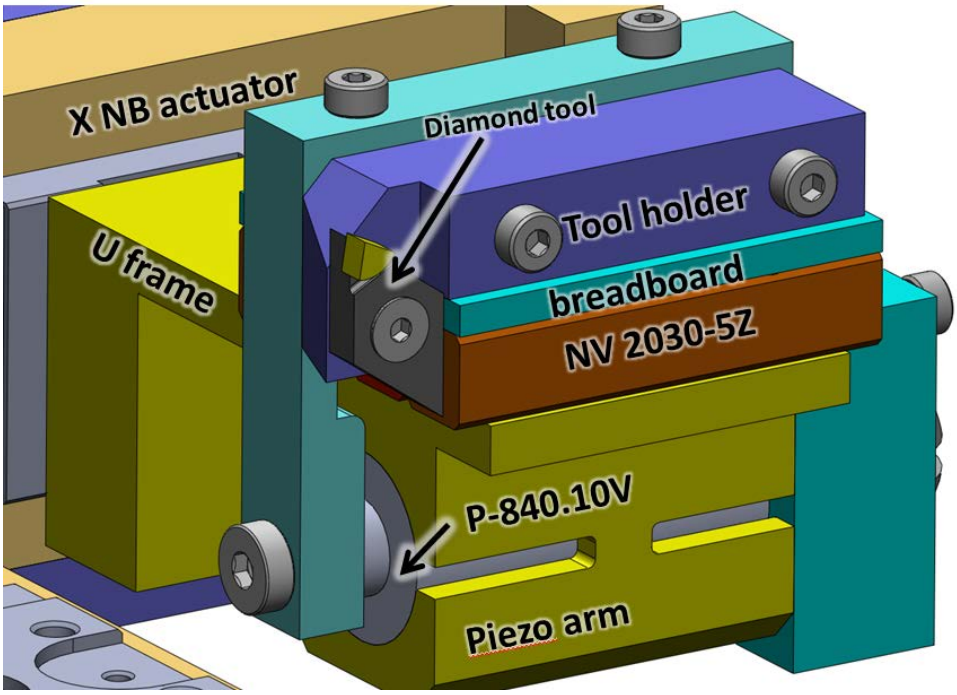

Figure 16: X direction sub assembly of micro machining device.

The stepper motors are run by a DC regulated power supply purchased from MCM electronics (Tenma Part # 72-7660) and a driver (specified above) that interfaces with a computer through a stepper motor controller by National Instruments (NI Part # NI PCI 7334) via a NI motion interface box (Part # UMI 7764). Another NI input/output board (Part # NI PCI-6014) provides the voltage input (0-10V) through a NI connector block (Part # CB-68 LP) to the piezo voltage amplifier (Part # E 501.00 (chassis), E 503.00 (amplifier)) for microscopic motion along the different axes. The load cell lines coming out of the feed through go into a NI (Part # USB 9237) high speed bridge strain measurement module. The strain gauge based load cell chosen for the original version of the device was eventually updated with a Kister 9017B piezo load cell and run with a Kistler amplifier (Part # 5010). All electrical/electronic component used in the device were eventually powered using standard 115V wall power supplies. A Graphical

User Interface has been designed for operating/controlling the different electrical systems of the device using Labview software. Labview code is described in Appendix B.

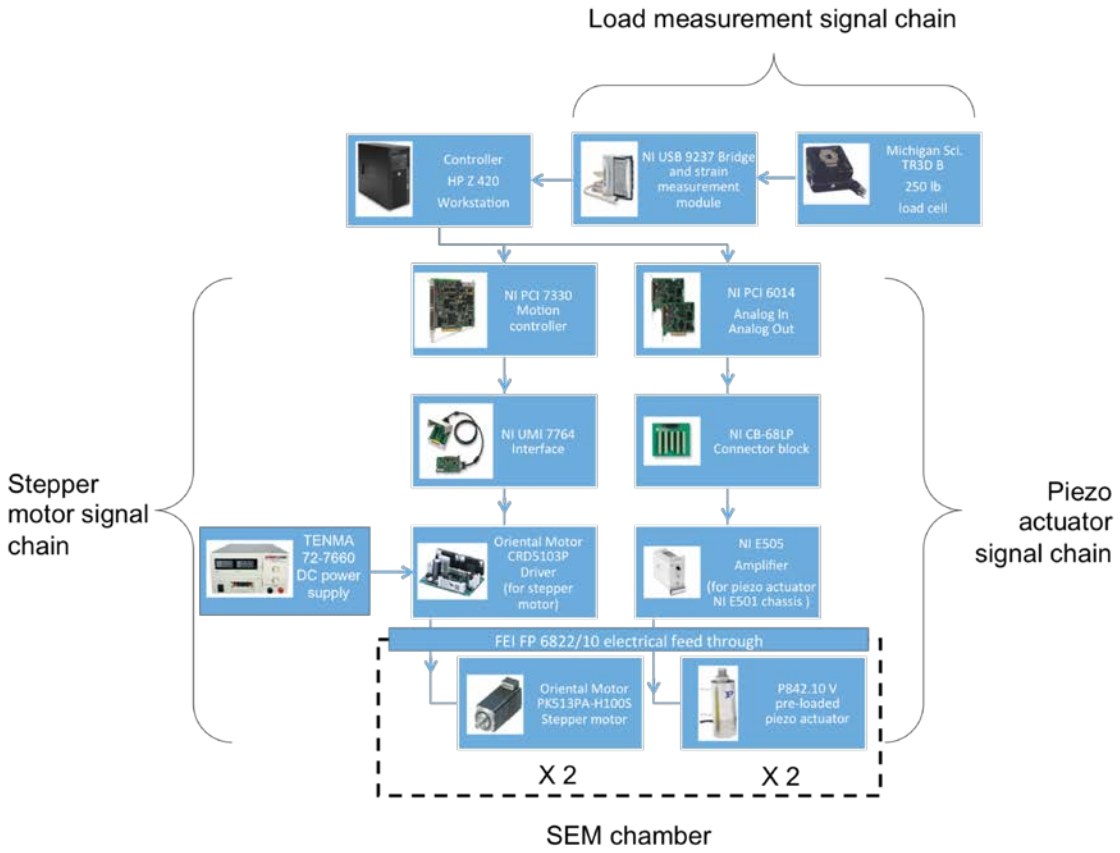

Figure 17: Signal chain for micro machining device.

3.3 ORIENTATION IMAGING MICROSCOPY (OIM)

Post-mortem orientation imaging microscopy of the chip specimens was performed using Electron Back Scattered Diffraction in a Philips XL 30 SEM equipped with a Hikari EBSD detector. Partially detached chip specimens were created by quick stop experiments while

micromachining. OIM was performed on zones equivalent to the rectangular box shown in Fig. 12b. In the configuration shown, the bottom right corner of the rectangle corresponds to material that had undergone no deformation. Therefore, microstructure in a zone close to the bottom right of the rectangle represented the un-deformed state of the work piece undergoing machining. However, the zone close to the top left in the rectangle had progressed through the deformation zone and undergone SPD in the deformation zone during machining. Therefore, OIM of a zone close to the top left would provide quantitative information about the microstructure in its evolved state following SPD. OIM of this zone spanning un-deformed and deformed microstructures would essentially provide a snapshot of microstructure evolution during machining. In addition to this, OIM from large areas within the chips created during micro machining were also obtained for insuring statistical significance. For performing OIM, partially detached chips specimens were polished mechanically to a 0.04 μm mirror finish through 15 μm, 9 μm, 6 μm, 3 μm and sometimes 1 μm finishes. Mechanical polishing was performed in a Struers. Additionally, Ni, Cu and Fe samples were also vibratory polished for several hours using 0.04 μm Alumina solution. Cu samples were also electro-polished on occasions to improve indexing. A Cu cathode in a 2:1:1 H_20, H_3PO_4, C_2H_5OH electrolyte at a potential difference of 2 V for duration of ~10 s was used for doing this. The resulting EBSD micrographs were analyzed by finding the average grain and sub-grain sizes (δ_{15° and δ_{2°) defined as domains enclosed by boundaries featuring misorientations > 15˚ and 2˚, respectively. δ_{15° and δ_{2° were calculated by finding area weighted means of grain and sub-grain sizes in the scanned EBSD micrographs. This was done using the TSL OIM 5.0 software in which $\delta_{15^\circ}/\delta_{2^\circ}$ of an individual grain/sub-grain is found by calculating the corresponding area enclosed and then finding the diameter of a circle with equal area.

3.4 DISLOCATION DENSITY USING XRD

The starting microstructure of the bulk material undergoing micro-machining was characterized using X Ray Diffraction (XRD) in a Bruker X Ray diffractometer equipped with a Lynx Eye detector having a resolution of 0.037˚. A source with X Ray Wavelength λ = 1.5406 nm was used with a scan step size of 0.03˚. The resulting scans were utilized to calculate the dislocation density ρ in the pre-LSM bulk microstructure using the method of moments. For calculating dislocation densities, the asymptotic parts of the second and the fourth moments of the $I(q)vs.q$ curve were fitted to the following pre-determined forms [35]:

$$M_2(q) = \frac{1}{\pi^2 \varepsilon_F} q - \frac{L}{4\pi^2 K^2 {\varepsilon_F}^2} + \frac{\Lambda \langle \rho \rangle \ln(q/q_0)}{2\pi^2} \tag{6}$$

$$\frac{M_4(q)}{q^2} = \frac{1}{3\pi^2 \varepsilon_F} q + \frac{\Lambda \langle \rho \rangle}{4\pi^2} + \frac{3\Lambda \langle \rho \rangle \ln(q/q_1)}{(2\pi)^4 q \varepsilon_F} + \frac{3\Lambda^2 \langle \rho^2 \rangle \ln^2(q/q_2)}{4\pi^4 q^2} \tag{7}$$

Here,

$M_k(q) = \int_{-q}^{q} q'^k I(q')dq' \Big/ \int_{-\infty}^{\infty} I(q')dq'$ where $I(q)$ is the XRD peak intensity at $q = \frac{2}{\lambda}(\sin\theta - \sin\theta_0)$ where θ_0 is the Bragg angle, θ is the diffraction angle and λ is the wavelength of the X-Ray used. The (220) X-Ray Diffraction (XRD) peak of annealed and pre-strained Ni were used for doing this (θ_0 = ~76.3˚ for (220) peak of Ni). $\langle \rho \rangle$ and $\langle \rho^2 \rangle$ are the mean dislocation density and mean squared dislocation density, respectively, K is the Scherrer constant ($K \sim 1$), ε_F is the crystallite size, q_0, q_1 and q_2 are fitting parameters.

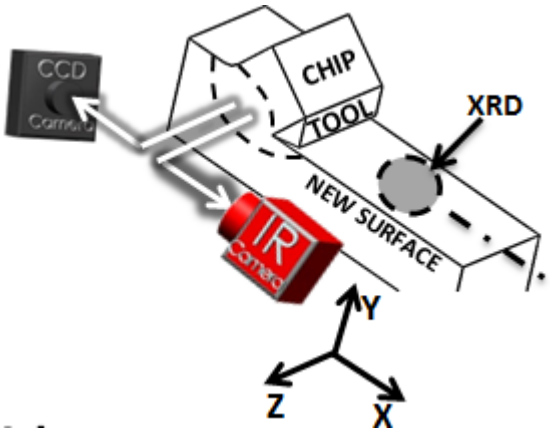

Figure 18: Schematic illustrating spatial configuration of XRD measurements.

3.5 CRYSTALLOGRAPHIC TEXTURES

Following machining, pole figure measurements were performed on the surface created using X-Ray Diffraction (XRD) in a Brueker D8 Discover system equipped with a GADDS area detector, using a Cu target producing a wavelength λ=0.157 nm. Measurements were made in the spatial configuration illustrated in Fig. 18. From this data, (111), (002) and (022) pole figures were extracted using the software Multex Area 2.0, from which Orientation Distribution Function was calculated using the freely available software 'MTEX' [36]. Pole figure measurements were also performed on the annealed bulk in order to verify initial texture of the material. Textures in the chips were found using statistically significant OIM datasets obtained using EBSD that was performed using the procedure described in the previous paragraph. Texture analysis here was performed using the 'MTEX' software.

4.0 RESULTS AND DISCUSSION

(Contents from this chapter were used in other publications, proceedings and project reports.)

The chapter provides a summary of results from experiments performed for this research. The chapter is divided in three different sections; the first relating to macro scale machining ($a_0 >\sim 100\mu m$); the second relating to micro machining ($a_0 <\sim 10\mu m$). The third section of this chapter aims to provide insight on distinctive features between material behaviors across the aforementioned length scales. Because of the varied nature of the experiments conducted for this research, each subsection in this chapter contains details explanation of the experiments conducted that are pertinent to the ongoing discussion.

4.1 MACRO-SCALE MACHINING

4.1.1 Digital Image Correlation (DIC)

Hardware and software for performing *in-situ* characterization of deformation using DIC were setup and validated by performing tension tests on dog bone shaped Al6061-T6 tensile testing specimens and measuring accumulated strain using DIC and the physical extensometer (ε = 0.05). The exercise showed a good match (within 5 %) between empirically measured and

processed ε values. Subsequently, the procedure was repeated in machining experiments and results are shown in Fig. 19.

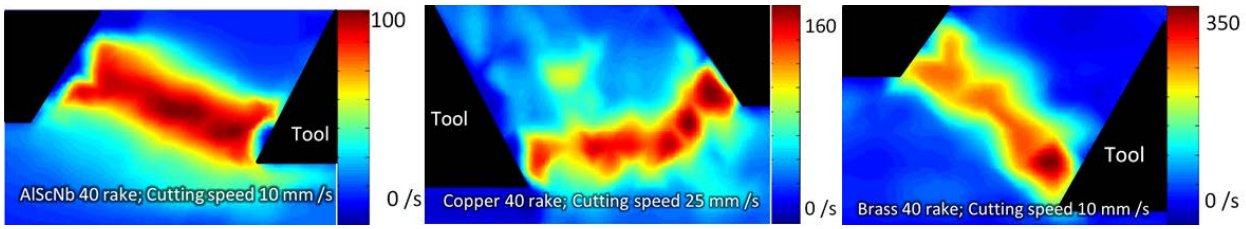

Figure 19: *in-situ* characterization of deformation zone of machining of (a) AlScNb alloy, α = 40°, V = 10 mm/s, (b) OFHC Cu, α = 40°, V = 25 mm/s and (c) 70:30 Brass, α = 40°, V = 10 mm/s. a_0 = 150 μm in all cases.

4.1.2 Crystallographic textures created during machining

In order to delineate texture evolution on the surface created during machining, Oxygen Free High Conductivity (OFHC) Copper was annealed at 973K for 2 hours and machining was performed in a linear setup. a_0 was maintained at 200 μm in all the machining experiments. Plane strain conditions were ensured by maintaining the width of the sample (in the Z direction, refer Fig. 18) at $>10a_0$ The tool rake angles α were chosen as 40°, 20° and 0° and the speeds of V=50mm/s (Low) and 550mm/s (Medium) were examined. These experimental conditions have been referred as 40L, 20M, etc. hereafter where the number in the label corresponds to the value of α and the letter corresponds to the speed of tool V (L=50mm/s (Low), M=550mm/s (Medium)). For example 20M refers to the LSM condition performed with α=20° and V=550mm/s.

4.1.2.1 Thermo-mechanical Characterization Effective strain imposed on the chip during machining was found using $\varepsilon = \frac{\sin\phi}{\sqrt{3}\sin\phi\cos(\phi-\alpha)}$ where ϕ is a function of a_0/a_c given by $\tan\phi = \frac{a_0/a_c \cos\alpha}{1 - a_0/a_c \sin\alpha}$. By measuring the value of a_0/a_c empirically, effective strain imposed on the material forming the chip was obtained. The deformation history of material in the chip and under the surface created during LSM with 40L was obtained *in-situ* using Digital Image Correlation (DIC). DIC was performed by first spraying the side plane XY of the bulk (Fig. 18) lightly with black paint whereby a concentrated speckle pattern was produced. The flow of material through the deformation zone during machining was captured in a sequence of images using a PCO 1200 HS high-speed optical camera. Subsequently, using image correlation algorithms the flow of the aforementioned speckles was quantified. Eventually, by spatially and temporally differentiating this flow and averaging, a mean deformation field of machining was created. More details of this approach can be found in Ref. [2]. Results from DIC were used to predict texture evolution in the chip and material under surface using the VPSC framework (described in Section 3.1.1). Utilizing the spatially and temporally differentiated flow field to compute a velocity-gradient tensor field generated the input for the VPSC model. This was done along pathlines that ran through the deformation zone into the chip and the freshly generated surface, which were also delineated from the high-speed images.

The temperature field in the deformation zone was measured using calibrated Infra-Red (IR) thermography. For this, a calibration curve was first generated. This was done by coating the side of a thick Cu plate uniformly with black stove paint and then heating the plate to temperatures between 300 K and 573 K in steps of 5 K. The plate was subsequently observed with a FLIR

325A IR camera, which produced a characteristic number of counts for each temperature. A thermocouple attached to the plate was used to measure the temperature concurrently. Recording the temperature from the thermocouple and tallying with corresponding count readings from the IR camera generated a calibration curve. Subsequently before performing LSM, the side XY of the work piece (Fig. 18) was also coated with same black stove spray paint. Thereafter, IR thermography of the deformation zone was performed during LSM and frames from the same were converted to temperature field using the calibration curve. Theoretical temperature rise in the deformation zones of LSM were also calculated using Oxley's extended model [2].

4.1.2.2 Simulation Simulation of texture evolution on the machined surface was performed using the Visco Plastic Self Consistent (VPSC) model [37]. The VPSC model works by simulating crystallographic texture evolution of individual grains of a microstructure assuming they are embedded in a medium that has the same mean material response as that of the individual grains combined [38]. A FORTRAN implementation of this model was employed [39] which uses a discretized ODF in the form of a collection of orientations as input. Randomly distributed orientation distribution data sets consisting of 1000 orientations each were input to the VPSC code for performing texture evolution simulations. The Voce material model for Cu was used [40]. To calibrate the VPSC model, deformation history of the chip and material under the fresh surface created during machining condition 40L (α = 40˚, V = 55mm/s, a_0 = 200 μm) were obtained from empirical measurements using DIC and IR respectively. The velocity vector fields prevalent during machining in the deformation zone were obtained from DIC and input to the VPSC code for simulating texture evolution in the chip and material under the surface, respectively. Simulated textures were then compared with empirical texture measurements and

parameters of the VPSC model were updated until a good match between observed and experimental data was obtained. Subsequently, a Finite Element Method (FEM) based numerical simulation of machining was set up. The FEM models were set up by Dr. Saradhi Koneru. An Arbitrary-Lagrangian-Eulerian (ALE) framework was used for setting up the FEM model. The machining parameters used in the FEM model were the same as described in section on material deformation. The Johnson-Cook material model for OFHC Cu was used in the FEM models. A tool edge radius of 5 μm was used in the FEM model in all cases. Thereafter, the velocity vector fields prevalent during machining were extracted from results of the FEM model. Texture evolution during machining was then simulated using these velocity vector fields in conjunction with the VPSC model and results were compared with experimental data.

4.1.2.3 Thermo-mechanical characterization-results Effective strain (ε) imparted to the material forming the chip during LSM was gauged post-mortem, empirically. This was done by measuring the ratio a_0/a_c and then using Equation 2 to calculate the value of ϕ which was then substituted into Equation 1 to calculate the value of ε. This was done for all the thermo-mechanical conditions and results are listed in Table I. Fig. 20 shows the results of mechanical characterization of the deformation zone prevalent during LSM of 40L using DIC. Using IR thermography, the corresponding deformation zone temperature fields were measured. Area averages of the temperature fields close to the center of the idealized deformation planes (SP in Fig. 20) were calculated. From this the temperature rise in deformation zone of LSM due to heat dissipated during plastic work was calculated (Table I).

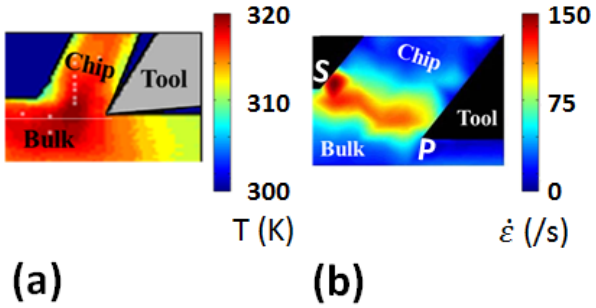

Figure 20: *in-situ* (a) thermal and (b) mechanical characterization of the deformation zone during machining of OFHC Cu with α = 40°, V = 25 mm/s and a_0 = 150 μm.

Results are illustrated in Fig. 20 for LSM with 40L. We see (in Table I) that for the same speed V of LSM, a smaller value of α corresponds to a larger value of effective strain ε in the chip. For example, chip created with the 40L, 20L and 0L condition exhibits effective strains of 2.6, 5.9 and 8.7 respectively. Furthermore, for the same value of α, increasing speed of LSM generally results in increasing temperature rise in the deformation zone. For example, 40L and 40M result in an empirically measured temperature rise of 24 K, 36 K respectively. This trend was verified by theoretical estimates of temperature rise and the two results are in reasonable agreement (Table I). Theoretical estimates of the temperature rise were calculated using Oxley's extended model [9]. Note that the apparent variation between the two at higher speeds might be an artifact of limited temporal resolution of our IR camera.

4.1.2.4 Crystallographic textures in chips created during machining Fig. 21 shows the crystallographic texture created in the chip during machining with 0L. The ODF (Fig. 21b) was calculated by performing OIM of the chip (Fig. 21a) and subsequently using a discrete binning technique with a bin size of 3˚. In line with the dominant deformation geometries known to

prevail in the deformation zone of machining, a simple shear crystallographic texture was seen in the chip. Analysis of the ODF revealed three dominant fibers, identified as the $f1$, $f2$ and $f3$. The ideal locations of these fibers are overlaid on the dashed lines for reference. These fibers are also seen in other simple shear deformation processes like ECAP [11].

Table II: Ideal orientations of texture components [12, 41].

Texture Comp.	Ideal position in orientation space			Fiber it belongs to	{*hkl*}[*uvw*]
	$\varphi 1$	Φ	$\varphi 2$		
$A_{1\theta}^{*}$	35.26 215.26	45	0 90	$\{111\}_\theta$	(111)[-1-12]
	125.26	90	45		
$A_{2\theta}^{*}$	144.74	45	0 90	$\{111\}_\theta$	(111)[11-2]
	54.74 234.74	90	45		
A_θ	0	35.26	45	$\{111\}_\theta$ <110>$_\theta$	(1-11)[110]
$\overline{A}_\theta$	180	35.26	45	$\{111\}_\theta$ <110>$_\theta$	(-11-1)[-1-10]
B_θ	0 120 240	54.74	45	<110>$_\theta$	(1-12)[110]
$\overline{B}_\theta$	60 180	54.74	45	<110>$_\theta$	(-11-2)[-1-10]
C_θ	90 270	45	0 90	<110>$_\theta$	{001}<110>
	0 180	90	45		

The $f1$ fiber starts from the $A_{1\theta}^{*}$ traveling through the $A_{\theta}/\overline{A}_{\theta}$ and ending at the $A_{2\theta}^{*}$ component. These components belong to the $\{111\}_{\theta}$ partial fiber which solely constitutes the $f1$ fiber. Refer Table II for the idealized locations of these components. The $f2$ fiber constitutes the $<110>_{\theta}$ partial fiber which includes the C_{θ}, $B_{\theta}/\overline{B}_{\theta}$ and $A_{\theta}/\overline{A}_{\theta}$ components, as well as the $\{111\}_{\theta}$ partial fiber which includes the $A_{\theta}/\overline{A}_{\theta}$ and the $A_{1\theta}^{*}$ component. The $f3$ fiber which is symmetrical with respect to the $f2$ fiber includes the C_{θ}, $B_{\theta}/\overline{B}_{\theta}$ and $A_{\theta}/\overline{A}_{\theta}$ in the $<110>_{\theta}$ partial fiber and the $A_{\theta}/\overline{A}_{\theta}$ and the $A_{2\theta}^{*}$ components in the $\{111\}_{\theta}$ fiber.

The C_{θ} was the dominant texture component in the chip created with 0L exhibiting an intensity $f(g)$ = ~21.6. $A_{1\theta}^{*}$ and $A_{2\theta}^{*}$ components were also activated with peak intensities $f(g)$ = ~12.0 and 5.0. Fig. 21 shows the pole figures that resulted in the chips created during LSM with 0L. As expected from the analysis of the ODF, the pole figures also show a dominant simple shear character. This inference was based on a comparison of these with pole figures resulting from Equal Channel Angular Pressing (ECAP, one pass [12]). This establishes a simple shear crystallographic texture evolution in the chips resulting from LSM. Analysis of the ODFs of textures on the freshly generated surface from LSM was also performed using XRD. ODFs were reconstructed from empirically measured (111), (022) and (002) pole figures on surface created during LSM using ‘MTEX’ software. Subsequently, the ODFs were rotated whereby they would coincide with the spatial reference configuration shown in the schematic inset in Fig. 18. This was done to facilitate comparison between the chip and the surface. Raw data was collected and processed using the technique described in Section 2.4.

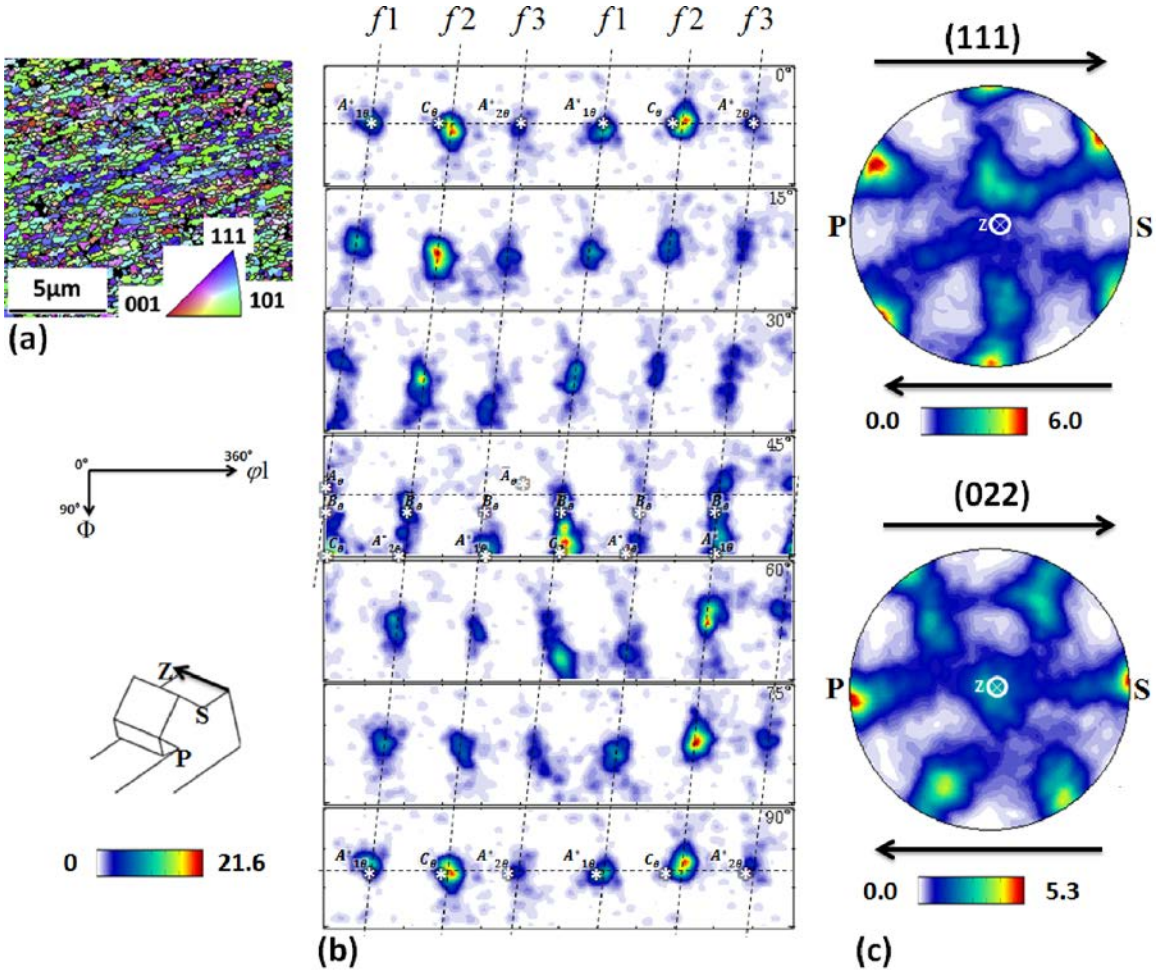

Figure 21: (a) Orientation Imaging Microscopy (OIM) of chip produced during machining with 0L. (b) $\varphi 2$ (= 0˚, 15˚, 30˚, 45˚, 60˚, 75˚ and 90˚) sections of Orientation Distribution Function (ODF) compiled from OIM with discrete binning technique (bin size: 3˚). Refer $\Phi - \varphi 1$ inset in center left and color bar in bottom left for spatial reference and scale, respectively. The ODF reveals a simple shear crystallographic texture in the chip. Dotted lines show locations of ideal $f1$, $f2$ and $f3$ fibers. (c) (111) and (022) pole figures obtained from the ODF. Refer arrows and machining schematic inset near center left for direction of simple shear and PZS axis reference, respectively.

4.1.2.5 Texture measurements and ODF analysis Figure 22 shows the pole figures collected empirically from the surface created during machining. It is evident from the figure that texture evolution follows a gradual transition across the thermomechanical conditions studied here. It

should be noted that the X Ray penetration depth of the steepest peak (with the largest Bragg angle: ~75˚ for (022)) collected for this research was ~15 μm. This penetration depth was calculated by finding the distance travelled by X Ray (originating from the Cu source) through the Cu medium, over which its intensity attenuated to 10% of its original value. Pole figures reported in Fig. 22 therefore represent the deformation-induced crystallographic textures from within ~15 μm of the surface created from machining. It will be shown that these empirical crystallographic textures are relatable to our simulations based on DIC and FEM based VPSC, respectively.

The pole figures exhibit a monoclinic (m) symmetry about the XY plane owing to the geometry of the deformation. Reconstructed and subsequently reoriented ODFs are shown in Figs. 23 and 24 in $\varphi 2$ sections with values ranging between 0^o and 90^o in steps of 15^o (Shown in $\Phi - \varphi 2$ inset in center left in Fig. 21). Here, ODFs were calculated without imposing any sample symmetry (triclinic symmetry was used).

The ODFs reveal significant concentration along preferred orientations, which fall along six fibers, which were somewhat symmetrical about the Z axis (monoclinic: $2/m$). In order to delineate simple shear components in the crystallographic textures created during machining under the surface, the following sections provide a description of the principal simple shear texture components that develop under the surface created during machining. The aforementioned texture components are described in Section 4.1.2.4 and are known to form during simple shear deformation processes.

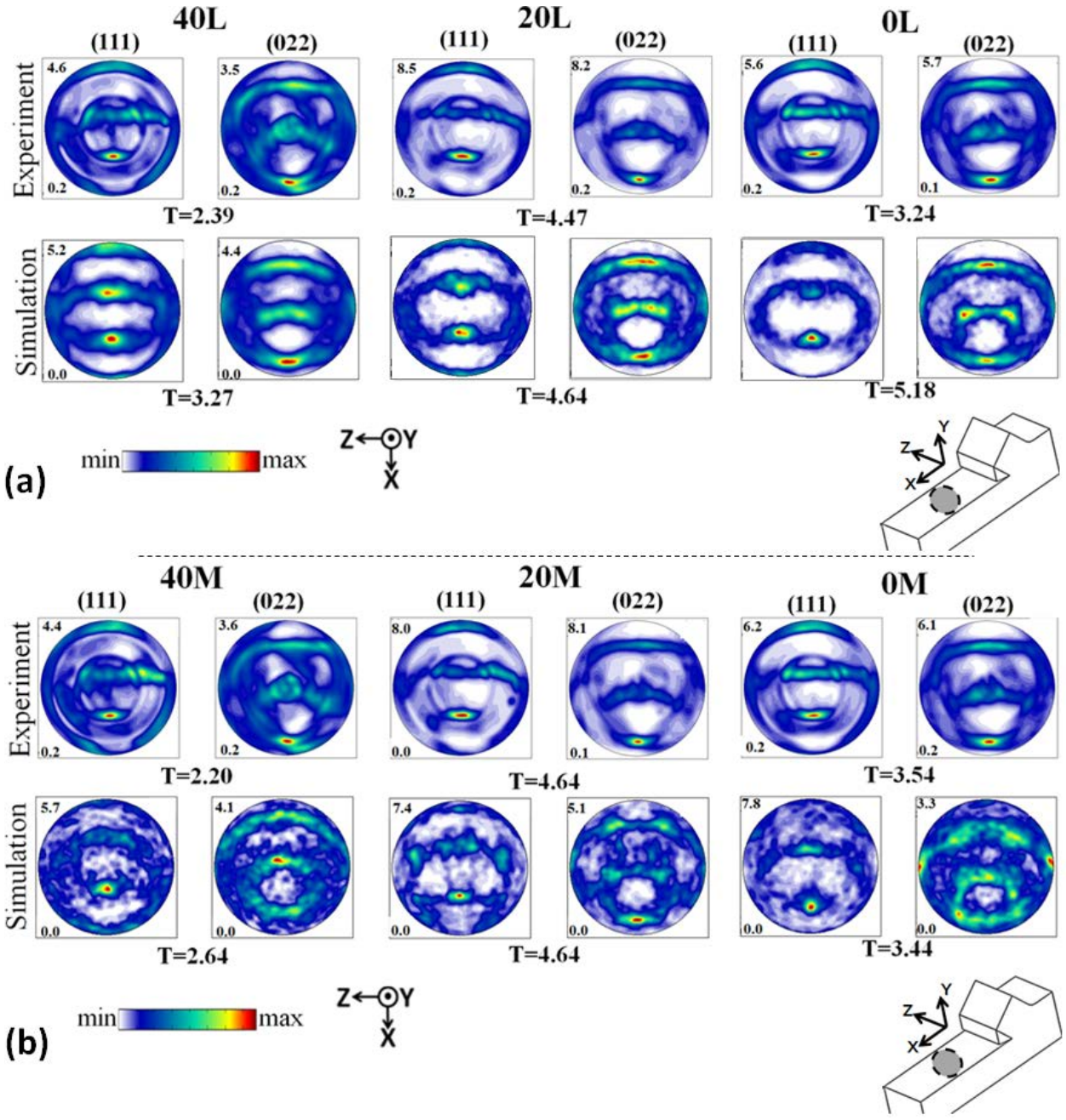

Figure 22: Empirical (111) and (022) pole figures in the surface created during machining and their simulated counterparts for speeds V= (a) 50 mm/s (b) 550 mm/s. Refer bottom left for color bar and numbers in each pole figure box (maximum: top left, minimum: bottom left) for scale. Schematic in bottom right shows spatial configuration of pole figures. (Color online)

4.1.2.6 Low (V = 55 mm/s) Fig. 23 show the ODFs of textures measured for the surface created from 40L, 20L and 0L conditions respectively. It is evident from these figures that the principal texture components, which form during machining, develop along few fibers (shown in Fig. 23 using arrows). It was seen that these fibers lie at an offset of ~15° with respect to the ideal $f1$, $f2$ and the $f3$ fibers [11] which form during simple shear deformation. $A_{1\theta}^{*}$ is the strongest component in the texture produced during machining with 40L (in $\varphi 2 = 0^{o}$), with an intensity $f(g)$ = 1.4. C_{θ} and $A_{2\theta}^{*}$ components have intensities of $f(g)$= ~2.0 and 1.2 respectively. B_{θ} and $\overline{B}_{\theta}$ exhibit negligible values of $f(g)$= ~0.1 and ~0.2 respectively. $A_{\theta}/\overline{A}_{\theta}$ components exhibit $f(g)$= ~0.8, each. Compared to 40L, 20L condition exhibits almost negligible simple shear texture components. The $A_{1\theta}^{*}$, C_{θ} and $A_{2\theta}^{*}$ feature $f(g)$ = ~0.0, 0.1, and 0.1 respectively. $A_{\theta}/\overline{A}_{\theta}$ and $B_{\theta}/\overline{B}_{\theta}$ feature $f(g)$ = ~0.0/0.8 and 0.1/0.1 respectively. Compared to 20L, 0L condition exhibits a slight intensification of the simple shear crystallographic textures with $A_{1\theta}^{*}$, C_{θ} and $A_{2\theta}^{*}$ featuring $f(g)$ = ~0.2, each. $A_{\theta}/\overline{A}_{\theta}$ and $B_{\theta}/\overline{B}_{\theta}$ feature $f(g)$ = ~0.1/0.5 and 0.1/0.1, respectively. Though manifesting smaller simple shear components when compared with those resulting from ECAP, the aforementioned textures exhibit significant texture strengths ($T = \int f(g)^{2}\, dg$) at 2.4, 4.5 and 3.2 for 40L, 20L and 0L, respectively. These observations, made from ODFs suggest absence of simple shear crystallographic textures in material under the surface created during LSM and demonstrate a heretofore-ignored distinction from the microstructure in the chip. The same can also be inferred by comparing (111) and (022) pole figures from material under the surface (Fig. 23d) with those in the chip (Fig. 21c).

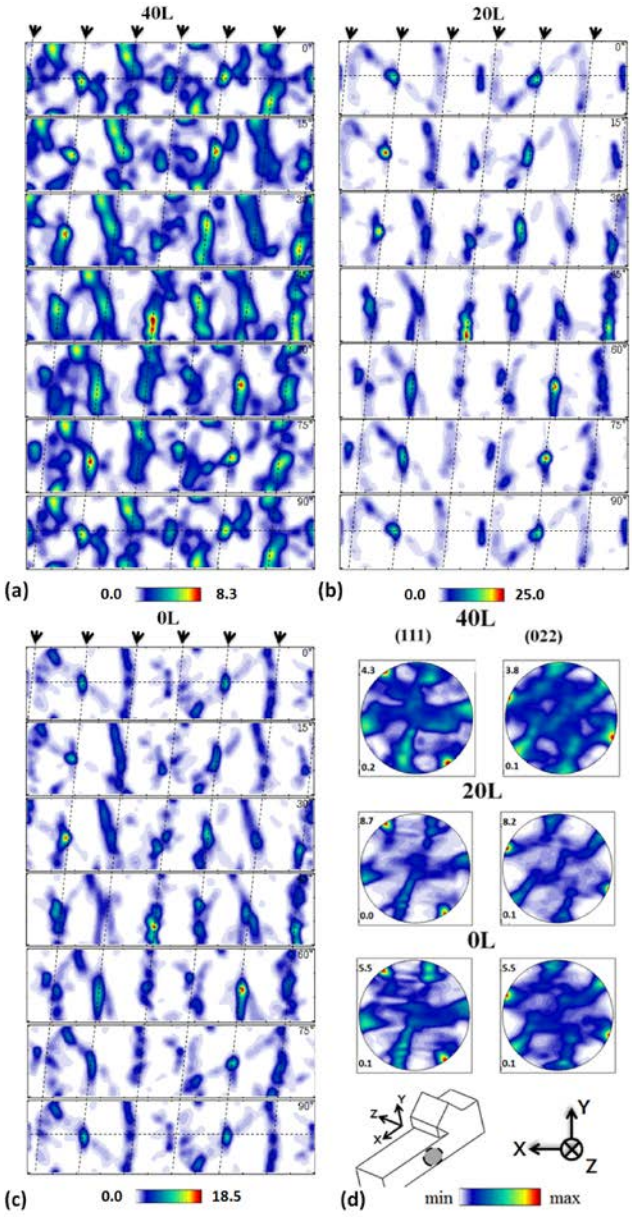

Figure 23: $\phi 2$(= 0˚, 15˚, 30˚, 45˚, 60˚, 75˚ and 90˚) sections of ODFs reconstructed from empirically collected (111), (002) and (022) pole figures in the surface created during machining with V = 50 mm/s and α = (a) 40˚, (b) 20˚ and (c) 0˚. The ODFs reveal preferred orientations along fibers (black arrows). Refer color bar under each ODF for scale. (d) Empirically collected pole figures reoriented to coincide with spatial reference shown in bottom left. Refer color bar in bottom right for scale. Numbers at top left and bottom left of each pole figure box show maximum and minimum. Schematic shows spatial configuration of the pole figures with respect to geometry of machining.

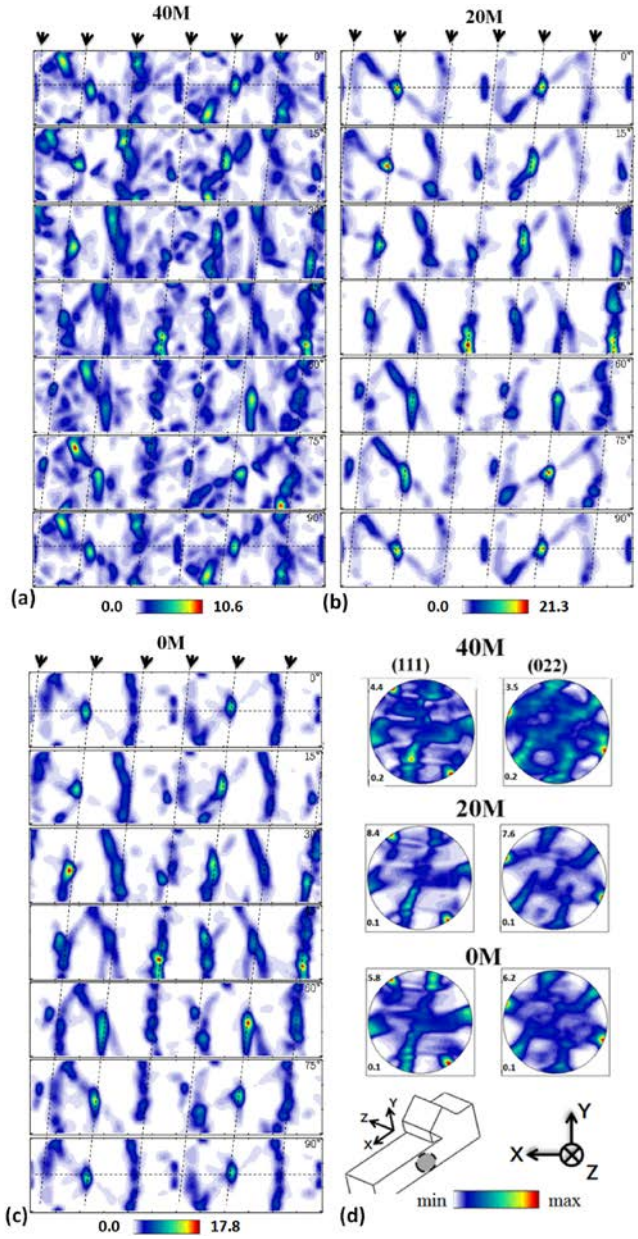

Figure 24: $\varphi 2$ (= 0˚, 15˚, 30˚, 45˚, 60˚, 75˚ and 90˚) sections of ODFs reconstructed from empirically collected (111) and (022) pole figures in the surface created during machining with V = 550 mm/s and α = (a) 40˚, (b) 20˚ and (c) 0˚. The ODFs reveal preferred orientations along fibers (black arrows). Refer color bar under each ODF for scale. (d) Empirically collected pole figures reoriented to coincide with spatial reference shown in bottom left. Refer color bar in bottom right for scale. Numbers at top left and bottom left of each pole figure box show maximum and minimum. Schematic shows spatial configuration of the pole figures with respect to geometry of PSM.

4.1.2.7 Medium (V = 550 mm/s) Fig. 24 show the ODFs of textures measured on the surface created with 40M, 20M and 0M, respectively. The textures formed during machining with V = 550 mm/s (Medium) share several characteristics with those formed during machining with V=50mm/s (Low). For e.g. the textures here are arranged along the same dominant fibers as seen during machining with V=50mm/s (Low) (Section 4.1.2.6). Additionally, the textures also exhibit monoclinic symmetry. However, compared to 40L, 40M shows a weakening in simple shear textures components with $A_{1\theta}^{*}$, C_{θ} and $A_{2\theta}^{*}$ featuring $f(g)$ = ~0.9, 0.6 and 0.6, respectively. $A_{\theta}/\overline{A}_{\theta}$ and $B_{\theta}/\overline{B}_{\theta}$ exhibit $f(g)$ = ~1.0, 1.0 and 0.1 and 0.1, respectively. Compared to 40M, 20M exhibits a similar loss of simple shear texture components as also seen across 40L-20L in Sect. 4.1.2.6. $A_{1\theta}^{*}$, C_{θ} and $A_{2\theta}^{*}$ feature $f(g)$ = ~0.0 each. $A_{\theta}/\overline{A}_{\theta}$ and $B_{\theta}/\overline{B}_{\theta}$ exhibit $f(g)$ = ~0.1 each. The 0M crystallographic texture exhibits a similarly weak simple shear components with $A_{1\theta}^{*}$, C_{θ} and $A_{2\theta}^{*}$ featuring $f(g)$ = ~0.1, 0.1 and 0, respectively. $A_{\theta}/\overline{A}_{\theta}$ and $B_{\theta}/\overline{B}_{\theta}$ exhibit $f(g)$ = ~0.1/0.6 and 0.1/0.1.

Crystallographic textures obtained from machining with V = 550 mm/s exhibit similar anomalous strengths ($T = \int f(g)^2 dg = 2.2$, 4.6 and 3.5 for 40M, 20M and 0M, respective) as observed during machining with V = 50 mm/s. Presence of non-negligible texture strengths despite the near absence of simple shear components indicates presence other crystallographic textures arising from different deformation modes which might be activated in the material under the surface during machining. After further analysis, it was seen that the ODFs obtained from the surfaces created during machining contained significant concentrations of rolling texture components. This is shown in Fig. 25 in which the simple shear and rolling components within

the ODFs have been marked. In the configuration in which ODFs in Fig. 25 are plotted, the Brass, Goss and Copper rolling components and the C_θ simple shear component were clearly perceptible. It was seen that the rolling texture components became more dominant in surfaces that were created with more negative rake angles (20º and 0º with respect to 40º). Simultaneously, with the dominance of rolling texture components, the simple shear components seemed to decrease in strength during instances of machining with more negative rake angles. Rolling texture components in the surfaces created during machining presumably manifest due the effects arising from finite edge radii of the tools used compounded with other deformation modes (e.g. compression and tension) which are known to exist under the surface during machining (ahead and in the wake of the tool, respectively). The edge radii of tools used in this research were found by Atomic Force Microscopy (AFM) by measuring the edge profiles and subsequently fitting circles to the profiles; they were found to be ~5 μm for all three rake angles (40º, 20º and 0º).

4.1.2.8 Finite Element Simulation of Machining Table I shows the effective strains predicted by the FEM model of machining in the chip and material under the surface. Simulated strains in the surface and the chip were obtained from a layer within 20 μm of the surface and from the center of the chip created during machining, respectively. We see a general agreement between the empirical and predicted strains in the chip. On the other hand, numerically predicted strains in the surface featured somewhat smaller values, albeit of the same order when compared with those in the chip. Additionally, these results revealed that the strains imposed on the material under the surface created during machining were not as sensitive to speed (V) of tool advance as those for the corresponding chips created. It will be seen that despite this, FEM model explicitly

coupled with the VPSC model appears to predict evolution of texture under the surface created during machining across different speeds.

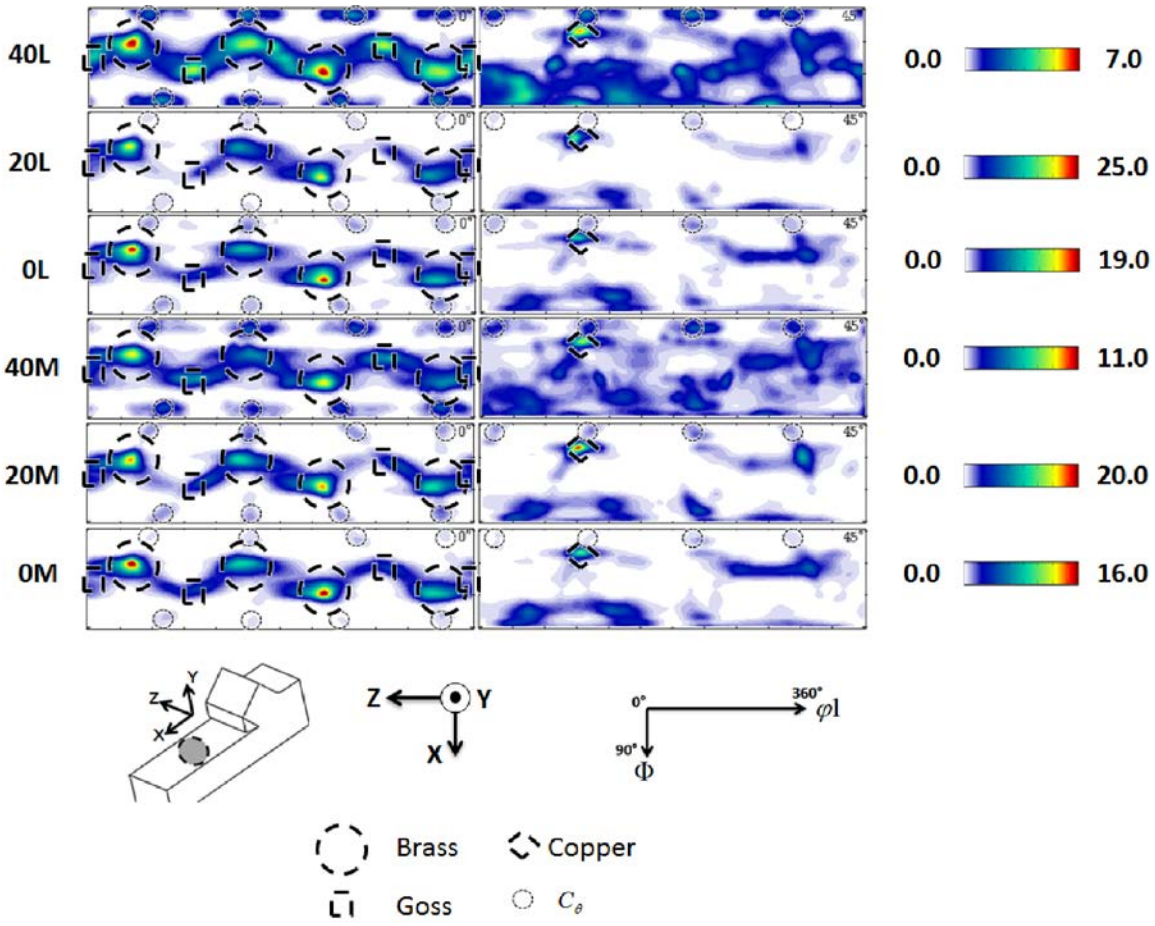

Figure 25: $\varphi 2 (= 0^\circ$ and $45^\circ)$ sections ODFs reconstructed from empirically collected pole figures on surfaces created during PSM showing rolling texture components (Brass, Goss and Copper) and simple shear (C_θ) texture components. Refer bottom left for spatial configuration of the ODFs and color bar on the right for scale.

4.1.2.9 VPSC Calibration and simulation Results from *in-situ* mechanical characterization of machining with 40L using DIC were used as input for calibrating the VPSC model. For doing this, the instantaneous velocity gradient tensors were calculated on pathlines connecting bulk to chip and material under the surface. The velocity gradient tensors were then input to the VPSC software for predicting textures in the chip and material under the surface respectively. The process is illustrated Fig. 26 which shows the evolution of shapes of material elements, representing deformation history of LSM. The element shapes during different stages of deformation by machining were obtained directly from DIC by following four pathlines representing the motion of the four vertices (analogous to material points) of the element. The initial, intermediary and final element shapes have been shown in blue, green and red respectively. Simple shear deformation is evident from the evolution of the chip and surface element shapes with significant rotation for the former. The surface element however deforms in plane, parallel to the surface that is created.

(111) pole figures of material in chip and under the surface obtained from VPSC simulations and their empirically measured counterparts (using OIM and XRD respectively) are shown in Fig. 26b. The VPSC model performs very well for predicting textures under the surface and reasonably well while predicting textures in the chip. Grain Sub Division (GSD; R=5) and Grain Co-Rotation (GCR) features of the model were turned on in these simulations. GSD refers to a feature in the VPSC model by which, a grain splits when it achieves a preset aspect ratio (R) due to shear deformation. GCR refers to the feature in the VPSC model using which, each grain is coupled with another randomly chosen grain in the input discretized ODF. This way, influence of neighboring grains in polycrystals in slowing down evolution of texture by preventing independent rotation of individual grains during plastic

deformation is emulated. It must be noted that while the aforementioned VPSC scheme generally performed well while simulating texture evolution during machining, certain modifications had to be made to reduce some inaccuracies as discussed in the following paragraphs.

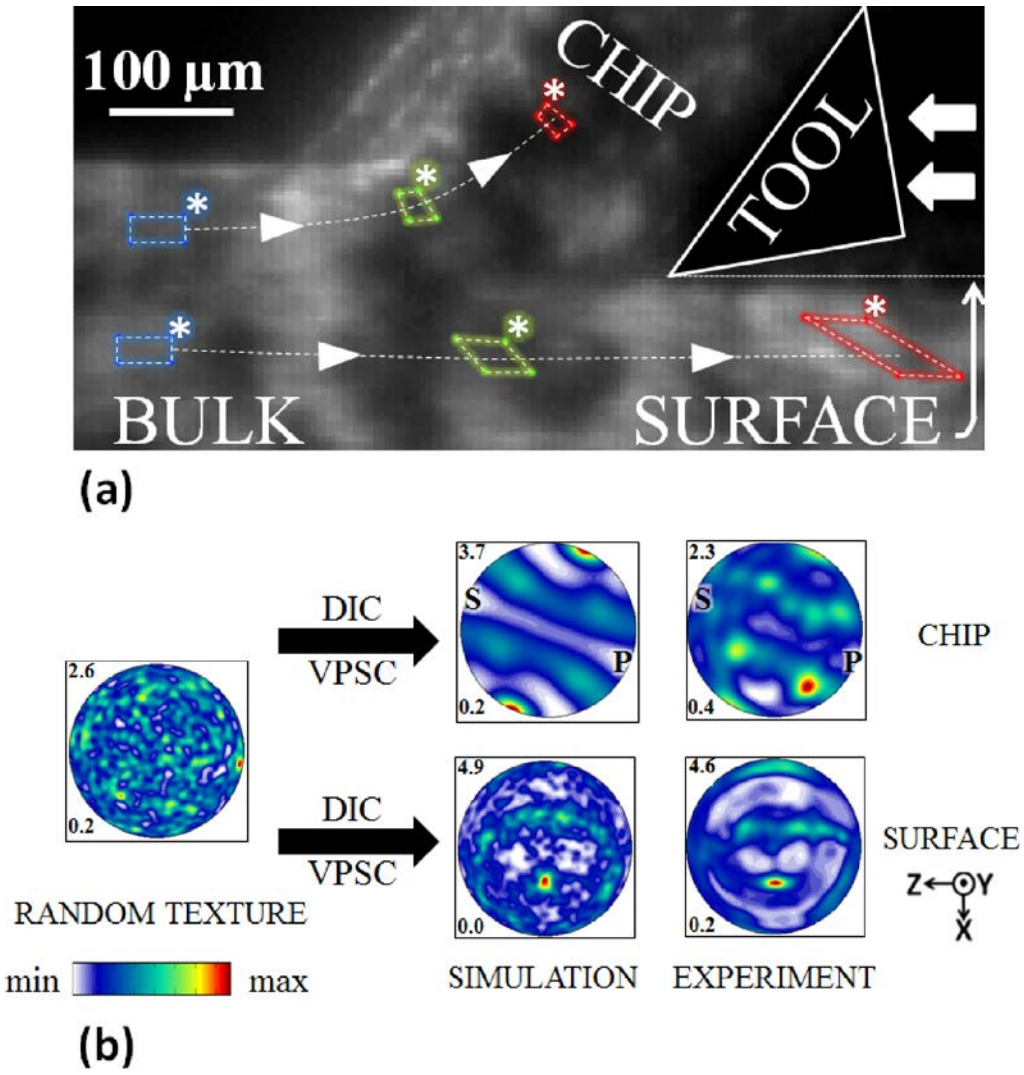

Figure 26: (a) Deformation history of the surface and chip created during PSM with 40L showing evolution of material element during deformation. (b) Experimental and simulated (111) pole figures obtained from VPSC respectively. Refer PS and XYZ in Fig. 18 for reference. Refer respective insets for color code and numbers in pole figure boxes for scale (bottom left: min and top left: max).

To complement the use of empirically based VPSC, deformation histories for the surface generated were obtained from the FEM model and input to the VPSC model. Fig. 22 shows pole figures obtained from empirical measurements and corresponding predictions of the VPSC model for machining conditions (40L, 20L, 0L, 40M, 20M and 0M). It is interesting that the empirical pole figures from different conditions demonstrate a comparable character. It is also evident from the predicted pole figures that this aforementioned similarity in character has been successfully simulated using the purely computational framework (FEM +VPSC). Table III provides a summary of the texture strengths calculated from the reconstructed ODFs of the empirical and simulated textures using $T = \int f(g)^2 dg$. Note that there is good agreement between the empirical and computational texture intensities. The computational model overestimates the texture for machining with 0L and reasons for this are discussed in the following sections.

Table III Empirical and Computational texture intensities of reconstructed ODFs.

PSM	Empirical Intensity T	Simulated Intensity T
40L	2.39	3.27
40M	2.20	2.64
20L	4.47	4.64
20M	4.64	4.64
0L	3.24	5.18
0M	3.54	3.44

It was mentioned that VPSC simulation of texture evolution during machining was performed with GSD activated (R=5). However, using this scheme, significantly smaller intensities (T = 2.51 and T = 2.42, respectively) were predicted in the surface created during

machining with 0M and 20M as opposed to empirically observed values (T = 3.44 and T = 4.44), respectively. To rectify this, we note that the GSD feature in the VPSC model splits a grain when it achieves a predefined aspect ratio (R) due to shear deformation, in a manner somewhat similar to Geometric Dynamic Recrystallization (GDRX) [9]. In this manner, the VPSC framework models formation of new grain by GDRX. However, we have previously shown that SPD induced grain refinement by GDRX slowed down in the chip during machining with 20M and 0M, compared to 20L and 0L. This empirically observed slow-down of GDRX in 20M and 0M was imposed in our simulations by retarding grain splitting by turning GSD off, whereby formation of new High Angle Grain Boundaries was slowed down, albeit artificially. In this manner, a better match between empirical and simulated intensities were be obtained (T = 3.44 and T = 4.64, respectively) for 0M and 20M, respectively (empirical: T = 3.44 and T = 4.44, respectively). In addition to turning the GSD scheme off while simulating texture evolution during machining in 0M and 20M, GCR was turned off for simulating textures in 20M as this improved the pole figure prediction slightly.

It is also shown in Ref. [9] that material forming the chip during machining with 0L condition undergoes maximum amount of recrystallization compared to all other thermomechanical conditions studied here. In a sense, this implies that the thermomechanical conditions prevalent in the deformation zone during chip formation in machining with 0L are most amenable to formation of new grains. To simulate this, the maximum aspect ratio for GSD was decreased from R = 5 to R = 3. However, despite these measures, significantly larger texture intensity was predicted by the VPSC model for 0L (T = 3.26 (empirical), T = 5.18 (VPSC)). It must be realized that VPSC does not incorporate other models of grain refinement like rotational recrystallization that are likely active during machining with 0L which can contribute to these

texture anomalies. Due to the absence of the aforementioned models of grain refinement in VPSC, texture evolution and corresponding intensities would be overestimated here. However, incorporation of these additional modes of grain fragmentation will essentially contribute to a better emulation of real texture evolution and result in a concomitant weakening of texture intensities here.

4.2 MICRO MACHINING

The procedure for micromachining involved a wedge shaped tool (T) that was advanced into a workpiece (S) whereby a preset depth a_0 is deformed in simple shear (Fig. 12a) within a deformation zone to create a chip with thickness a_c. Owing to the configuration of the setup, the deformation zone is not occluded but remains exposed unlike in other common configurations of SPD like Equal Channel Angular Pressing (ECAP), High Pressure Torsion (HPT), etc. Exploiting this feature, we utilized a custom built deformation stage capable of operating within the chamber of a Scanning Electron Microscope (SEM) (Fig. 13). By doing this, it became possible to observe and quantify the flow of material through the deformation zone of LSM using Digital Image Correlation (described in the following paragraph). LSM was performed on annealed and pre-strained (cold-rolled, ε = 0.32) Ni 200, both featuring a grain size of 100 μm – 200 μm. Annealing was performed at 973 K for 1 h. Speed of advance (V) of the wedge shaped tool was maintained at 150 μm/s whereby near isothermal conditions could be ensured. a_0 was set between ~10 μm and 1 μm. While performing SPD, the thickness of the work piece in the Z (Fig. 12a) direction was set at ~100 μm whereby plane strain conditions in the deformation zone

were maintained. A commercially available, nominally sharp single crystal diamond tool was procured from Technodiamant for performing machining. This configuration also makes the results relatable to diamond micromachining, which is used in the fabrication of a range of precision components, including optics, biomedical devices, etc.

Digital Image Correlation (DIC) was used to quantify the deformation zone of LSM. Details of this technique can be found in Section 3.1.1.1. Microstructure response of the material forming the chip was quantified by performing Orientation Imaging Microscopy (OIM) using Electron Back Scattered Diffraction (EBSD) in a Philips XL 30 scanning electron microscope equipped with a Hikari EBSD detector. Samples for OIM were prepared by mounting partially detached chip specimens in epoxy followed by mechanical polishing, down to a 0.05 μm surface finish. Subsequently, OIM specimens were polished in a vibratory polisher for several hours using a 0.05 μm Alumina suspension. The resulting EBSD micrographs were analyzed by finding the average grain and sub-grain sizes (δ_{15° and δ_{2°) defined as domains enclosed by boundaries featuring misorientations > 15˚ and 2˚, respectively. δ_{15° and δ_{2° were calculated by finding area weighted means of grain and sub-grain sizes in the scanned EBSD micrographs. This was done using the TSL OIM 5.0 software in which $\delta_{15^\circ}/\delta_{2^\circ}$ of an individual grain/sub-grain is found by calculating the corresponding area enclosed and then finding the diameter of a circle with equal area. The starting microstructure of the bulk material undergoing machining was characterized using X Ray Diffraction (XRD) and dislocation densities were calculated using the technique described in Section 3.4.

4.2.1 Mechanics of Deformation

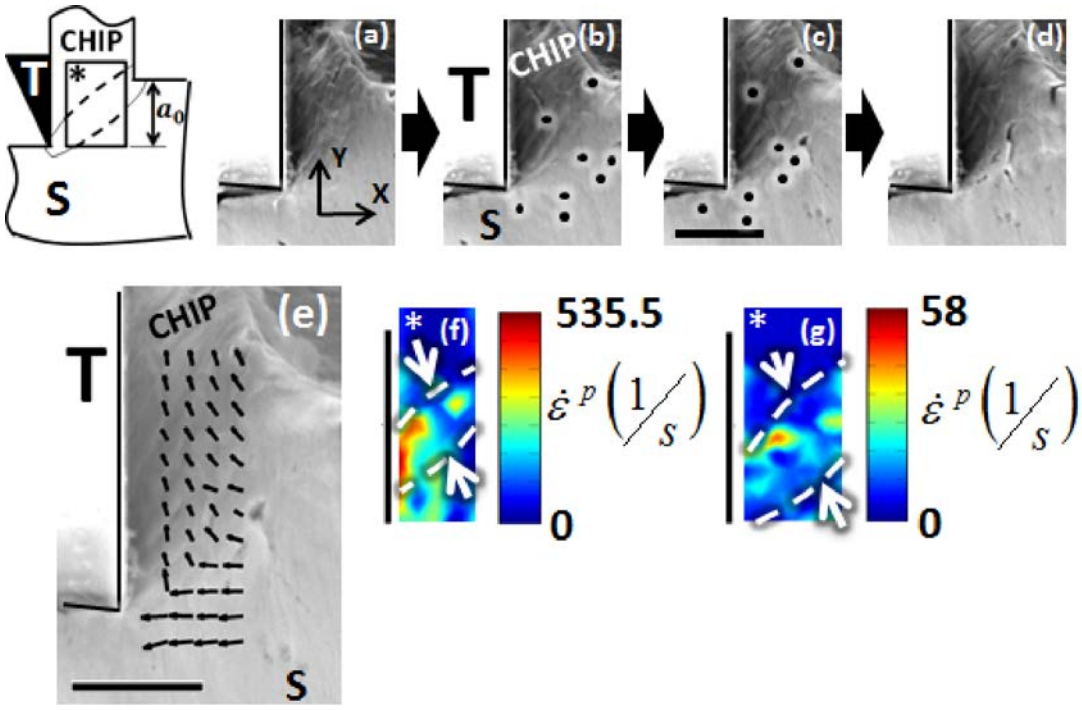

Figure 27: (a)-(d) Sequence of Secondary Electron Images for performing Digital Image Correlation captured during machining of annealed Ni with V=150 μm/s and a_0= 11 μm. (e) Displacement field obtained from DIC of (a)-(d). Strain rate field obtained from DIC for machining with V=150 μm/s and (f) a_0= 2 μm (g) a_0= 11 μm. The deformation zone in (f) is an order of magnitude thinner (~0.7 μm) compared with (g) ~4 μm. Scale bars are 10 μm for (c), (e) and (g) and 2 μm for (f).

The results of in-situ characterization of material flow in the deformation zone during machining are shown in Fig. 27. Figures 27a through 27d show the images in the sequence recorded during machining of annealed Ni with V = 150 μm/s at a_0 = 11 μm. Figures 27b and 27c illustrate DIC of asperities (highlighted using black dots) in the deformation zone of machining. By performing this process repeatedly for a grid of asperities close to the deformation zone, a displacement field was produced (Fig. 27e) and then was differentiated spatially and

temporally to produce the strain rate field (Fig. 27f). Figure 27g shows the strain rate field calculated using this procedure during machining of Ni with V=150 μm/s at a_0=2 μm. While the strain rate fields during machining at a_0=11 μm and 2 μm are geometrically similar, shrinking length scales (reducing a_0) results in SPD being imposed in increasingly confined zones. White arrows (in Figs.27f, 27g) show deformation zone thicknesses h of ~0.7 μm and ~4 μm during machining with a_0 2 μm and 11 μm, respectively. The effective strain imposed on the chip during machining can be found by measuring the chip thickness ratio a_0/a_c as [42] : $\varepsilon = \frac{\cos\alpha}{\sqrt{3}\sin\varphi\cos(\varphi-\alpha)}$, where φ is given by $\tan\varphi = \frac{a_0/a_c\cos\alpha}{1-a_0/a_c\sin\alpha}$. We find that as a_0 is reduced from 11 μm through ~5 μm to 1 μm, similar SPD strains ε = ~2 are imposed on the material forming the chip albeit in increasingly spatially narrow deformation zones. The same trend was observed for annealed as well as pre-strained samples. Note that, h is often approximated as $l/10$ where $l = a_0/\sin\phi$ is the length of the idealized deformation plane [31]. This approximation gives similar h values (3.5 μm and 0.6 μm) for machining of annealed Ni with a_0 = 11 μm and 2 μm (~4 μm and 0.7 μm seen empirically), respectively. Based on this empirical trend, the predicted deformation zone thicknesses during machining of annealed Ni at V=150 μm/s for a_0 ranging between 10 μm and 1 μm are shown in Fig. 28. It must be noted that for the same amount of imposed ε, decreasing thickness of the deformation zone (h) implies increasing strain gradients. Approximate strain gradients given by ε/h (= $2/h$) for different a_0

are also shown in Fig. 28. Reducing a_0 leads to a spatial constriction of the zone over which SPD is imposed and leads to a concomitant magnification of the associated strain gradients.

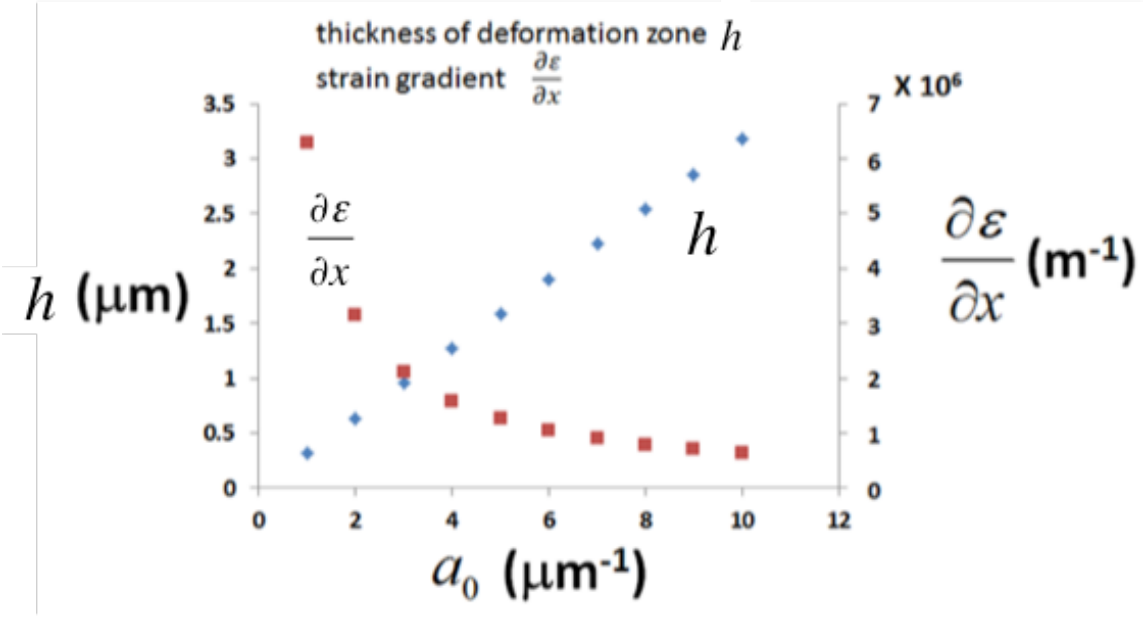

Figure 28: Predicted deformation zone thicknesses for machining of annealed Ni with V=150 μm/s at specified a_0 values (blue). Prevalent strain gradients in the deformation zone of machining with corresponding a_0 values (red).

4.2.2 Characterization of starting bulk microstructure using XRD

Dislocation densities (ρ) in the starting bulk microstructures (annealed and pre-strained) were characterized using XRD line broadening analysis. Instrumental broadening was ignored in this analysis as the Full Width at Half Max of the XRD peaks collected from the samples were an order of magnitude larger than the resolution of the detector. ρ = ~ 6 * 10^{14} m^{-2} and ~ 1.50 * 10^{15} m^{-2} were found for the annealed and pre-strained samples, respectively. Dislocation

densities back calculated from empirically observed hardness data [4], using the Taylor relation, $\tau = \tau_0 + \alpha G b \sqrt{\rho}$ produced similar values ρ = ~3.6 * 10^{14} m^{-2} and = ~1.20 * 10^{15} m^{-2} for the annealed and pre-strained samples, respectively. The nominal average grain size measured using optical metallography was ~ 150 μm.

4.2.3 Orientation imaging Microscopy of Microstructure Evolution

4.2.3.1 Chip microstructures Fig. 29 shows the Inverse Pole Figures (IPF) obtained from OIM performed on partially detached chip specimens using EBSD. The specimens were obtained from machining of annealed Ni with V=150 μm/s at a_0=12 μm, 6.5 μm, 5.5 μm, 3.4 μm and 1 μm (IPF shown in Fig. 29a through 29e, respectively). OIM was performed on a rectangular region of the partially detached chip specimen schematized in the inset (top left in Fig. 29). In this manner, the regions within the OIM maps closer to the bottom right corresponded to the un-deformed bulk whereas the regions closer to the top left corresponded to the chips produced during machining.

We find that during machining with a_0 between 12 μm and 5.5 μm, the material forming the chip undergoes significant grain refinement as it progresses through the deformation zone (final δ_{15° = ~500 nm; initial δ_{15° = ~150 μm). In contrast to this, chips obtained from machining with a_0=3.4 μm and 1 μm exhibit an anomalous lack of refinement whereby a larger grain size δ_{15°=~1.67 μm and 1.1 μm were obtained, respectively. Furthermore, δ_{15° obtained from the latter also exhibited significantly larger scatter as shown in Fig. 30. In comparison with δ_{15°, δ_{2° in all LSM conditions exhibited similar values (~250 nm), albeit with larger scatter.

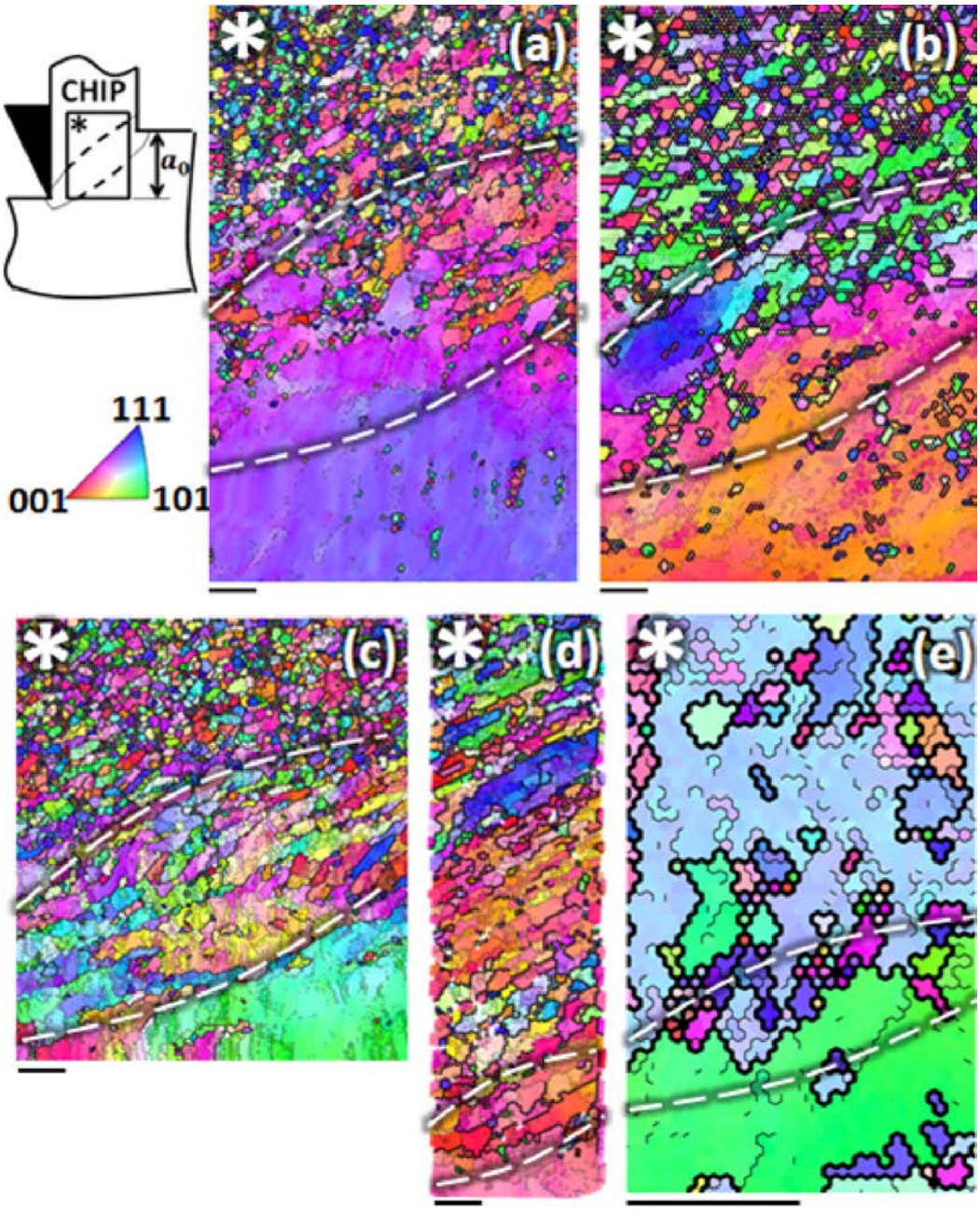

Figure 29: Inverse Pole Figures obtained from Orientation Image Microscopy of partially detached chip specimens obtained during machining of annealed Ni with V=150 μm/s at a_0 = (a) 12 μm (b) 6.5 μm (c) 5.5 μm (d) 3.4 μm (e) 1 μm. Refer insets in top left for spatial configurations of zones within partially detached chip specimens where OIM was performed and color code. All scale bars are 1 μm. Dashed lines show approximate location of deformation zone.

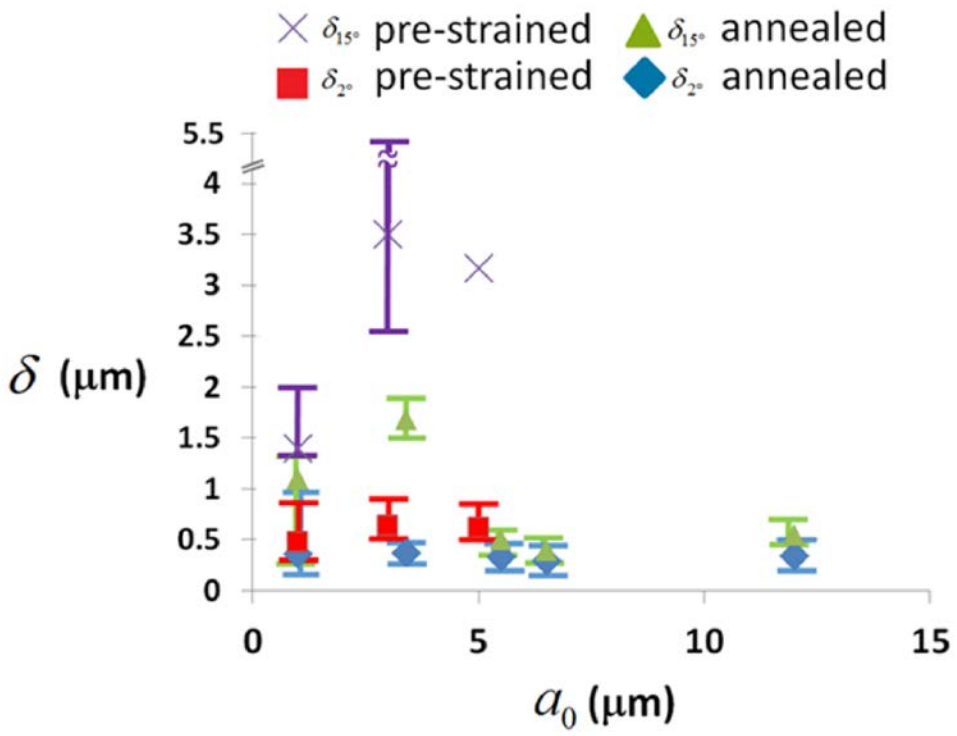

Figure 30: Grain size statistics obtained from chips created during machining of Ni.

The aforementioned lack of refinement manifested in the presence of large grains enclosed by High Angle Grain Boundaries (HAGBs) that contained a sub-grain dislocation structure composed of Low Angle Grain Boundaries (LAGBs), often interspersed with stray segments of High Angle Boundaries (HABs). The statistics (Fig. 30) demonstrate a length scale effect in the progression of microstructure evolution during SPD.

Fig. 31 shows the misorientation distribution plots obtained from the respective chips. Figures 31a through 31c correspond to chips obtained with a_0=12 μm, 6.5 μm and 5.5 μm, respectively and show a nearly random misorientation distribution characteristic of UFG microstructures, with mean misorientation angle $\langle\theta\rangle$ = 35˚, 37˚ and 33˚ respectively. However, lack of grain refinement would necessitate the presence of large grains and reduction of the HAB

content. This in turn would manifest in misorientation distributions shifting towards smaller values as seen in Figs. 31d and 31e which correspond to a_0 = 3.4 μm and 1 μm and feature $\langle\theta\rangle$= 22˚ and 24˚ respectively.

Fig. 32 shows the IPFs obtained from OIM performed on chip specimens created during machining with V=150 μm/s at a_0=5 μm, 3 μm and 1 μm on Ni samples pre-strained to ε=0.32 by rolling. The IPFs qualitatively reveal significant differences in comparison with those obtained from LSM of annealed Ni for similar a_0 values.

The chip obtained during machining of pre-strained Ni with a_0=5 μm exhibits large grains signifying lack of microstructure refinement during SPD. Quantitative analysis of the chip microstructure reveled δ_{15°=3.2 μm and δ_{2°=~616 nm in contrast to smaller values (δ_{15°=500 nm and δ_{2°=~250 nm) obtained from machining of annealed Ni in analogous conditions (V=150 μm/s and a_0=5.5 μm). A similar deviation in microstructural features was observed during machining of pre-strained Ni with a_0=3 μm and V=150 μm/s (δ_{15°=3.5 μm and δ_{2°=~638 nm) when compared with machining of annealed Ni at a_0=3.4 μm and V=150 μm/s (δ_{15°=1.67 μm and δ_{2°=~360 nm). For a_0=1 μm and V=150 μm/s, chips produced from pre-strained Ni exhibited (δ_{15°=1.4 μm and δ_{2°=~478 nm) compared with (δ_{15°=1.1 μm and δ_{2°=~355 nm) for chips produced from annealed Ni.

Fig. 33 shows the misorientation distributions of the grain structure in the chips created during machining of pre-strained Ni. The distributions show a similar bias towards smaller angles in smaller length scales, indicative of lack of grain refinement as seen in chips created from annealed Ni. Furthermore, a comparison of Fig. 31a, featuring$\langle\theta\rangle$ = 22˚ (a_0=5 μm) with

Fig. 33c, $\langle\theta\rangle$ = 33˚ (a_0=5.5 μm) corroborates the influence of pre-strain in instigating length-scale inflicted microstructure evolution during SPD. However, this deviation became somewhat moderate in smaller length scales ($\langle\theta\rangle$ = 20˚, 23˚) during machining of pre-strained Ni with a_0 =3 μm and 1 μm, compared with ($\langle\theta\rangle$ = 22˚, 24˚) machining of annealed Ni with a_0=3.4 μm and 1 μm, respectively.

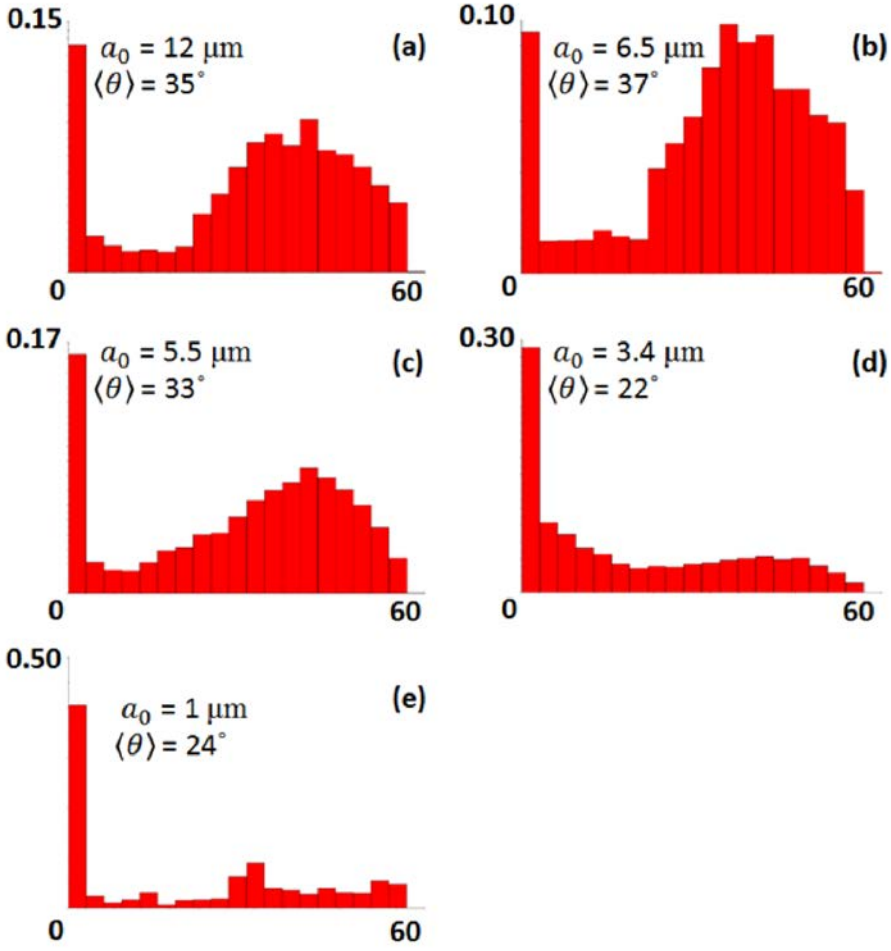

Figure 31: Misorientation (θ) distributions obtained from chips created during machining of annealed Ni with V=150 μm/s at specified a_0 values.

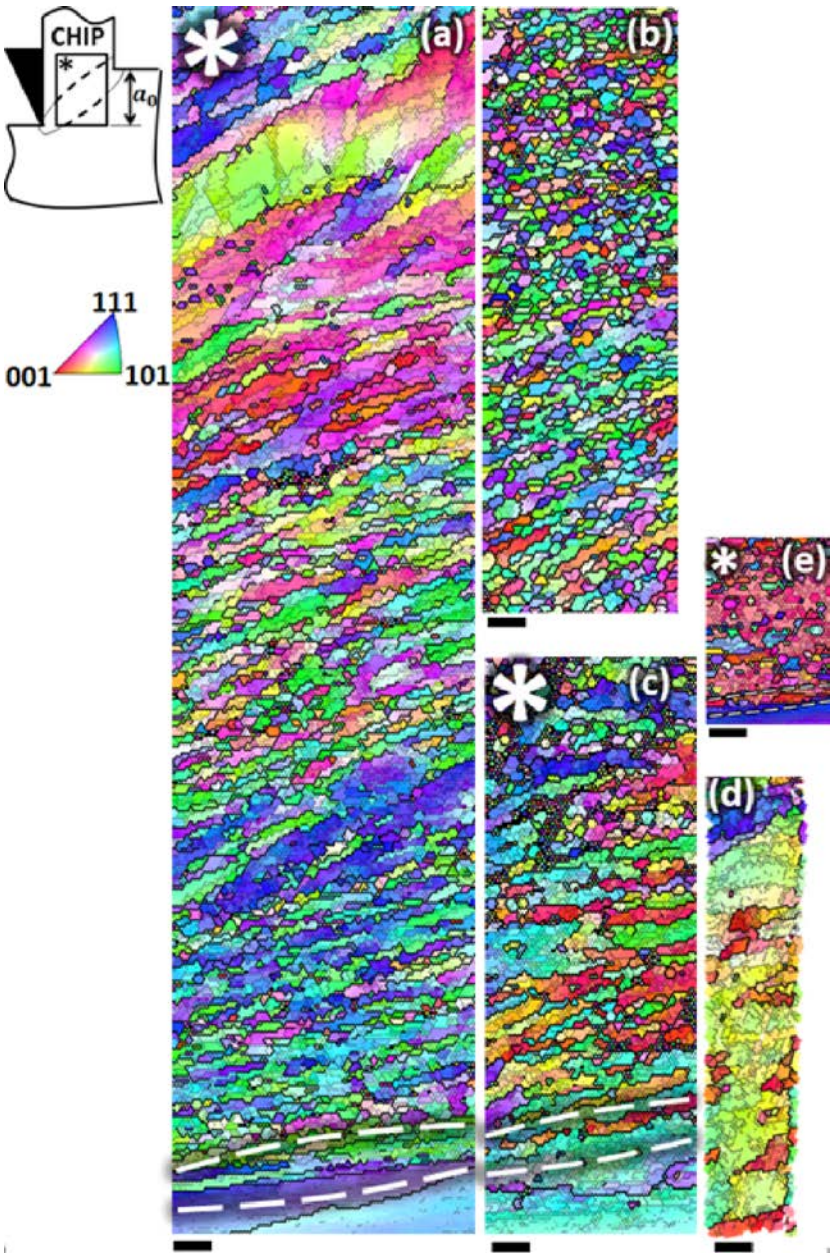

Figure 32: Inverse Pole Figures obtained from Orientation Image Microscopy of partial chip specimens obtained while machining of pre-strained Ni with V=150 μm/s at *a* = (a)-(b) 5 μm, (c) – (d) 3 μm and (e) 1 μm. Refer insets in top left for spatial configurations of zones within partially detached chip specimens (for (a) and (c)) where OIM was performed and color code. All scale bars are 1 μm. Dashed lines show approximate location of deformation zone.

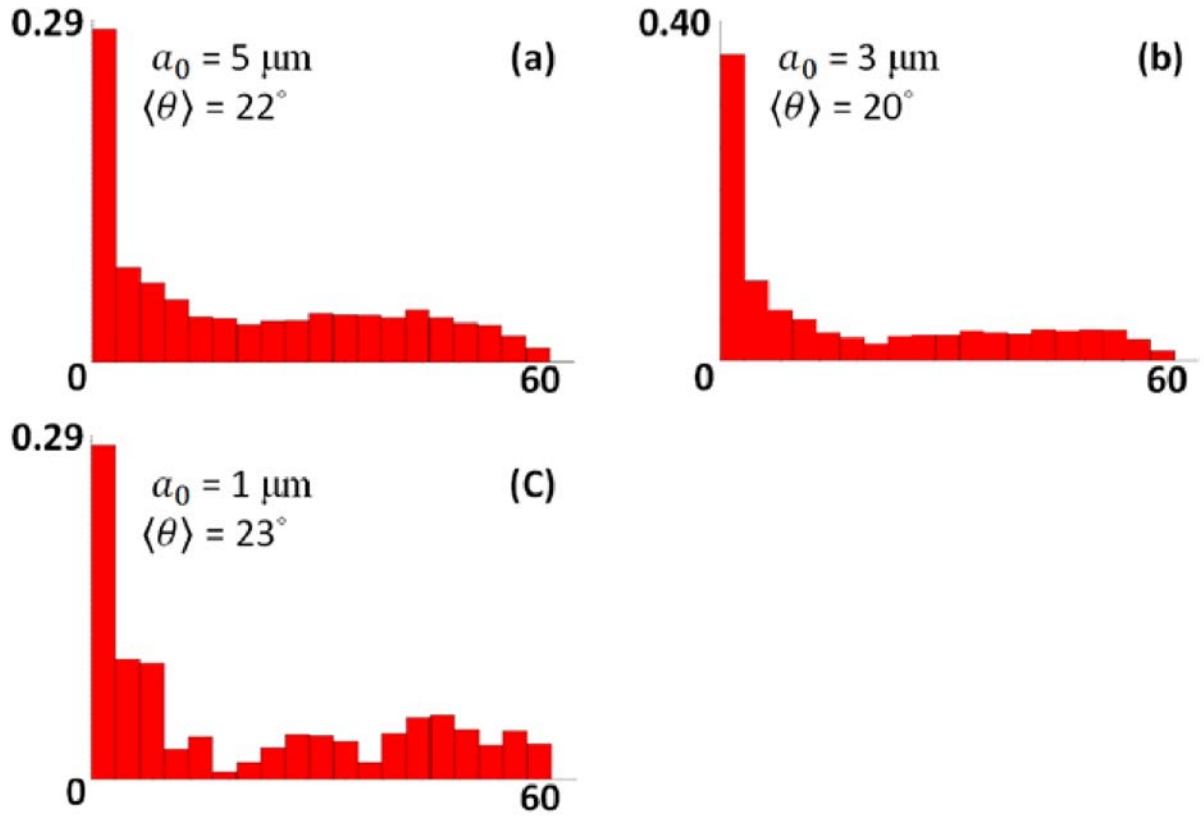

Figure 33: Misorientation (θ) distributions obtained from chips created during machining of pre-strained Ni with V=150 μm/s at specified a_0 values.

These observations suggest an effect of length scales on microstructure evolution behavior during SPD in Ni that is intensified by pre-strain. In this, microstructure evolution during SPD involving grain refinement is replaced with lack of refinement even after SPD as the length scales go down. It is important to note that the chip microstructures were inherited from the deformation zone of machining, necessitating a switchover in the mechanics of microstructure evolution there, across large and small length scales in annealed and pre-strained samples. The next section provides a description of the mechanics of microstructure evolution in the deformation zone of machining.

4.2.3.2 Microstructure evolution in the deformation zone Figures 29a through 29c reveal mechanics of microstructure evolution as material progresses through the deformation zone to form the chip during machining of annealed Ni at larger a_0 values (> 5 μm). We find that in these spatial regimes, microstructure evolves gradually in response to SPD whereby a large grain develops a dislocation sub-structure, which evolves progressively through the deformation zone as the tool advances. It has been shown using TEM of rolled Ni [4] that among others, the aforementioned sub-structure include Incidental Dislocation Boundaries (IDBs) and Geometrically Necessary Boundaries (GNBs). IDBs are composed of statistically trapped dislocations whereas GNBs are created out of geometrical necessity due to strain gradients. GNBs therefore demarcate regions in which different sets of slip systems are activated to sustain plastic flow or the same set of slip systems are activated to different extents. Progressive microstructure evolution during SPD results in continuous increase of mean misorientation angles of IDBs and GNBs. In this manner, neighboring parts of the same crystal gradually reorient themselves to significantly different orientations and develop High-Angle Grain Boundaries (HAGBs) between them. A similar phenomenon is evidenced during machining of annealed Ni with $a_0 \approx 12$ μm (Fig. 34) where two neighboring regions within the same crystal (A and B) in the deformation zone are shown to be connected by a path lacking any HAGBs. However, these neighboring regions have developed significant misorientation with respect to each other (~45˚) suggesting the presence of a GNB between them.

The aforementioned mechanism continues by the segregation of more such regions whereby more GNBs (and IDBs) are created. In this manner, UFGs are formed by progressive refinement as material progresses through the deformation zone into the chip. This is assisted by other mechanisms like GDRX in which, thin serrated pancake shaped zones surrounded by

HAGBs are pinched off whereby several UFGs are created [9]. It has been seen that δ_{15° created using these mechanisms are similar to δ_{2° [7, 9] and this is indeed the case as verified by quantitative investigation of the OIMs of chips created during LSM of annealed Ni with large a_0 >5 μm (δ_{15° = ~0.5 μm and δ_{2° = ~0.25 μm).

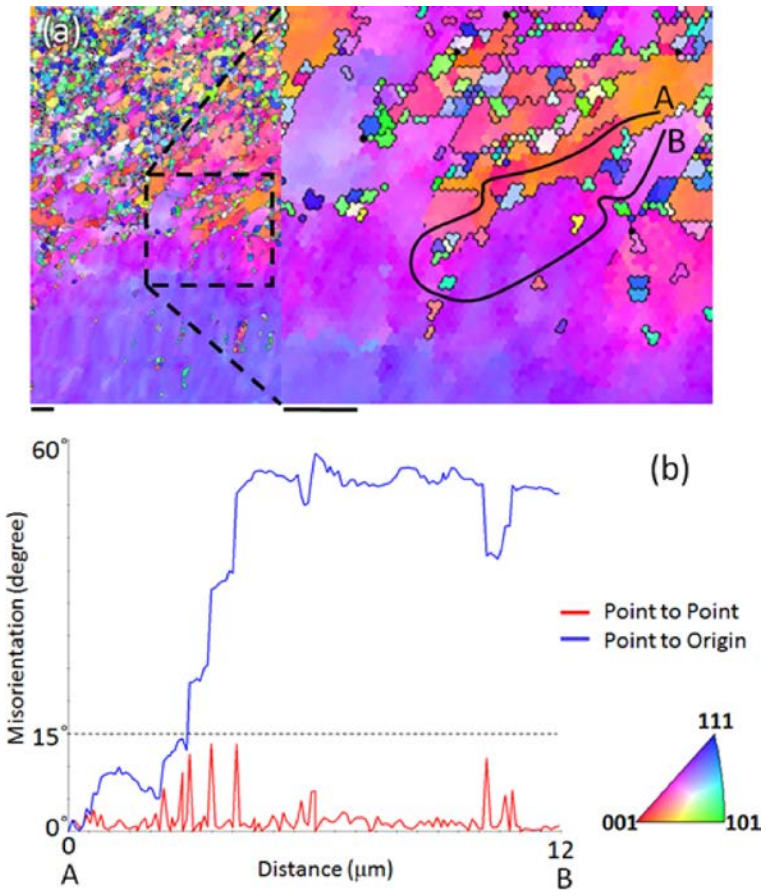

Figure 34: (a) Inverse Pole Figure of microstructure field obtained from the deformation zone of machining of annealed Ni with a_0 = 12 μm. The inset shows two neighboring regions of the same crystal in the microstructure near the deformation zone that are heavily misoriented with respect to each other but are connected by a path that does not contain HAGBs. This suggests that the two regions are separated by a GNB. (b) Point to point and point to origin misorientation along path A-B connecting the two regions. All scale bars are 1 μm. Refer inset in bottom right for color code.

When compared with this picture of grain refinement (that is progressive in nature), Figs. 29d, 29e and 32a through 32c exhibit an abrupt mechanism of microstructure evolution. These figures correspond to instances of machining in which the anomalous lack of grain refinement was observed, *viz.* annealed Ni with a_0 < 5 μm and pre-strained Ni. Interestingly, this deviation of behavior from traditional microstructure evolution mechanisms is more pronounced when the bulk material is pre-strained as evidenced in Fig. 32a with respect to Fig. 29c (deformation zones of machining of pre-strained and annealed Ni respectively with a_0 = ~5 μm). Characteristics of this trajectory of microstructure evolution involve a single HAGB demarcating the start of chip microstructure zone, present nearly parallel to the idealized deformation plane (Fig. 12a). This contrasts conventional microstructure evolution observed in annealed specimens with a_0 ≥ ~5 μm. The HAGB leads into a single large grain within the chip, which is heavily defected with LAGB structures and interspersed along isolated HAB segments. Additionally, these instances lack gradual microstructure evolution through the deformation zone to a UFG state. These observations provide the basis for larger δ_{15° observed in the chip during machining with a_0 < ~3.5 μm in annealed and a_0 < ~5 μm in pre-strained Ni samples.

An instance of this scheme of microstructure evolution is magnified in Fig. 35a which shows the grain structure of the chip created during LSM of pre-strained Ni with a_0 = 5 μm. In the color scheme utilized in Fig. 35a, each adjacent grain is assigned a different color for facilitating visual differentiation. Here, grains refer to domains in the microstructure that are enclosed within a boundary featuring misorientation > 15˚. The grain boundary close to the deformation zone borders a large grain (~ 6 μm in length in the chip). The corresponding IPF is shown in Fig. 35b. Fig. 35c shows the magnified view of the white inset marked in Fig. 35a (Refer Fig. 12a for spatial configuration reference).

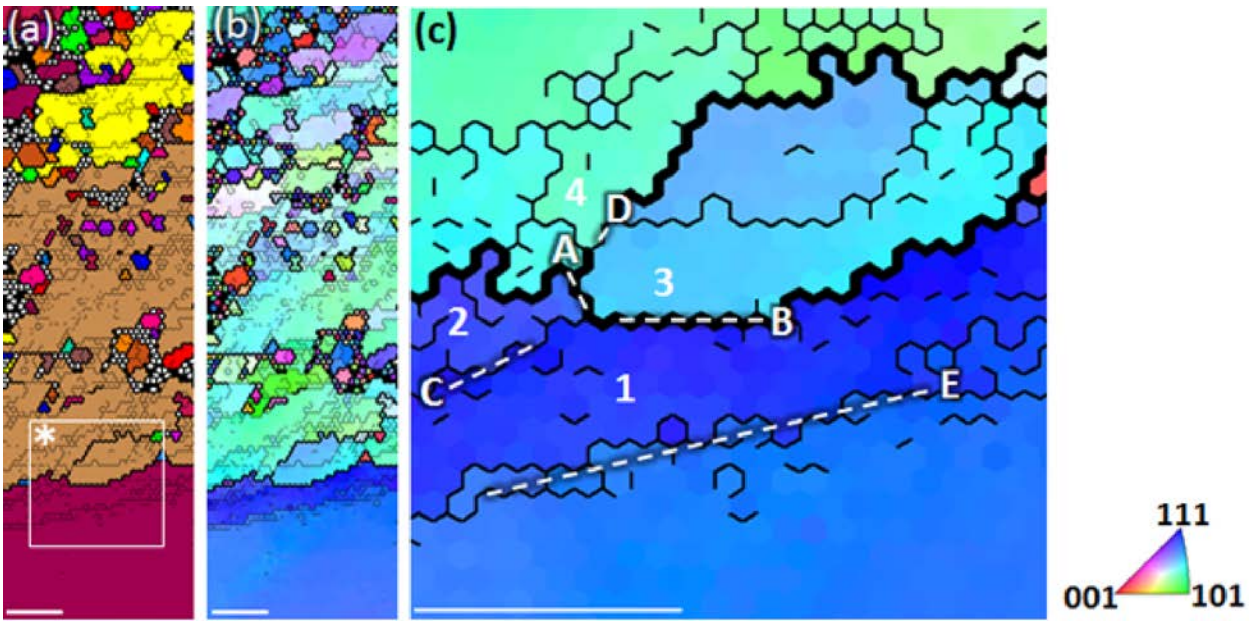

Figure 35: Mechanism of Geometrically Necessary Dynamic Recrystallization. (a) Unique grain color map showing bulk and chip microstructures produced during machining of pre-strained Ni with V=150 μm/s and a_0= 5 μm. (b) Inverse Pole Figure corresponding to (a). (c) Magnified view of the microstructure in the deformation zone within the region marked with the white box in (a). Misorientation of highlighted boundaries are: A (~16˚), B (~24˚), C (~8˚) and D (~ 14˚). Refer asterisk (*) in Figure 1a for spatial configuration. All scale bars are 1 μm.

Microstructural domains labeled 1, 2-3 and 4 (Fig. 35c) correspond to regions before, within and beyond the deformation zone, respectively. Domains 3 and 4 are integral parts of the chip microstructure (Fig. 35a) and feature large angular misorientation with respect to the domain 1 (bulk) ~24˚ and ~40˚ respectively. However, 2 is at an intermediate angular orientation featuring a misorientation of ~16˚ and 8˚ with domain 3 (chip) and 1 (bulk) respectively. This angular configuration of neighboring microstructural domains suggests a progressive rotational mechanism in which spatially Ultra-Fine regions in the deformation zone of machining reorient progressively, until the entire microstructure field advancing into the deformation zone reorients

to become the chip. In this manner, chips featuring large δ_{15° are created when reorientation of adjacent domains match closely. However, owing to statistical crystallographic orientation fluctuations, this can leave HAGB debris in the chip in locations where re-orientation is not complete/similar to adjacent domains. In a mechanistic framework, similar progressive rotation translates to activation of similar slip systems through the length of the deformation zone. Owing to unidirectional simple shear deformation geometry in machining (Fig. 12b), coupled with increasingly confined deformation zones in smaller a_0 regimes, this is indeed a possibility. It can be hypothesized that this is what happened in zone 3 which by reorientation, decreased its misorientation to < 15˚ in the boundary segment D (θ = ~14˚) and became an integral part of the chip.

4.2.4 Discussion

4.2.4.1 Temperature rise in the deformation zone It is known machining is a thermo-mechanically coupled deformation process in which heat dissipated during plastic deformation can result in temperature rise, thus influencing the mechanics of microstructure evolution [9]. Here we examine a theoretical estimate of the temperature rise in the deformation zone of machining calculated using Oxley's extended model [43]. During machining, heat is dissipated in a moving heat source configuration from the deformation zone across which mass transport happens. Temperature rise in the chip can therefore be calculated using techniques akin to those in Ref. [43]. While it is difficult to perform thermometry of the deformation zone inside the SEM, such validated theoretical models can provide a reliable estimate of the temperature zone [9]. In particular, we sought to isolate the role of the scale of the deformation zone on the

resulting microstructure attributes and to that effect, sought to minimize the temperature rise via the choice of the low deformation speeds.

Incremental temperature rise in the chip is given by the equation $\rho C_p dT = (1-\beta)\sigma(\varepsilon, \dot{\varepsilon}, T)d\varepsilon$ where $d\varepsilon$ is the incremental strain in the chip as it moves through the deformation zone. β is the fraction of heat that is transported by the bulk away from the deformation zone and is given by:

$\beta = \frac{1}{4\alpha} erf\sqrt{\alpha} + (1+\alpha) erfc\sqrt{\alpha} - \frac{e^{-\alpha}}{\sqrt{\pi}}\left(\frac{1}{2\sqrt{\alpha}} + \sqrt{\alpha}\right)$ where $\alpha = (Va_0 \tan\varphi)/4*\kappa$. Here, κ is the thermal diffusivity of Ni (~22mm^2/s). Assuming Johnson-Cook material model, rearranging and subsequently solving the equation: $\int_{T_0}^{T_{calc}} \frac{\rho C_p}{1-\left(\frac{T-T_r}{T_m-T_r}\right)^m} dT = (1-\beta)*\left(A\varepsilon + \frac{B}{n+1}\varepsilon^{n+1}\right)*\left(1 + C\ln\frac{\dot{\varepsilon}}{\dot{\varepsilon}_0}\right)$

, the final temperature in the chip (T_{calc}) was found. Here, A, B, C and m were Johnson-Cook material parameters for Ni obtained from Ref. [44]. ρ and C_p were density and specific heat capacity of Ni. T_0 (starting temperature) was set at 293K. Using this procedure, it was found that the theoretical temperature rise in the chip created in all conditions was < 10 K. Consequently, the effect of heat on the microstructural consequences that have been described can be neglected and the focus can remain on the role of the length-scale of the deformation zone in modifying the mechanics and the microstructure evolution.

4.2.4.2 Spatial confinement of the zone of SPD, resulting strain gradients and the effect on microstructure evolution Deformation can be decomposed into a pure shear and rotational component as:

$$\underline{F} = \frac{\underline{F} + \underline{F}^T}{2} + \frac{\underline{F} - \underline{F}^T}{2}$$

Where,

$\underline{F}$ is the displacement gradient tensor defined as:

$$\underline{F} = \begin{bmatrix} \frac{\partial u}{\partial X} & \frac{\partial u}{\partial Y} & \frac{\partial u}{\partial Z} \\ \frac{\partial v}{\partial X} & \frac{\partial v}{\partial Y} & \frac{\partial v}{\partial Z} \\ \frac{\partial w}{\partial X} & \frac{\partial w}{\partial Y} & \frac{\partial w}{\partial Z} \end{bmatrix}$$ in which u, v and w are displacement along X Y Z directions respectively,

$\underline{\varepsilon} = \frac{\underline{F} + \underline{F}^T}{2}$ is the strain tensor and

$\underline{W} = \frac{\underline{F} - \underline{F}^T}{2}$ is the rotation tensor.

Adopting a similar argument as given in Ref. [23], we note that depending on crystallographic orientation of the bulk material, $\underline{W}$ may be accommodated in two different ways. Fig. 36 illustrates this for machining involving simple shear deformation. Fig. 36a shows an element (A) undergoing simple shear in the deformation zone to convert to the deformed state (B). Case 1 (Fig. 36b) shows that when plastic strain is accommodated by slip in certain crystallographic orientations that are aligned perfectly with the direction of simple shear, $\underline{W}$ may be accommodated during LSM more easily, without any crystallographic reorientation. However, this may not be possible in other situations e.g., Fig. 36c, where rotation

associated with simple shear will inevitably have a crystallographic re-orientation effect. For ε ~2, rotation associated with simple shear comes to ~60˚. This was calculated by performing polar decomposition of the displacement gradient tensor and then relating the rotation matrix with physical angular re-orientation with respect to axis Z axis (Ref. Figs. 12a).

Spatial confinement of the deformation zone with decreasing a_0 is bound to result in significant curvature in the displacement field (Fig. 27e). This will result in significant crystallographic reorientation close to the deformation zone, accommodated by Geometrically Necessary Dislocations (GNDs) [23]. As noted previously (Section 4.2.4.2), chips created during LSM with small a_0 exhibited a dominant grain boundary demarcating the chip microstructure zone. It is likely that these HAGBs were created due to high curvature in the displacement field near the deformation zone of LSM that intensified in smaller a_0 regimes. The role of curvatures in displacement field resulting in grain fragmentation in crystalline metals is well known [45, 46].

However, instead of continuous and progressive grain fragmentation resulting in UFG microstructures, high curvatures here seem to manifest in large grains by a novel mechanism (Section 4.2.4.2). Effectively, the dominant grain boundary establishes a moving recrystallization front because of geometrical necessity imposed by confinement in low a_0 regimes. Consequently, this mechanism, Geometrically Necessary Dynamic Recrystallization (GNDRX), results in large grains manifesting in the coarse-grained microstructures in the chip during LSM. It is likely that GNDRX results from a coupled effect of high strain gradients and small deformation volume ($\propto$ thickness of the deformation zone $\boldsymbol{h}$) during machining in small $\boldsymbol{a_0}$ regimes. A small $\boldsymbol{h}$ approaching the characteristic length scales associated with dislocation

structures that form during SPD (in large sized specimens) would interfere with conventional microstructure evolution and refinement mechanisms, manifesting in GNDRX.

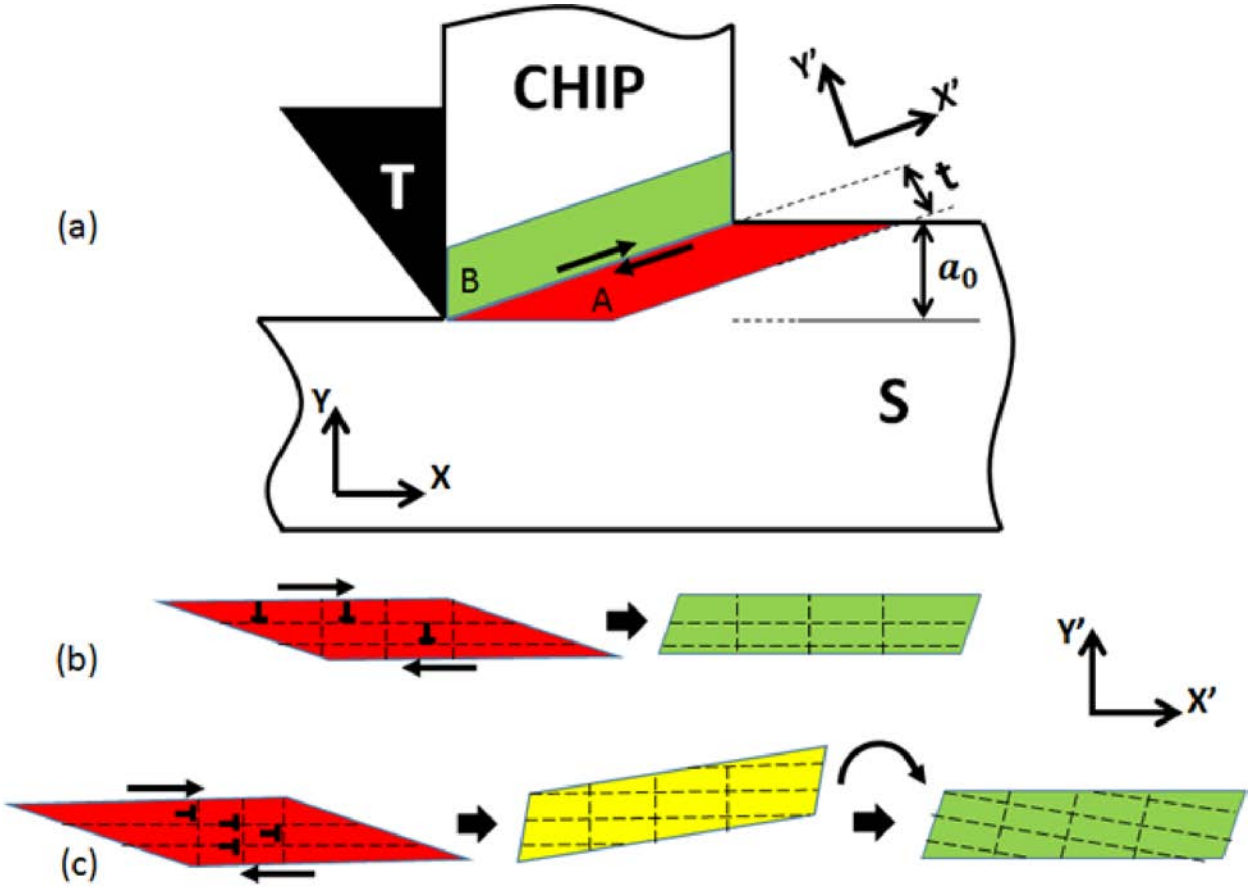

Figure 36: (a) Simple shear deformation during machining. Element A with thickness h is simply sheared in an idealized deformation plane (refer double arrows) as it forms the chip. This idealized model translates to machining with a deformation zone thickness that approximated as h during real machining. (b) Accommodation of simple shear by dislocation slip in planes and directions perfectly aligned to direction of simple shear (X') does not produce any associated crystallographic rotation. (c) Accommodation of simple shear by dislocation slip in planes and directions not aligned with direction of simple shear (X') produces crystallographic rotation.

In order to probe this further, we note that GNBs plays a crucial role in microstructure refinement during SPD [4]. Additionally, GNB spacing (δ_{GNB}) decreases monotonically in Ni

with respect to strain imposed [4]. In turn, this suggests that a larger δ_{GNB} will always be the predecessor to a smaller δ_{GNB} during SPD. Additionally, as a_0 is reduced, the evolution of δ_{GNB} in the material undergoing machining ought to occur progressively over a smaller h. To this end, we hypothesize that if $\delta_{GNB}(x) > x$ where $\delta_{GNB}(x)$ is δ_{GNB} at x which is the distance traversed through the deformation zone by the material undergoing LSM ($0 \le x \le h$), then this evolution will be hampered. To quantify this effect, we find $\frac{h - x_{\min}}{h}$ for different a_0 values (2 μm $\le a_0 \le$ 10 μm). Here $x_{\min}$ is the smallest x at which $\delta_{GNB}(x) = x$. $\frac{h - x_{\min}}{h}$ is the fraction of the spatial extent of the deformation zone in which microstructure refinement by conventional mechanisms can be anticipated to take place because $\delta_{GNB}(x) < x$ within this zone. We find $\frac{h - x_{\min}}{h}$ by fitting the empirically observed evolution of δ_{GNB} with respect to ε as [4]:

$$\delta_{GNB} = 0.41\varepsilon^{-0.83} \tag{8}$$

This captures the empirical behavior with high R^2 (=0.96). Furthermore, we assume a linear strain gradient through the deformation zone whereby:

$$\varepsilon = \varepsilon_f \frac{x}{h} \tag{9}$$

ε_f is the final effective strain imposed on the material forming the chip during LSM (=2). Substituting this in Equation 8 and using $\delta_{GNB}(x) = x$, we obtain:

$$x_{\min} = \left(0.41\left(\frac{2}{h}\right)^{-0.83}\right)^{\frac{1}{1.83}} \text{ or } x_{\min} = 0.45h^{0.45} \tag{10}$$

This implies, $\frac{h - x_{\min}}{h} = \frac{h - 0.45h^{0.45}}{h} = 1 - \frac{0.45}{h^{0.55}} = 1 - \frac{0.45}{(0.35a_0)^{0.55}} = 1 - \frac{0.8}{a_0^{0.55}}$ (11)

Here, $h = 0.35a_0$ was obtained from empirical measurements using DIC (section 4.2.2). Using this topological argument, we see that refinement of δ_{GNB} can be anticipated to take place in a large fraction (~0.75) of the deformation zone during machining with a_0=10 μm. However, when a_0=2 μm and 1 μm, this fraction reduces to ~0.45 and ~0.2, respectively, suggesting significantly hampered microstructure refinement in smaller a_0 regimes by conventionally established dislocation substructure evolution mechanisms in agreement with experimental results.

4.2.4.3 Scaling of microstructure evolution The arguments presented so far suggest a role of curvature in displacement fields, coupled with small deformation volumes in steering microstructure evolution in small length scales. In order to understand this further, we present a phenomenological model of the evolution of grain size δ_{15° as a function of the length scales and starting microstructural parameters here. In doing this, we make the argument that the final grain size δ_{15° is a function of the strain imposed ε. Therefore, δ_{15° must evolve as a function of the distance x traversed through the deformation zone during LSM. In trying to model this evolution, we decouple the refinement of δ_{15° from grain growth (by GNDRX) as:

$$\delta_{15^\circ} = \int \frac{\partial \delta_{15^\circ}^{+}}{\partial x} - \frac{\partial \delta_{15^\circ}^{-}}{\partial x} dx \qquad (12)$$

The first term in the integrand corresponds to grain growth due to GNDRX whereas the second term corresponds to grain refinement due to SPD.

We can expand the second term in the integrand using

$$\frac{\partial \delta_{15^\circ}^{-}}{\partial x} = \frac{\partial \delta_{15^\circ}^{-}}{\partial \varepsilon} \frac{\partial \varepsilon}{\partial x} \qquad (13)$$

Here $\frac{\partial \varepsilon}{\partial x}$ is the strain gradient imposed while machining, which can be approximated using κ (the crystallographic curvature) as [23]:

$$\kappa \propto \frac{\partial \varepsilon}{\partial x} \tag{14}$$

Note that Equation 13 coupled with Equation 14 implies that in the presence of larger strain gradients (essentially resulting in larger crystallographic curvature), microstructure evolution involving refinement will be accelerated [25]. However, GNDRX (progressive sub-grain rotation) is driven by large κ (Section 4.2), which in turn results in large δ_{15° We add this contribution to Equation 12 using $\frac{\partial \delta_{15^\circ}^{+}}{\partial x} \propto \kappa$ resulting in:

$$\delta_{15^\circ} = \int A\kappa - B\kappa \frac{\partial \delta_{15^\circ}^{-}}{\partial \varepsilon} dx \tag{15}$$

where A and B are functions of the current microstructural state as material traverses through the deformation zone. It must be realized that Equation 15 is strictly valid in regimes where GNDRX is activated. We again assume that strain gradients in the deformation zone of machining are linear, whereby $\varepsilon = \varepsilon_f \frac{x}{h}$ where ε_f is the total strain imposed on the material forming the chip and h is the thickness of the deformation zone (Fig. 27).

Therefore,

$$dx = \frac{h}{\varepsilon_f} d\varepsilon \tag{16}$$

Substituting Equation (16) in (15), we get,

$$\delta_{15^\circ} = \kappa \int \left(A - B \frac{\partial \delta_{15^\circ}^{-}}{\partial \varepsilon} \right) \frac{h}{\varepsilon_f} d\varepsilon \tag{17}$$

Here, $\kappa\left(\propto \frac{\partial \varepsilon}{\partial x}\right)$ was pulled out of the integral because, $\frac{\partial \varepsilon}{\partial x}$ (strain gradient) was assumed to be constant in the narrow deformation zone. We further note that for the same ε_f, $h \propto a_0$ or $h = C' a_0$ [31]. Substituting this in Equation 17, we get:

$\delta_{15^\circ} = \kappa \int \left(A - B \frac{\partial \delta_{15^\circ}}{\partial \varepsilon} \right) \frac{C' a_0}{\varepsilon_f} d\varepsilon$, or:

$$\frac{\delta_{15^\circ}}{a_0} = \kappa \int \left(A - B \frac{\partial \delta_{15^\circ}}{\partial \varepsilon} \right) \frac{C'}{\varepsilon_f} d\varepsilon \qquad (18)$$

Therefore, Equation 18 implies that for the same amount of strain imposed , $\frac{\delta_{15^\circ}}{a_0} \propto \kappa$. κ was empirically measured using the TSL OIM 5.0 software by finding the misorientation gradient along pathlines close to the deformation zone. Several measurements were made for repeatability. Fig. 37a shows the variation of $\frac{\delta_{15^\circ}}{a_0}$ with respect to κ corroborating the hypothesis that strain gradients (resulting in crystallographic curvature) indeed play a decisive role in steering microstructure evolution during SPD in small length scales. The line $\frac{\delta_{15^\circ}}{a_0} = 4 \times 10^{-6} \kappa$ in Fig. 37a, captures the microstructure evolution behavior with high R^2 (= 0.92).

It should be noted that $\kappa \propto \frac{\partial \varepsilon}{\partial x}$ was used repeatedly in this section. This is a somewhat simplified notion as κ will not be proportional to $\partial \varepsilon / \partial x$ for all points within the orientation space during machining (Refer section 2.5.1). Such instances were isolated while calculating statistics of microstructure resulting in the chip from those in which $\kappa \propto \frac{\partial \varepsilon}{\partial x}$ by realizing that

prominent grain boundaries in the deformation zone such as those in Fig. 35 will be absent in the former based on the arguments presented in this section.

4.2.4.4 Length scale-dependent response as a function of prior deformation It remains to be seen how pre-straining influences the ensuing crystallographic curvature κ during machining which gives rise to GNDRX (section 4.2.4.2). Interestingly, κ could not be written as a function of the set depth of cut (a_0) alone because pre-rolled conditions exhibit a significantly higher κ value than annealed conditions (Fig. 37b) during machining. We note that there is a material length ($\hat{l}$) associated with the state of the bulk with which, the strain gradient must be normalized [24] in order to quantify its influence. This length depends on the mean spacing between dislocations $\hat{l} \propto \frac{1}{\rho}$ where ρ is the dislocation density. Therefore, a pre-strained bulk (with higher ρ) will feature a smaller $\hat{l}$. Based, on this argument, $\kappa\hat{l}$ ($\propto \frac{\kappa}{\rho}$) can be hypothesized to scale better with respect to the set depth of cut, thereby making it a better measure of the associated strain gradients.

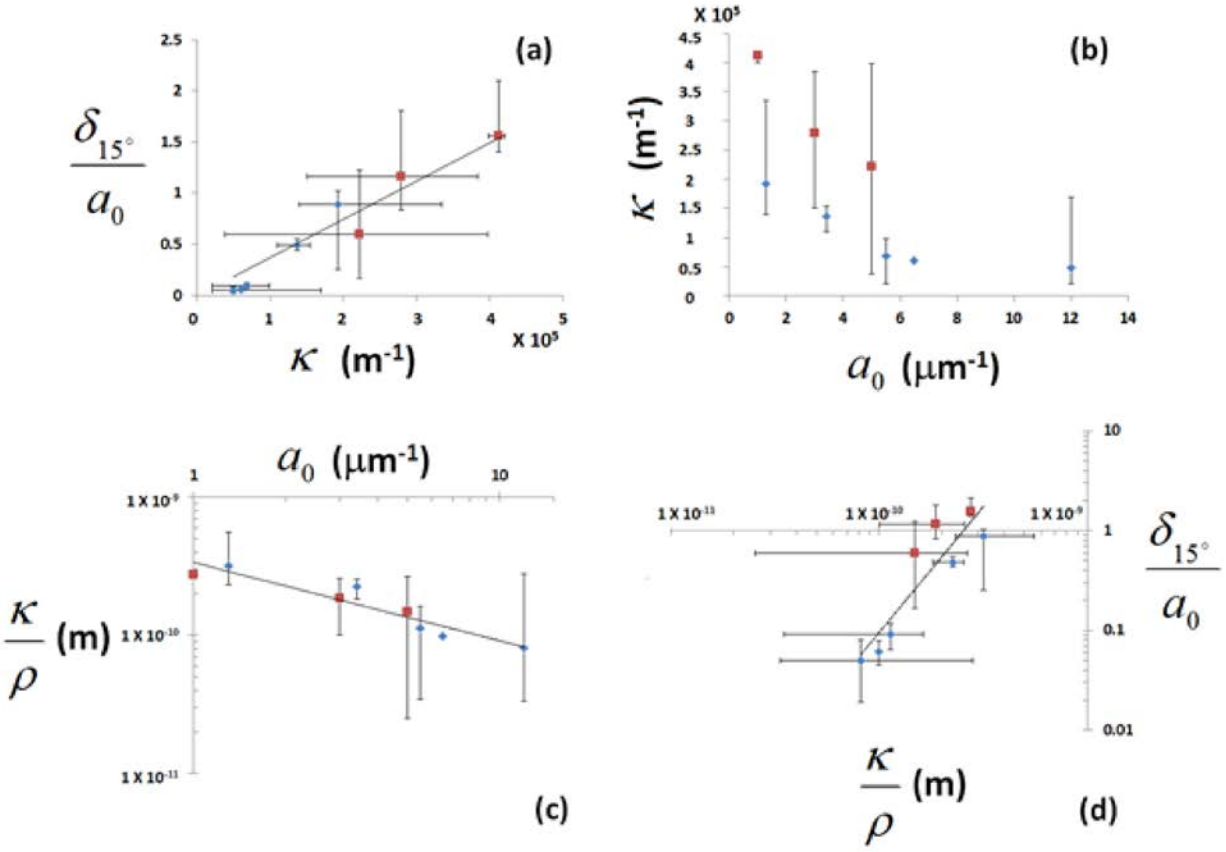

Figure 37: (a) Linear variation of $\frac{\delta_{15^\circ}}{a_0}$ with respect to the crystallographic curvature κ (radians/m) set depth of cut of machining. (b) Variation of κ with respect to set depth of cut a_0. (c) Variation of $\frac{\kappa}{\rho}$ with respect to a_0. (d) Variation of $\frac{\delta_{15^\circ}}{a_0}$ with respect to $\frac{\kappa}{\rho}$. The error bars show scatter in data. Red points (square) belong to pre-strained specimens; blue points (diamond) belong to annealed specimens.

Incorporating this, we find that $\kappa\hat{l}$ indeed scales as $\frac{\kappa}{\rho} = 3\times10^{-10} a_0^{-0.57}$ with high R^2 (= 0.89) as shown in Fig. 37c. It is interesting to find that $\kappa\hat{l} \propto a_0^{-0.57}$ as opposed to the conventionally anticipated $\kappa\hat{l} \propto a_0^{-1}$ [24]. A possible reason can be the more homogenous plane strain simple shear deformation state prevailing in the deformation zone of LSM as opposed to

the three dimensional deformation geometries involved in indentation. Fig. 37d shows the variation of $\frac{\delta_{15^\circ}}{a_0}$ with respect to $\frac{\kappa}{\rho}$, revealing a power law relationship ($\frac{\delta_{15^\circ}}{a_0} = 1\times10^{24}\left(\frac{\kappa}{\rho}\right)^{2.5}$, R^2 = 0.81). This exercise establishes the utility of $\frac{\kappa}{\rho}$ as a parameter for predicting mechanics of microstructure evolution during SPD in small length scales.

In order to identify the influence of pre-straining, we note that rolling will essentially cause crystallographic texturing of the bulk material, albeit in limited extent in the present case owing to the small reduction ratio employed (rolling reduction = 26%). However, this might be sufficient to result in the onset of crystallographic reorientation of the sub-grains (dislocation cells surrounded by GNBs) to a rolling type texture [47]. Subsequent simple shear during machining might interfere with this texture and result in quicker rates of crystallographic reorientation in a manner somewhat similar to that described in Ref. [46]. Preliminary analysis to test this hypothesis was performed using a Visco Plastic Self Consistent framework based simulation of simple shear (machining) and rolling preceded by simple shear. It was seen that average crystallographic rotation was indeed larger in the latter as opposed to the former in the beginning of the simple shear processes. This accelerated rate of rotation would manifest in larger κ in pre-strained samples.

4.2.5 Effect of length scales on microstructure evolution during SPD on other metals

In order to validate the trends of length scale inflicted microstructure evolution during SPD in Ni 200, micro machining was performed on other prototypical FCC metals (OFHC Cu and Al 1100). This section of the thesis provides a brief summary of the results obtained. Additionally

an attempt to quantify the influence of material parameter Stacking Fault Energy (SFE) has been described in this chapter.

4.2.5.1 OFHC Cu OFHC Cu was annealed at 973 K for 2 hours resulting in a grain size of ~ 50 μm. Samples made with annealed OFHC Cu then orthogonally micro machined with a nominally sharp diamond tool that was advanced at the same speed V = 150 μm/s. a_0 was set between 13 μm and 2 μm. *in-situ* mechanical characterization of the deformation zone was performed during machining by DIC using the same approach as given in section 3.1.1.1. Microstructure response of the material forming was quantified using OIM by EBSD on partially detached chip specimens using the technique described in section 4.2.

Effective strains imposed on the chips were calculated using: $\varepsilon = \frac{\cos\alpha}{\sqrt{3}\sin\varphi\cos(\varphi-\alpha)}$, where φ is given by $\tan\varphi = \frac{a_0/a_c\cos\alpha}{1-a_0/a_c\sin\alpha}$. A value of ~3.5 was seen across different length scales studied. Results of mechanical characterization of the deformation zone are shown in Fig. 38. Machining OFHC Cu resulted in a deformation zone ~ 300 nm, significantly smaller than that in Ni 200 (~ 2 μm; Fig. 28) under equivalent conditions V = 150 μm/s, a_0 = 6.5 μm.

Fig. 39 shows the OIM of the partially attached chip specimens created by machining OFHC Cu with V = 150 μm/s and a_0 = ~ 13 μm and 4 μm respectively. In the larger length scale (a_0 = ~ 13 μm), the microstructure undergoes significant grain refinement resulting in UFG microstructures. The deformation zone (Fig. 39a) reveals formation of isolated pancake shaped grain structures, possibly from formation and shear of isolated grains formed

in the initial stages of deformation by Continuous Dynamic Recrystallization (CRDX). This is similar to observations made in Ni 200 while machining with a_0 = ~ 12 μm and V = 150 μm/s (Fig. 34). Close the trailing edge of the deformation zone (Fig. 39a), these grains assume a serrated shape suggesting simultaneous activation of Geometric Dynamic Recrystallization (GDRX) contributing to microstructure evolution and refinement. It is interesting to note that even at large length scales (a_0 = ~ 13 μm) microstructure evolution involving refinement in the chip does not seem to be complete as evidenced from the presence of isolated pancake grains close to the top in Figs. 39a and 39b. δ_{15° and δ_{2°quantified from the OIM data using the technique described in section 4.2 revealed values of ~3 μm and ~1.3 μm, respectively. A mean misorientation $\langle\theta\rangle$= ~ 30° was observed.

Comparing with a_0 = ~ 13 μm, microstructures created from OFHC Cu by machining with a_0 = 4 μm reveal significantly retarded refinement. Here, the entire width of the chip was composed of one large grain interspersed with island like grains and other high angle and low angle dislocation structures. Comparison with microstructure in the chip created by machining Ni 200 under similar conditions (V = 150 μm/s and a_0 = 3.4 μm) shows that the effect of length scales is significantly stronger in OFHC Cu as opposed to Ni 200. δ_{15° and δ_{2°quantified from OIM using the same technique (section 4.2) revealed values of ~6 μm and ~1.8 μm, respectively. This change was visible in the misorientation distribution that was biased towards significantly smaller angles ($\langle\theta\rangle$= ~ 15° observed), compared with a_0= ~13 μm (~ 30°).

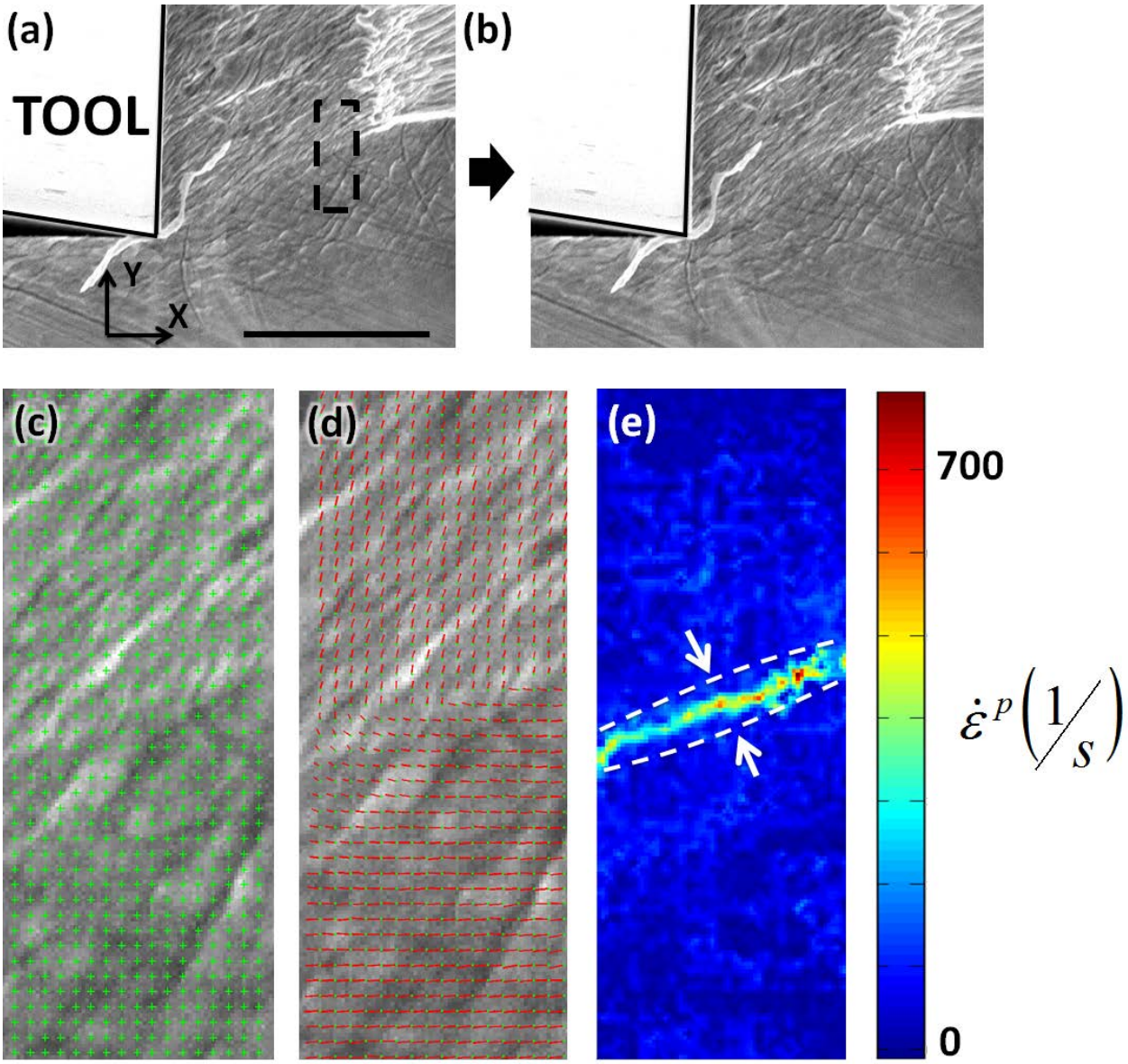

Figure 38: *in-situ* mechanical characterization of the deformation zone while machining OFHC Cu using DIC (V = 150 μm/s, a_0 = 6.5 μm). DIC was performed on the sequence of images illustrated in (a) through (b) on a grid (c). (d) Displacement field obtained from DIC overlaid on the grid. (e) Spatially and temporally differentiated and subsequently processed displacement to show effective strain rate field. The deformation zone (dash lines in (e)) thickness marked using white arrows in (e) was ~300 nm.

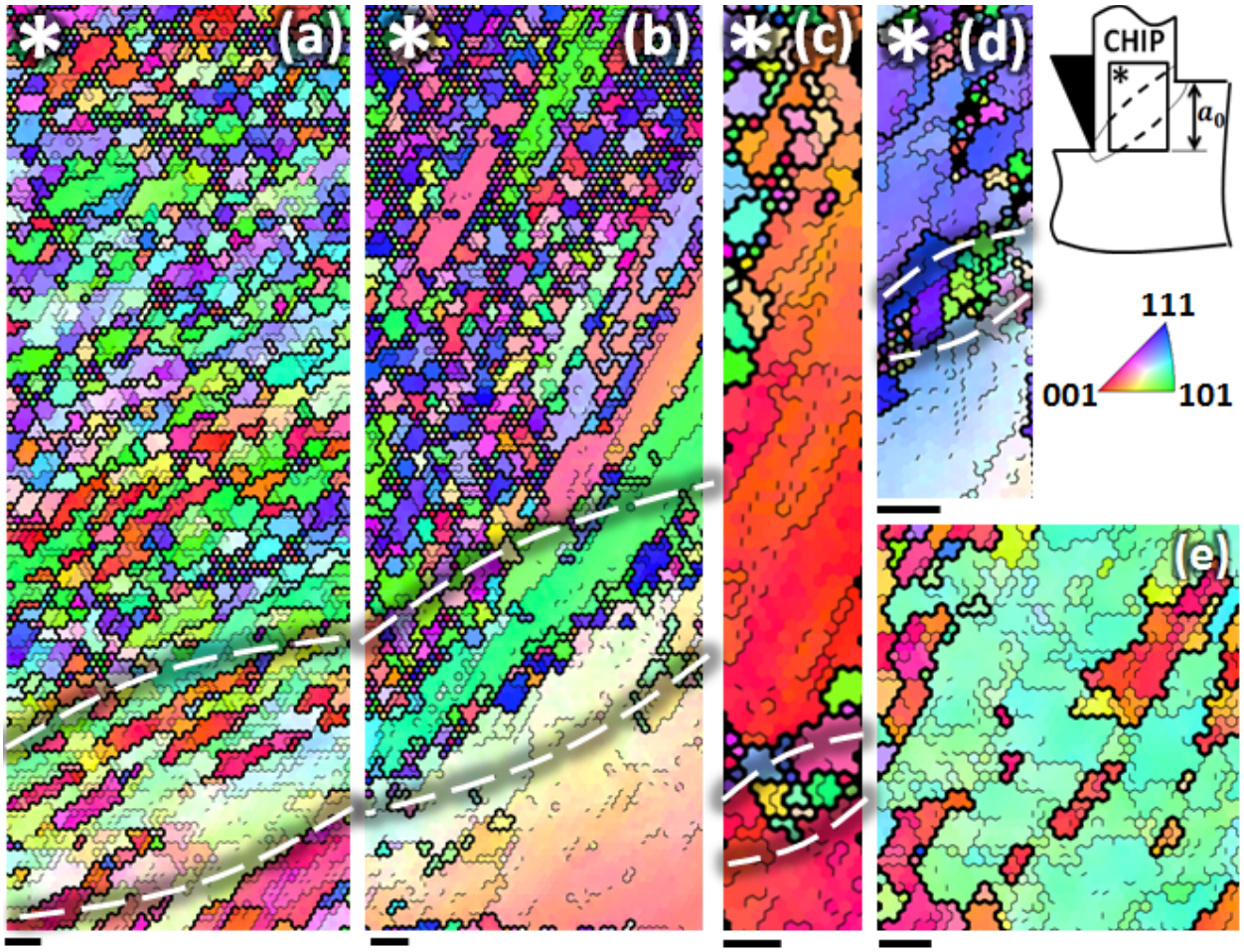

Figure 39: Inverse Pole Figures obtained from Orientation Image Microscopy of partially detached chip specimens obtained during machining of annealed OFHC Cu with V=150 μm/s at a_0= (a) and (b) ~13 μm (c) and (d) 4 μm (e) IPF within the chip created by machining of OFHC Cu with a_0 = 4 μm showing completely recrystallized microstructures. Refer insets in top right for spatial configurations of zones within partially detached chip specimens where OIM was performed and color code. All scale bars are 1 μm. Dashed lines show approximate location of deformation zone.

Similar to a_0 = 4 μm, chips created by machining OFHC Cu with a_0 = 2 μm at V = 150 μm/s reveal a near complete lack of microstructure refinement with the entire thickness of the chip composed of one grain. Furthermore, the chip microstructure was again seen to be heavily defected and interspersed with stray high as well as low angle dislocation boundaries. δ_{15° and

δ_{2°quantified from OIM revealed values of ~5.3 μm and ~0.9 μm, respectively. A mean misorientation of $\langle\theta\rangle$ = ~ 16° was seen.

Comparison of microstructures created from OFHC Cu by micromachining with $a_0 \leq$ ~ 4 μm (Figs. 39e and 40) suggests a similar microstructure evolution in the two cases. Mechanistically, it is possible that Cu is within the length scale zone ($a_0 \leq$ ~4 μm) in which lack of microstructure refinement due to Geometrically Necessary Dynamic Recrystallization (GNDRX) manifests. However, it must be noted that within this length scale regime, the chip is consistently composed of very few grains. This is likely to result in significant scatter and possible underestimation. Based on the trends observed in Ni 200 and OFHC Cu, it can be hypothesized that in the regime in which GNDRX is active, lack of microstructure refinement will result in a surjective (and possibly bijective) mapping of the initial grains of a polycrystal to a final grain structure in the chip during machining. While this hypothesis was not validated here, preliminary investigations do support this view. Fig. 40 (top right and bottom left) shows the grain structure of the chips created from grains that had the same starting orientation. Both chips reveal average orientations very close to each other. By extrapolation, this implies the same final orientation starting from the same initial orientation in the polycrystal during machining.

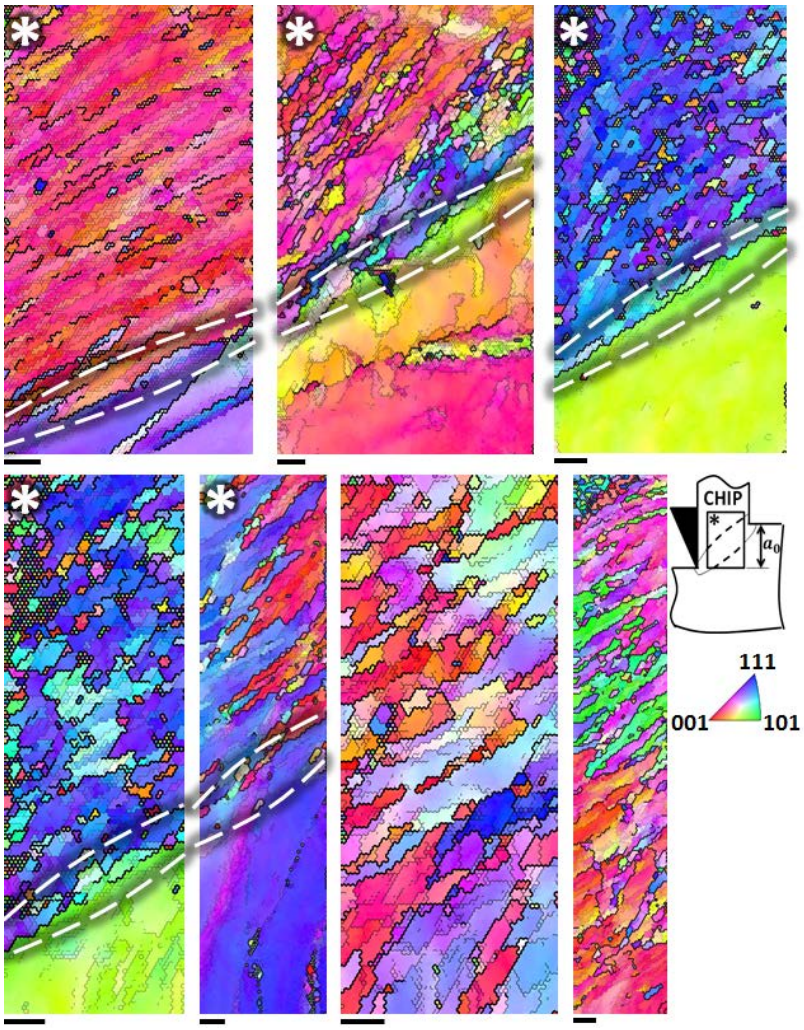

Figure 40: Inverse Pole Figures obtained from Orientation Image Microscopy of partially detached chip specimens obtained during machining of annealed OFHC Cu with V=150 μm/s at a_0= 2 μm (top row, bottom left and bottom center left). IPFs of chips created using the same conditions (bottom right and bottom center right). Refer insets in top right for spatial configurations of zones within partially detached chip specimens where OIM was performed and color code. All scale bars are 1 μm. Dashed lines point approximate location of deformation zone.

4.2.6.2 Al 1100 This section describes the effect of length scales on microstructure evolution due to SPD on Al 1100 while machining. For achieving this, machining was performed on annealed Al 1100. Speed of tool advance was set at V = 150 μm/s and a_0 was set between 10 μm and 1

μm as specified. *In-situ* mechanical characterization of the deformation zone was performed using DIC while machining Al 1100 with V = 150 μm/s and a_0 = 10 μm. A somewhat more diffuse deformation compared with zone with a thickness of ~ 4 μm was seen. This is somewhat more diffuse than Ni 200 under similar conditions (~ 3.20 μm for a_0 = 10 μm, Fig. 28). Effective strains imposed on the chips were calculated using: $\varepsilon = \frac{\cos\alpha}{\sqrt{3}\sin\varphi\cos(\varphi-\alpha)}$, where φ is given by $\tan\varphi = \frac{a_0/a_c\cos\alpha}{1-a_0/a_c\sin\alpha}$ and value of ~2.5 was seen across different length scales studied here.

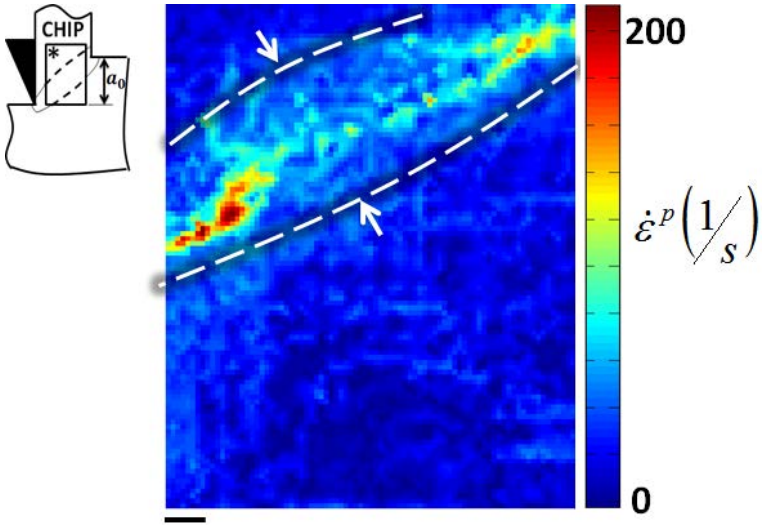

Figure 41: *in-situ* mechanical characterization of the deformation zone during machining of Al 1100. The strain rate field was acquired from a region, the approximate location of which is shown in the box within the inset on top left. Machining parameters were: V = 150 μm/s, a_0 = 10 μm. Scale bar at the bottom left is 1 μm.

Fig. 42 shows results of OIM on partially detached chip specimens created by machining Al 1100. It is evident from a qualitative inspection of the OIMs that Al 1100 exhibits a very subdued effect of length scales on microstructure evolution during SPD, exhibiting $\delta_{15^\circ}(\delta_{2^\circ})$ values of 0.81 μm (0.60 μm), 1.2 μm (0.7 μm) and 1.2 μm (0.6 μm) for a_0 = 5 μm, 3 μm and 1 μm, respectively. Furthermore, the chip microstructures exhibit similar mean misorientations of $\langle\theta\rangle$ = ~ 35°, ~ 30° and ~ 32° for a_0 = 5 μm, 3 μm and 1 μm, respectively.

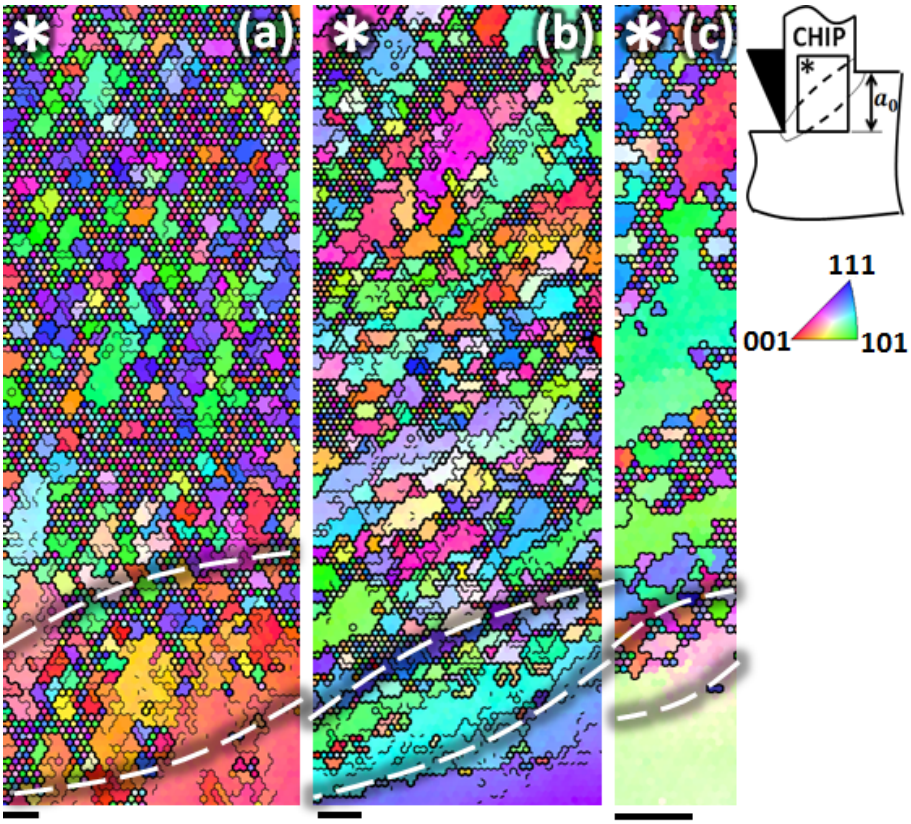

Figure 42: Inverse Pole Figures obtained from Orientation Image Microscopy of partially detached chip specimens obtained during machining of annealed Al 1100 with V=150 μm/s at (a) a_0= 5 μm, (b) a_0= 3 μm and (c) a_0= 1 μm. Refer insets in top right for spatial configurations of zones within partially detached chip specimens where OIM was performed and color code. All scale bars are 1 μm. Dashed lines point approximate location of deformation zone.

The aforementioned suppression of length scale inflicted phenomena in small length scales during machining of Al 1100 could be a manifestation of several factors (including material parameters like Stacking Fault Energy, etc.). Mechanistically, this suppression might result from a more diffuse deformation zone, which develops during machining of Al 1100 as opposed to Ni 200 or OFHC Cu. A larger spatial expanse of the deformation zone can be expected to interfere with microstructure evolution mechanisms in a manner similar to that described in 4.2.5.2. Validation of this hypothesis necessitates accurate measurement of δ_{GNB} as a function of strain imposed in Al 1100 and was not pursued here. However, accuracy of this argument is supported by rampant GNDRX in OFHC Cu, where a significantly thinner deformation zone was seen (Fig. 38) for the same machining parameters when compared with Ni 200 (Figs. 27 and 28) and Al 1100 (Fig. 41).

5.0 CONCLUSIONS AND FUTURE WORK

We have demonstrated a novel influence of length scales on microstructure evolution during Severe Plastic Deformation by performing machining on three commercially pure Face Centered Cubic metals (Ni 200, Oxygen Free High Conductivity Cu and Al 1100). In this, conventionally observed refinement during SPD is replaced by lack of refinement, resulting in large grains. This anomalous lack of refinement was attributed to a coupled effect of high strain gradients and small deformation volumes in small length scales. It was hypothesized that when volume undergoing deformation approaches that associated with characteristic dislocation structures which form during SPD in conventional settings (large length scales), the mechanisms of microstructure evolution involving refinement are hindered. While the aforementioned effect was rampant in OFHC Cu, it was almost absent in Al 1100. By characterizing the deformation zone of machining *in-situ* in OFHC Cu as well as Al 1100, this effect was attributed to the spatially diffuse deformation zone, which naturally develops during machining.

The flow fields in the deformation zone of machining were characterized using Digital Image Correlation. This was done *in-situ* using a Scanning Electron Microscope as the deformation zone flow fields are often not resolvable optically, especially in small length scales. To do this, a deformation stage capable of operating within the chamber of a SEM was designed and fabricated in house. Subsequently, techniques for performing *in-situ* DIC of machining were also established. Experimental methods used for performing DIC were initially established by

studying microstructure evolution during macro scale machining. Specifically, evolution of crystallographic textures during macro scale machining was studied and modeled. Eventually, the established DIC techniques were advanced to handle challenges of *in-situ* SEM DIC.

With the aim of making this study more practically relevant, the following future directions are proposed:

1. The research described in this thesis demonstrated an anomalous lack of microstructure refinement. Although this effect was modeled phenomenologically (section 4.2.5.4) its mechanistic underpinnings are still not clear. Only a successful effort in this direction will make these insights generalizable to other single-phase metals and possibly more sophisticated alloys.
2. Machining is a mainstay of fabricating metallic components. During the process, a new surface is left in the wake of the tool. It has been seen that the deformation zone of machining contiguously extends under this surface. As a consequence, microstructure within this zone (and the integrity of the resulting surface) is directly inherited from the thermomechanical conditions prevalent in the deformation zone of machining. While a switchover in microstructure evolution mechanisms has been described in this thesis, its implications on the integrity of the surface created during micro machining were not studied. It is envisioned that insights gained form this research direction will have significant practical implications.
3. The aforementioned study is a first step in understanding the effect of length scales on microstructure evolution during SPD and it deals exclusively with FCC metals. A useful application of insights gained from this research is a study of effect of length scales on microstructure evolution in Hexagonally Close Packed metals which have wide spread

technological applications (e.g. Mg, Ti, Zr, etc.). For example, it has been seen that the anisotropic nature of Mg prohibits it from forming without failure at room temperatures [29]. However, this anisotropy has been shown to disappear at small (nano) length scales during micro pillar compression tests [48] resulting in significantly larger ductility. It will be interesting to see whether the aforementioned isotropy in mechanical behavior will sustain in Mg alloys in small length scales during micro machining. Given that Mg has highest specific strength among all metals that have common industrial application (e.g. in automobile industry, etc.) successful demonstration of the same will have tremendous implications.

APPENDIX A

DIGITAL IMAGE CORRELATION (DIC)

DIC, equivalently known as Particle Imaging Velocimetry (PIV) is a non-contact technique of tracking particles in 2D or 3D motion. The technique relies on acquisition of the instantaneous positions of particles (which might be in motion) in a sequence of high speed images. The displacement of particles across pairs of images within the sequence is then quantified using image correlation algorithms from which a displacement field in the region of interest is composed. By differentiating this displacement field with respect to time, a velocity vector field is generated which is further processed (by differentiating with respect to space) to produce velocity gradient fields, etc.

This section provides an overview of the software used to perform DIC. The software was adapted from freely downloadable open source MATLAB software (Ref. [49]) which relied of the normxcorr2.m (an inbuilt MATLAB function). This function uses Fast Fourier Transforms for DIC, exploiting the fact that the convolution function (which is typically used to perform correlation) can be decomposed as a Fourier Transform [50]. Figure 11 shows the sequence of primary steps that need to be performed to perform mechanical characterization from the sequence of recorded images.

A.1 filelist_generator.m

This subroutine automatically identifies a sequence of image files within the current working directory by finding the repetitive pattern within the names of the files in the sequence. The subroutine needs the name of the first file as input to do this. Subsequently, it archives all filenames within the sequence in a new file (‘filenamelist.mat’ by default). For e.g. if the sequence of high speed images goes as: p001.tif, p002.tif and so on, this part of the software identifies all files p001.tif – p00N.tif in the folder (with the same motif ‘p’ after ‘p001.tif’ is input) and saves these names in file ‘filenamelist.mat’ in that order.

```
function [FileNameBase,PathNameBase,filenamelist]=filelist_generator

% Code to construct a list of 9999 or less filenames
% Programmed by Rob, changed by Chris. Automatic filelist generation
% and image time aquisition added by Chris.
% Last revision: 12/25/06

filenamelistmode = menu(sprintf('How do you want to create the
filenamelist?'),...
    'Manually','Automatically','Cancel');
if filenamelistmode==3
    return
end
if filenamelistmode==2
    [FileNameBase,PathNameBase,filenamelist]=automatically;
end
if filenamelistmode==1
    [FileNameBase,PathNameBase,filenamelist]=manually;
end

[FileNameBase,PathNameBase,filenamelist]=imagetime(FileNameBase,PathNameBase,
filenamelist);

%  ------------------------------------------------------
%  filenamelistmode=2 (automatically) was chosen

function [Firstimagename,ImageFolder,filenamelist]=automatically

[Firstimagename ImageFolder]=uigetfile('*.TIF','Open First Image');
if Firstimagename~~[];
    cd(ImageFolder);
end
```

```
if Firstimagename~~[];
    % Get the number of image name
    letters=isletter(Firstimagename);
    Pointposition=findstr(Firstimagename,'.');
    Firstimagenamesize=size(Firstimagename);
    counter=Pointposition-1;
    counterpos=1;
    letterstest=0;
    while letterstest==0
        letterstest=letters(counter);
        if letterstest==1
            break
        end
        Numberpos(counterpos)=counter;
        counter=counter-1;
        counterpos=counterpos+1;
        if counter==0
            break
        end
    end

    Filename_first = Firstimagename(1:min(Numberpos)-1);
    Firstfilenumber=Firstimagename(min(Numberpos):max(Numberpos));
    Lastname_first =
Firstimagename(max(Numberpos)+1:Firstimagenamesize(1,2));
    Firstfilenumbersize=size(Firstfilenumber);
    onemore=10^(Firstfilenumbersize(1,2));
    filenamelist(1,:)=Firstimagename;

    Firstfilenumber=str2num(Firstfilenumber);
    u=1+onemore+Firstfilenumber;
    ustr=num2str(u);
    filenamelist(2,:)=[Filename_first ustr(2:Firstfilenumbersize(1,2)+1)
Lastname_first];
    numberofimages=2;

    counter=1;

    while exist(filenamelist((counter+1),:),'file') ==2;
        counter=counter+1;
        u=1+u;
        ustr=num2str(u);
        filenamelist(counter+1,:)=[Filename_first
ustr(2:Firstfilenumbersize(1,2)+1) Lastname_first];
        if exist(filenamelist((counter+1),:),'file') ==0;
            warning('Last image detected')
            filenamelist(counter+1,:)=[];
            break
        end
    end
end
[FileNameBase,PathNameBase] = uiputfile('filenamelist.mat','Save as
"filenamelist" in image directory (recommended)');
cd(PathNameBase)
save(FileNameBase,'filenamelist');
```

```
%  --------------------------------------------------------
function [FileNameBase,PathNameBase,filenamelist]=manually;
% Prompt user for images to be used for analysis

prompt = {'Enter number of first image (i.e. "3" for PIC00003):','Enter
number of last image (i.e. "100" for PIC00100):'};
dlg_title = 'Input images to be used for the analysis';
num_lines= 1;
def     = {'1','100'};
answer = inputdlg(prompt,dlg_title,num_lines,def);
F2 = str2num(cell2mat(answer(1,1)));
F = str2num(cell2mat(answer(2,1)));

if F >= 10000
    error0 = menu('!!! ERROR - Code will only work properly for 9999 or less
picture files !!!','Restart');
    return
end

% Choose first name of images
G = 'PIC1';
prompt = {'Enter Image Name (first 4 letters):'};
dlg_title = 'Input images to be used for the analysis';
num_lines= 1;
def     = {'PIC1'};
answer = inputdlg(prompt,dlg_title,num_lines,def);
G = cell2mat(answer(1,1));

E='.tif';

namelist(1:F-F2+1,1)=G(1,1);
namelist(1:F-F2+1,2)=G(1,2);
namelist(1:F-F2+1,3)=G(1,3);
namelist(1:F-F2+1,4)=G(1,4);

% create the numberlist
num=((10000+F2):(10000+F))';

% Creation of final results
filenamelist=namelist;
str=num2str(num);
filenamelist(:,5:8)=str(:,2:5);

filenamelist(1:F-F2+1,9)=E(1,1);
filenamelist(1:F-F2+1,10)=E(1,2);
filenamelist(1:F-F2+1,11)=E(1,3);
filenamelist(1:F-F2+1,12)=E(1,4);


% Save results
[FileNameBase,PathNameBase] = uiputfile('filenamelist.mat','Save as
"filenamelist" in image directory (recommended)');
cd(PathNameBase)
save(FileNameBase,'filenamelist');
```

```
%  ---------------------------------------
% Extract the time from images?

function
[FileNameBase,PathNameBase,filenamelist]=imagetime(FileNameBase,PathNameBase,
filenamelist)

selection_time_image = menu(sprintf('Do you also want to extract the time
from images to match stress and strain?'),'Yes','No');

if selection_time_image==1

    % Loop through all images in imagetimelist to get all image capture times

    [ri,ci]=size(filenamelist);

    o=waitbar(0,'Extracting the image capture times...');

    for q=1:ri

        waitbar(q/ri);
        info=imfinfo(filenamelist(q,:));
        time=datevec(info.FileModDate,13);
        seconds(q)=time(1,4)*3600+time(1,5)*60+time(1,6);

    end

    close(o)

    % Configure and then save image number vs. image capture time text file

    im_num_im_cap_time=[(1:ri)' seconds'];
    save time_image.txt im_num_im_cap_time -ascii -tabs

end
```

A.2 grid_generator.m

This subroutine selects a grid of points within the Region Of Interest (ROI) in an image. The user therefore chooses an image in the sequence (described in Section A.1) and then demarcates a ROI within that image. Subsequently, the image correlation algorithm attempts to track the position of each point in the grid in the consecutive images. Parameters associated with the grid (e.g. spacing between grid points, shape of ROI, etc.) are provided by the user.

```
function [grid_x,grid_y]=grid_generator(FileNameBase,PathNameBase);

% Code to generate the DIC analysis grid
% Completely rewritten by Chris
% Programmed first by Dan and Rob
%
% Last revision: 12/27/06

% The grid_generator function will help you create grids of markers. The
% dialog has different options allowing you to create a marker grid which is
rectangular,
% circular, a line or two rectangels of a shape or contains only of two
% markers. After choosing one of the shapes you will be asked for the base
% image which is typically your first image. After opening that image you
% will be asked to click at the sites of interest and the markers will be
% plotted on top of your image. You can choose if you want to keep these
% markers or if you want to try again.
% It has to be noted that you can
% always generate your own marker positions. Therefore the marker position
% in pixel has to be saved as a text based format where the x-position is
% saved as grid_x.dat and the y-position saved as grid_y.dat.
%



% Prompt user for base image
if exist('FileNameBase')==0
[FileNameBase,PathNameBase] = uigetfile( ...
    {'*.bmp;*.tif;*.jpg;*.TIF;*.BMP;*.JPG','Image files
(*.bmp,*.tif,*.jpg)';'*.*',  'All Files (*.*)'}, ...
    'Open base image for grid creation');

end
cd(PathNameBase)
im_grid = imread(FileNameBase);
```

```
[grid_x,grid_y,FileNameBase,PathNameBase] = gridtypeselection(FileNameBase,
PathNameBase, im_grid);

close all

%------------------------------
%
% Decide which type of grid you want to create

function [grid_x,grid_y,FileNameBase,PathNameBase] =
gridtypeselection(FileNameBase, PathNameBase, im_grid);

hold off
imshow(im_grid,'InitialMagnification',100);

gridselection = menu(sprintf('Which type of grid do you want to use'),...
    'Rectangular','Circular','Two Markers','Line','Two Rectangles of
Markers','Cancel');


if gridselection==1
    [grid_x,grid_y,FileNameBase,PathNameBase] = rect_grid(FileNameBase,
PathNameBase, im_grid);
    return
end

if gridselection==2
    [grid_x,grid_y,FileNameBase,PathNameBase] = circ_grid(FileNameBase,
PathNameBase, im_grid);
    return
end

if gridselection==3
    [grid_x,grid_y,FileNameBase,PathNameBase] = twop_grid(FileNameBase,
PathNameBase, im_grid);
    return
end

if gridselection==4
    [grid_x,grid_y,FileNameBase,PathNameBase] = line_grid(FileNameBase,
PathNameBase, im_grid);
    return
end

if gridselection==5
    [grid_x,grid_y,FileNameBase,PathNameBase] = torect_grid(FileNameBase,
PathNameBase, im_grid);
    return
end

if gridselection==6
    return;
end
```

```
%------------------------------
%
% Define two rectangles and add them to one marker array

function [grid_x,grid_y,FileNameBase,PathNameBase] =
tworect_grid(FileNameBase, PathNameBase, im_grid);

[grid_x1,grid_y1,FileNameBase,PathNameBase] = rect_grid(FileNameBase,
PathNameBase, im_grid);
imshow(im_grid,'truesize');
[grid_x2,grid_y2,FileNameBase,PathNameBase] = rect_grid(FileNameBase,
PathNameBase, im_grid);

grid_x1=reshape(grid_x1,[],1);
grid_x2=reshape(grid_x2,[],1);
grid_y1=reshape(grid_y1,[],1);
grid_y2=reshape(grid_y2,[],1);

grid_x=[grid_x1; grid_x2];
grid_y=[grid_y1; grid_y2];

imshow(im_grid,'truesize');
hold on
plot(grid_x,grid_y,'.')
title(['Selected grid has ',num2str(length(grid_x)), ' rasterpoints'])    %
plot a title onto the image

% Accept the chosen markers, try again or give up

confirmcircselection = menu(sprintf('Do you want to use these markers?'),...
    'Yes','No, try again','Go back to grid-type selection');

if confirmcircselection==2
    close all
    hold off
    imshow(im_grid,'truesize');
    tworect_grid(FileNameBase, PathNameBase, im_grid);
end

if confirmcircselection==3
    close all
    gridtypeselection(FileNameBase, PathNameBase, im_grid);
end

if confirmcircselection==1
    close all
    save grid_x.dat grid_x -ascii -tabs
    save grid_y.dat grid_y -ascii -tabs
end

%------------------------------
%
```

```
% Define line and create markers

function [grid_x,grid_y,FileNameBase,PathNameBase] = line_grid(FileNameBase,
PathNameBase, im_grid);

title(sprintf('Pick two points on the sample.') )

[x(1,1),y(1,1)]=ginput(1);
hold on
plot(x(1,1),y(1,1),'+g')

[x(2,1),y(2,1)]=ginput(1);
plot(x(2,1),y(2,1),'+g')


linelength=sqrt((x(2,1)-x(1,1))*(x(2,1)-x(1,1))+(y(2,1)-y(1,1))*(y(2,1)-
y(1,1)));
lineslope=(y(2,1)-y(1,1))/(x(2,1)-x(1,1));
intersecty=y(1,1)-lineslope*x(1,1);
ycalc=zeros(2,1);
ycalc=lineslope*x+intersecty;
plot(x(:,1),ycalc(:,1),'-b')


prompt = {'Enter the number of intersections between markers on the line:'};
dlg_title = 'Input for grid creation';
num_lines= 1;
def     = {'30'};
answer = inputdlg(prompt,dlg_title,num_lines,def);
linediv = str2num(cell2mat(answer(1,1)));
linestep=((max(x)-min(x))/linediv);
grid_x(1:linediv+1)=min(x)+linestep*(1:linediv+1)-linestep;
grid_y=lineslope*grid_x+intersecty;

plot(grid_x,grid_y,'ob')
title(['Selected grid has ',num2str(linediv), ' rasterpoints'])    % plot a
title onto the image

% Accept the chosen markers, try again or give up

confirmcircselection = menu(sprintf('Do you want to use these markers?'),...
    'Yes','No, try again','Go back to grid-type selection');

if confirmcircselection==2
    close all
    hold off
    imshow(im_grid,'truesize');
    twop_grid(FileNameBase, PathNameBase, im_grid);
end

if confirmcircselection==3
    close all
    gridtypeselection(FileNameBase, PathNameBase, im_grid);
end
```

```
if confirmcircselection==1
    save grid_x.dat grid_x -ascii -tabs
    save grid_y.dat grid_y -ascii -tabs
end

%-------------------------------
%
% Select two markers

function [grid_x,grid_y,FileNameBase,PathNameBase] = twop_grid(FileNameBase,
PathNameBase, im_grid);

title(sprintf('Pick two points on the sample.') )

[x(1,1),y(1,1)]=ginput(1);
hold on
plot(x(1,1),y(1,1),'+g')

[x(2,1),y(2,1)]=ginput(1);
plot(x(2,1),y(2,1),'+g')

% Accept the chosen markers, try again or give up

confirmcircselection = menu(sprintf('Do you want to use these two
markers?'),...
    'Yes','No, try again','Go back to grid-type selection');

if confirmcircselection==2
    close all
    hold off
    imshow(im_grid,'truesize');
    twop_grid(FileNameBase, PathNameBase, im_grid);
end

if confirmcircselection==3
    close all
    gridtypeselection(FileNameBase, PathNameBase, im_grid);
end

if confirmcircselection==1
    grid_x=x;
    grid_y=y;
    save grid_x.dat grid_x -ascii -tabs
    save grid_y.dat grid_y -ascii -tabs
end
%-------------------------------
%
% Select a circular area

function [grid_x,grid_y,FileNameBase,PathNameBase] = circ_grid(FileNameBase,
PathNameBase, im_grid);
```

```
title(sprintf('Pick three points on the circle in clockwise order at the
upper boundary of the sample.') )

[x(1,1),y(1,1)]=ginput(1);
hold on
plot(x(1,1),y(1,1),'+g')

[x(2,1),y(2,1)]=ginput(1);
plot(x(2,1),y(2,1),'+g')

[x(3,1),y(3,1)]=ginput(1);
plot(x(3,1),y(3,1),'+g')

xnew=x;
ynew=y;

% Calculate center between the 3 sorted points and the normal slope of the
vectors
slope12=-1/((ynew(2,1)-ynew(1,1))/(xnew(2,1)-xnew(1,1)));
slope23=-1/((ynew(3,1)-ynew(2,1))/(xnew(3,1)-xnew(2,1)));
center12(1,1)=(xnew(2,1)-xnew(1,1))/2+xnew(1,1);
center12(1,2)=(ynew(2,1)-ynew(1,1))/2+ynew(1,1);
center23(1,1)=(xnew(3,1)-xnew(2,1))/2+xnew(2,1);
center23(1,2)=(ynew(3,1)-ynew(2,1))/2+ynew(2,1);
% plot(center12(1,1),center12(1,2),'+b')
% plot(center23(1,1),center23(1,2),'+b')

if slope12==slope23
    return
end

% Calculate the crossing point of the two vectors
achsenabschnitt1=center12(1,2)-center12(1,1)*slope12;
achsenabschnitt2=center23(1,2)-center23(1,1)*slope23;
xdata=min(x):max(x);
ydata1=achsenabschnitt1+slope12*xdata;
ydata2=achsenabschnitt2+slope23*xdata;
% plot(xdata,ydata1,'-b')
% plot(xdata,ydata2,'-b')
xcross=(achsenabschnitt2-achsenabschnitt1)/(slope12-slope23);
ycross=slope12*xcross+achsenabschnitt1;
plot(xcross,ycross,'or')

% Calculate radius and plot circle
R=sqrt((xcross-xnew(1,1))*(xcross-xnew(1,1))+(ycross-ynew(1,1))*(ycross-
ynew(1,1)));
% ydata=ycross-sqrt(R*R-(xdata-xcross).*(xdata-xcross));
% plot(xdata,ydata,'-b')

% Calculate angle between vectors
xvector=[1;0];
x1vec(1,1)=xnew(1,1)-xcross;x1vec(2,1)=ynew(1,1)-ycross
x3vec(1,1)=xnew(3,1)-xcross;x3vec(2,1)=ynew(3,1)-ycross
alpha13=acos((dot(x1vec,x3vec))/(sqrt(x1vec'*x1vec)*sqrt(x3vec'*x3vec)))*180/
pi;
```

```
alpha01=acos((dot(xvector,x1vec))/(sqrt(x1vec'*x1vec)*sqrt(xvector'*xvector))
)*180/pi;
alpha03=acos((dot(xvector,x3vec))/(sqrt(xvector'*xvector)*sqrt(x3vec'*x3vec))
)*180/pi;
totalangle=alpha13;
minangle=alpha01;
maxangle=alpha03;
angldiv=abs(round(totalangle))*10;
anglstep=(totalangle/angldiv);
anglall(1:angldiv+1)=maxangle+anglstep*(1:angldiv+1)-anglstep;
xcircle(1:angldiv+1)=xcross+R*cos(-anglall(1:angldiv+1)/180*pi);
ycircle(1:angldiv+1)=ycross+R*sin(-anglall(1:angldiv+1)/180*pi);
plot(xcircle,ycircle,'-b')
drawnow

title(['Segment of circle spreads over ',num2str(totalangle),'°'])


% Accept the chosen circle, try again or give up

confirmcircselection = menu(sprintf('Do you want to use this circle as
basis?'),...
    'Yes','No, try again','Go back to grid-type selection');

if confirmcircselection==2
    close all
    imshow(im_grid,'truesize');
    circ_grid(FileNameBase, PathNameBase, im_grid);
end

if confirmcircselection==3
    close all
    gridtypeselection(FileNameBase, PathNameBase, im_grid);
end

if confirmcircselection==1

    prompt = {'Enter the number of intersections between markers on the
circle:'};
    dlg_title = 'Input for grid creation';
    num_lines= 1;
    def     = {'30'};
    answer = inputdlg(prompt,dlg_title,num_lines,def);
    angldiv = str2num(cell2mat(answer(1,1)));

    anglstep=(totalangle/angldiv);
    anglall(1:angldiv+1)=maxangle+anglstep*(1:angldiv+1)-anglstep;

    markerxpos(1:angldiv+1)=xcross+R*cos(-anglall(1:angldiv+1)/180*pi);
    markerypos(1:angldiv+1)=ycross+R*sin(-anglall(1:angldiv+1)/180*pi);

    plot(markerxpos,markerypos,'ob');

    % Pick the lower bound in the image
```

```
    title(sprintf('Pick three points lying on the circle in clockwise order.
The first and last one define the width of the raster') )

    [x(4,1),y(4,1)]=ginput(1);
    hold on
    plot(x(1,1),y(1,1),'+r')

    lowboundx=x(4,1);
    lowboundy=y(4,1);

    R2=sqrt((xcross-lowboundx(1,1))*(xcross-lowboundx(1,1))+(ycross-
lowboundy(1,1))*(ycross-lowboundy(1,1)));
    markerxposlb(1:angldiv+1)=xcross+R2*cos(-anglall(1:angldiv+1)/180*pi);
    markeryposlb(1:angldiv+1)=ycross+R2*sin(-anglall(1:angldiv+1)/180*pi);

    plot(markerxposlb,markeryposlb,'ob');

    prompt = {'Enter the number of intersections between the upper and lower
bound:'};
    dlg_title = 'Input for grid creation';
    num_lines= 1;
    def     = {'5'};
    answer = inputdlg(prompt,dlg_title,num_lines,def);
    Rdiv = str2num(cell2mat(answer(1,1)));

    Rstep=((R-R2)/Rdiv);
    Rall(1:Rdiv+1)=R2+Rstep*(1:Rdiv+1)-Rstep;

    grid_x=ones(Rdiv+1,angldiv+1)*xcross;
    grid_y=ones(Rdiv+1,angldiv+1)*ycross;
    A=Rall;
    B=cos(-anglall(1:angldiv+1)/180*pi);
    C=A'*B;
    grid_x=grid_x+Rall'*cos(-anglall(1:angldiv+1)/180*pi);
    grid_y=grid_y+Rall'*sin(-anglall(1:angldiv+1)/180*pi);

    close all
    imshow(im_grid,'truesize');
    hold on
    plot(grid_x,grid_y,'.b')

    title(['Selected grid has ',num2str(angldiv*Rdiv), ' rasterpoints'])    %
plot a title onto the image


    % Do you want to keep the grid?
    confirmselection = menu(sprintf('Do you want to use this grid?'),...
        'Yes','No, try again','Go back to grid-type selection');

    if confirmselection==1
        % Save settings and grid files in the image directory for
visualization/plotting later
        %         save settings.dat xspacing yspacing xmin_new xmax_new
ymin_new ymax_new -ascii -tabs
```

```
        save grid_x.dat grid_x -ascii -tabs
        save grid_y.dat grid_y -ascii -tabs
    end

    if confirmselection==2
        close all
        hold off
        imshow(im_grid,'truesize');
        circ_grid(FileNameBase, PathNameBase, im_grid);
    end

    if confirmselection==3
        gridtypeselection(FileNameBase, PathNameBase, im_grid);
    end

end


return



%--------------------------------
%

function [grid_x,grid_y,FileNameBase,PathNameBase] = rect_grid(FileNameBase,
PathNameBase, im_grid);

title(sprintf('Define the region of interest.  Pick (single click) a point in
the LOWER LEFT region of the gage section.\n  Do the same for a point in the
UPPER RIGHT portion of the gage section.'))

[x(1,1),y(1,1)]=ginput(1);
hold on
plot(x(1,1),y(1,1),'+b')

[x(2,1),y(2,1)]=ginput(1);
hold on
plot(x(2,1),y(2,1),'+b')

drawnow

xmin = min(x);
xmax = max(x);
ymin = min(y);
ymax = max(y);

lowerline=[xmin ymin; xmax ymin];
upperline=[xmin ymax; xmax ymax];
leftline=[xmin ymin; xmin ymax];
rightline=[xmax ymin; xmax ymax];

plot(lowerline(:,1),lowerline(:,2),'-b')
plot(upperline(:,1),upperline(:,2),'-b')
```

```
plot(leftline(:,1),leftline(:,2),'-b')
plot(rightline(:,1),rightline(:,2),'-b')

% closereq

cd(PathNameBase)

% Prompt user for grid spacing/resolution
prompt = {'Enter horizontal (x) resolution for image analysis [pixels]:', ...
        'Enter vertical (y) resolution for image analysis [pixels]:'};
dlg_title = 'Input for grid creation';
num_lines= 1;
def     = {'50','50'};
answer = inputdlg(prompt,dlg_title,num_lines,def);
xspacing = str2num(cell2mat(answer(1,1)));
yspacing = str2num(cell2mat(answer(2,1)));

% Round xmin,xmax and ymin,ymax "up" based on selected spacing
numXelem = ceil((xmax-xmin)/xspacing)-1;
numYelem = ceil((ymax-ymin)/yspacing)-1;

xmin_new = (xmax+xmin)/2-((numXelem/2)*xspacing);
xmax_new = (xmax+xmin)/2+((numXelem/2)*xspacing);
ymin_new = (ymax+ymin)/2-((numYelem/2)*yspacing);
ymax_new = (ymax+ymin)/2+((numYelem/2)*yspacing);

% Create the analysis grid and show user
[x,y] = meshgrid(xmin_new:xspacing:xmax_new,ymin_new:yspacing:ymax_new);
[rows columns] = size(x);
zdummy = 200.*ones(rows,columns);
imshow(FileNameBase)
title(['Selected grid has ',num2str(rows*columns), ' rasterpoints'])    %
plot a title onto the image
hold on;
plot(x,y,'+b')

grid_x=x;
grid_y=y;

% Do you want to keep the grid?
confirmselection = menu(sprintf('Do you want to use this grid?'),...
    'Yes','No, try again','Go back to grid-type selection');

if confirmselection==1
    % Save settings and grid files in the image directory for
visualization/plotting later
    save settings.dat xspacing yspacing xmin_new xmax_new ymin_new ymax_new -
ascii -tabs
    save grid_x.dat x -ascii -tabs
    save grid_y.dat y -ascii -tabs
    close all
    hold off
end

if confirmselection==2
```

```
    close all
    hold off
    imshow(im_grid,'truesize');
    rect_grid(FileNameBase, PathNameBase, im_grid);
end

if confirmselection==3
    close all
    hold off
    gridtypeselection(FileNameBase, PathNameBase, im_grid);
end
```

A.3 automate_image.m

The subroutine cross correlates the area within an active window, the size of which is preset by the user. The size is specified in the variable ‘corrsize’ (15 is the default value). The aforementioned region is cross correlated with similarly sized windows about points located in equivalent locations in the next image. When a maxima greater than a set threshold (0.4 is the default value) is detected in the cross correlation field, the location of the point corresponding to the maxima is updated as the position of the original point in the latter image. Depending on whether the object captured within the sequence is moving/deforming or not, the aforementioned position may or may not change. The procedure is illustrated in Fig. 11. The subroutine takes the ‘filenamelist.mat’, ‘gridx.dat’ and ‘gridy.dat’ as inputs and outputs ‘validx.dat’ and ‘validy.dat’ containing the corresponding positions of points within the grid.

```
function
[validx,validy]=automate_image(grid_x,grid_y,filenamelist,validx,validy);

% Code to start actual image correlation
% Programmed by Chris and Rob
% Last revision: 09/10/08

% The automation function is the central function and processes all markers
and
% images by the use of the matlab function cpcorr.m.
% Therefore the Current directory in matlab has to be the folder where
%  automate_image.m finds the filenamelist.mat, grid_x.dat and grid_y.dat as
well
% as the images specified in filenamelist.mat. Just type automate_image; and
% press ENTER at the command line of matlab.
% At first, automate_image.m will open the first image in the
filenamelist.mat and
% plot the grid as green crosses on top. The next step will need some time
since
% all markers in that image have to be processed for the first image. After
correlating
% image one and two the new raster positions will be plotted as red crosses.
On top
% of the image and the green crosses. The next dialog will ask you if you
want to
```

```
% continue with this correlation or cancel. If you press continue,
automate_image.m
% will process all images in the filenamelist.mat. The time it will take to
process
% all images will be plotted on the figure but can easily be estimated by
knowing the
% raster point processing speed (see processing speed).
% Depending on the number of images and markers you are tracking, this
process
% can take between seconds and days. For 100 images and 200 markers a decent
% computer should need 200 seconds. To get a better resolution you can always
% run jobs overnight (e.g. 6000 markers in 1000 images) with higher
resolutions.
% Keep in mind that CORRSIZE which you changed in cpcorr.m will limit your
% resolution. If you chose to use the 15 pixel as suggested a marker distance
of
% 30 pixel will lead to a full cover of the strain field. Choosing smaller
marker
% distances will lead to an interpolation since two neighboring markers share
% pixels. Nevertheless a higher marker density can reduce the noise of the
strain field.
% When all images are processed, automate_image will write the files
validx.mat,
% validy.mat, validx.txt and validy.txt. The text files are meant to store
the result in a
% format which can be accessed by other programs also in the future.


% exist('grid_x')
% exist('grid_y')
% exist('filenamelist')
% exist('validx')
% exist('validy')

% Load necessary files
if exist('grid_x')==0
    load('grid_x.dat')              % file with x position, created by
grid_generator.m
end
if exist('grid_y')==0
    load('grid_y.dat')              % file with y position, created by
grid_generator.m
end
if exist('filenamelist')==0
    load('filenamelist')            % file with the list of filenames to be
processed
end
resume=0;
if exist('validx')==1
    if exist('validy')==1
        resume=1;
        [Rasternum Imagenum]=size(validx);
    end
end
```

```
% Initialize variables
input_points_x=grid_x;
base_points_x=grid_x;

input_points_y=grid_y;
base_points_y=grid_y;

if resume==1
    input_points_x=validx(:,Imagenum);
    input_points_y=validy(:,Imagenum);
    inputpoints=1;
end

[row,col]=size(base_points_x);      % this will determine the number of
rasterpoints we have to run through
[r,c]=size(filenamelist);                   % this will determine the number
of images we have to loop through


% Open new figure so previous ones (if open) are not overwritten
h=figure;
imshow(filenamelist(1,:))           % show the first image
title('Initial Grid For Image Correlation (Note green crosses)')        % put
a title
hold on
plot(grid_x,grid_y,'g+')            % plot the grid onto the image
hold off

% Start image correlation using cpcorr.m
g = waitbar(0,sprintf('Processing images'));        % initialize the waitbar
set(g,'Position',[275,50,275,50])                                % set the
position of the waitbar [left bottom width height]
firstimage=1;

if resume==1
    firstimage=Imagenum+1
end

for i=firstimage:(r-1)              % run through all images


    tic             % start the timer
    base = uint8(mean(double(imread(filenamelist(i,:))),3));            %
read in the base image ( which is always  image number one. You might want to
change that to improve correlation results in case the light conditions are
changing during the experiment
    input = uint8(mean(double(imread(filenamelist((i+1),:))),3));       %
read in the image which has to be correlated

    input_points_for(:,1)=reshape(input_points_x,[],1);         % we reshape
the input points to one row of values since this is the shape cpcorr will
accept
    input_points_for(:,2)=reshape(input_points_y,[],1);
    base_points_for(:,1)=reshape(base_points_x,[],1);
    base_points_for(:,2)=reshape(base_points_y,[],1);
```

```
    input_correl(:,:)=cpcorr1(input_points_for, base_points_for, input,
base);           % here we go and give all the markers and images to process
to cpcorr.m which is a function provided by the matlab image processing
toolbox
    input_correl_x=input_correl(:,1);                                    %
the results we get from cpcorr for the x-direction
    input_correl_y=input_correl(:,2);                                    %
the results we get from cpcorr for the y-direction



    validx(:,i)=input_correl_x;
% lets save the data
    savelinex=input_correl_x';
    dlmwrite('resultsimcorrx.txt', savelinex , 'delimiter', '\t', '-append');
% Here we save the result from each image; This may not work in MATLAB 6.5

    validy(:,i)=input_correl_y;
    saveliney=input_correl_y';
    dlmwrite('resultsimcorry.txt', saveliney , 'delimiter', '\t', '-append');

    waitbar(i/(r-1))
% update the waitbar

    % Update base and input points for cpcorr.m
    base_points_x=grid_x;
    base_points_y=grid_y;
   % the last two lines are activated if steady state is known to prevail in
the deformation experiment that is captured in the sequence of images.
   % However, if this is not the case the following two lines are activated
   %base_points_x=input_correl_x;
   %base_points_y=input_correl_y;
    input_points_x=input_correl_x;
    input_points_y=input_correl_y;

    imshow(filenamelist(i+1,:))                    % update image
    hold on
    plot(grid_x,grid_y,'.g')                               % plot start
position of raster
    plot(input_correl_x,input_correl_y,'.r')        % plot actual postition
of raster
    hold off
    drawnow
    time(i)=toc;                                                % take time
    estimatedtime=sum(time)/i*(r-1);            % estimate time to process
    title(['# Im.: ', num2str((r-1)),'; Proc. Im. #: ', num2str((i)),'; #
Rasterp.:',num2str(row*col), '; Est. Time [s] ',
num2str(round(estimatedtime)), ';  Elapsed Time [s] ',
num2str(round(sum(time)))]);    % plot a title onto the image
    drawnow

end

close(g)
% close all
```

```
% save

save time.dat time -ascii -tabs
save validx.dat validx -ascii -tabs
save validy.dat validy -ascii –tabs
```

A.4 vonmisesarea.m

The subroutine process results from automate_image.m to find the displacement field in the ROI. The subroutine subsequently differentiates the displacement field with respect to time and space to find the velocity vector field and strain rate fields, respectively. The latter part of the subroutine finds the line or area average of the strain rate field as specified, along a selected line or within a selected polygon, respectively. In order to differentiate the displacement field with respect to time, Δt = time between two successive images in the high speed sequence. Δt is saved in the variable 'framerate'.

```
% this calculates the strains based on the results of matlab DIC software
clc
clear
close all

load filenamelist.mat
%image=filenamelist(1,:);
image=filenamelist(1,:);
fig=figure;
imshow(imread(image));
hold on
load grid_x.dat
load grid_y.dat
load validx.dat
load validy.dat
plot(grid_x,grid_y,'.g');
%drawnow
%keyboard

%plot(validx,validy,'.r');

choice='n';
selection = menu(sprintf('Do you want to exclude points from strain
calculations ?'),'Yes','No');
if selection==1
    choice='y';

    if exist('matlab.mat')==2
        load 'matlab.mat';
        siz_excluded=size(excluded);
        for r=1:siz_excluded(1,1)
            for c=1:siz_excluded(1,2)
```

```
                if excluded(r,c)==1
                    plot (grid_x(r,c),grid_y(r,c),'.yellow');
                end
            end
        end



        selection = menu(sprintf('An excluded points array has been found. Do
you want to exclude more points ?'),'Yes','No');
        if selection==2
            choice='n';
        end
    else
        excluded=zeros(size(grid_x));
    end

end

limit=1;

while choice=='y'
    a(limit,:,:,:,:)=getrect(fig);

    % This highlights the points
    [excluded_x1]=find(grid_x(1,:)>a(limit,1));
    [excluded_x2]=find(grid_x(1,excluded_x1)<a(limit,1)+a(limit,3));

    [excluded_y1]=find(grid_y(:,1)>a(limit,2));
    [excluded_y2]=find(grid_y(excluded_y1,1)<a(limit,2)+a(limit,4));
    selection = menu(sprintf('Do you want to exclude this selection
?'),'Yes','No');
    if selection==1

plot(grid_x(excluded_y1(excluded_y2),excluded_x1(excluded_x2)),grid_y(exclude
d_y1(excluded_y2),excluded_x1(excluded_x2)),'.yellow');
        excluded(excluded_y1(excluded_y2),excluded_x1(excluded_x2))=1;

%von_mises_strain(excluded_y1(excluded_y2),excluded_x1(excluded_x2))=0;
    end
    clear excluded_x1 excluded_x2 excluded_y1 excluded_y1

   selection = menu(sprintf('Do you want to exclude more points from strain
calculations ?'),'Yes','No');
    if selection == 2
        choice='n';
    else
        limit=limit+1;
    end

end
```

```
h=grid_x(1,2)-grid_x(1,1);
k=grid_y(2,1)-grid_y(1,1);


siz=size(grid_x);
size_validx=size(validx);
frame_rate= 1;

l=1;
von_mises_strain=zeros(siz(1,1)-1,siz(1,2)-1);
for image_pair=1:size_validx(1,2)
    clear displacement strain_tensor principle_strain
    strain_tensor=zeros(siz(1,1)-1,siz(1,2)-1,3);
    principle_strain=zeros(siz(1,1)-1,siz(1,2)-1,3);
%     displacement(:,:,2)=reshape(validx(:,image_pair),siz)-grid_x;
%     displacement(:,:,1)=reshape(validy(:,image_pair),siz)-grid_y;
    displacement(:,:,2)=validx-grid_x;
    displacement(:,:,1)=validy-grid_y;

    for row=1:siz(1,1)-1
        for col=1:siz(1,2)-1


        strain_tensor(row,col,1)=(displacement(row,col+1,2)-
displacement(row,col,2))/h;
        strain_tensor(row,col,2)=(displacement(row+1,col,1)-
displacement(row,col,1))/k;
        strain_tensor(row,col,3)=1/2*((displacement(row,col+1,2)-
displacement(row,col,2))/k+((displacement(row+1,col,1)-
displacement(row,col,1))/h));


principle_strain(row,col,1)=(strain_tensor(row,col,1)+strain_tensor(row,col,2
))/2+sqrt(((strain_tensor(row,col,1)-
strain_tensor(row,col,2))/2)^2+strain_tensor(row,col,3)^2);

principle_strain(row,col,2)=(strain_tensor(row,col,1)+strain_tensor(row,col,2
))/2-sqrt(((strain_tensor(row,col,1)-
strain_tensor(row,col,2))/2)^2+strain_tensor(row,col,3)^2);


von_mises_strain(row,col)=von_mises_strain(row,col)+sqrt((2/3)*(principle_str
ain(row,col,1)^2+principle_strain(row,col,2)^2));

        if image_pair==size_validx(1,2)
            vonm(l,1)=grid_x(row,col);
            vonm(l,2)=grid_y(row,col);
            if excluded(row,col)==0

vonm(l,3)=(von_mises_strain(row,col)/size_validx(1,2))/frame_rate;
                vonm(l,4)=strain_tensor(row,col,3)/frame_rate;
            else
                vonm(l,3)=0;
                vonm(l,4)=0;
```

```
            end
             l=l+1;


        end

        end

    end

end


%figure;
%image_=imread(image);
%imshow(image_(min(grid_y(:,1)):max(grid_y(:,1)),min(grid_x(1,:)):max(grid_x(
1,:))));
[X
Y]=meshgrid(min(vonm(:,1)):1:max(vonm(:,1)),min(vonm(:,2)):1:max(vonm(:,2)));
Z=griddata(vonm(:,1),vonm(:,2),vonm(:,3),X,Y,'cubic',{'QJ'});
%shear_strain=griddata(vonm(:,1),vonm(:,2),vonm(:,4),X,Y,'cubic');
%figure;
% Z=fliplr(Z);
close all

surf(Z);


%axis([0 max(size(Z)) 0 max(size(Z)) min(min(Z)) max(max(Z)) min(min(Z))
max(max(Z))]);
view(0,90);

selection = menu(sprintf('Do you want area averaging or line averaging
?'),'area','line');

if selection==2
    [x y]=ginput (2);
    %hold on
    % this calculate the average in the zone of principal deformation
    y=round(y);
    x=round(x);
    slope=(y(2)-y(1))/(x(2)-x(1));
    %max_cols_Z=zeros(1,siz_Z(1,2));
    num=find(x==min(x));
    min_x=min(x);
    max_x=max(x);
    avg_strain_rate=0;
    prev_x=min_x;
    prev_y=y(num);
    for col=min_x+1:max_x
        dist=sqrt((round(y(num)+slope*(col-min_x))-prev_y)^2+(col-prev_x)^2);
        avg_strain_rate=avg_strain_rate+((Z(round(y(num)+slope*(col-
min_x)),col)+Z(prev_y,prev_x))/2)*dist;
```

```
        % plot3(col,round(y(num)+slope*(col-min_x)),2000);
        prev_y=round(y(num)+slope*(col-min_x));
        prev_x=col;
    end
else
    if selection ==1
        sides=1;
        poly=zeros(10,0);
        [x y]=ginput(1);
        poly(sides,1)=x;
        poly(sides,2)=y;
        ch=1;
        while ch==1
            sides=sides+1;
            [x y]=ginput(1);
            poly(sides,1)=x;
            poly(sides,2)=y;
            line([poly(sides,1) poly(sides-1,1)], [poly(sides,2) poly(sides-
1,2)], [2 2],'linewidth',2,'color','red');
            ch=menu(sprintf('do you want to continue ?'),'yes','no');
        end
        line([poly(sides,1) poly(1,1)], [poly(sides,2) poly(1,2)],[2
2],'linewidth',2,'color','red');
        sides=sides+1;
        poly(sides,1)=poly(1,1);
        poly(sides,2)=poly(1,2);
        [X Y]=meshgrid(1:1:size(Z,2),1:1:size(Z,1));

        IN=inpolygon(X,Y,poly(1:sides,1),poly(1:sides,2));
        Z=reshape(Z,size(Z,1)*size(Z,2),1);
        IN=reshape(IN,1,size(IN,1)*size(IN,2));
        avg_strain_rate=IN*Z;
        avg_strain_rate=avg_strain_rate/max(size(find(IN==1)));


    end
end
[x y]=ginput(2);
for image_pair=1:size_validx(1,2)

displacement(:,:,2)=displacement(:,:,2)+reshape(validx(:,image_pair),siz)-
grid_x;

displacement(:,:,1)=displacement(:,:,1)+reshape(validy(:,image_pair),siz)-
grid_y;
end
displacement(:,:,2)=displacement(:,:,2)/size_validx(1,2);
displacement(:,:,1)=displacement(:,:,1)/size_validx(1,2);

x_original(1)=grid_x(round(size(grid_y,2)*y(1)/max(max(Y))),round(size(grid_x
,2)*(1-(x(1)/max(max(X))))));
y_original(1)=grid_y(round(size(grid_y,2)*y(1)/max(max(Y))),round(size(grid_x
,2)*(1-(x(1)/max(max(X))))));
figure
imshow(imread(image));
hold on
```

```
plot(x_original(1),y_original(1),'.');
U(1)=displacement(round(size(grid_y,2)*y(1)/max(max(Y))),round(size(grid_x,2)
*(1-(x(1)/max(max(X))))),2);
V(1)=displacement(round(size(grid_y,2)*y(1)/max(max(Y))),round(size(grid_x,2)
*(1-(x(1)/max(max(X))))),1);
x_original(2)=grid_x(round(size(grid_y,2)*y(2)/max(max(Y))),round(size(grid_x
,2)*(1-(x(2)/max(max(X))))));
y_original(2)=grid_y(round(size(grid_y,2)*y(2)/max(max(Y))),round(size(grid_x
,2)*(1-(x(2)/max(max(X))))));

plot(x_original(2),y_original(2),'.');

U(2)=displacement(round(size(grid_y,2)*y(2)/max(max(Y))),round(size(grid_x,2)
*(1-(x(2)/max(max(X))))),2);
V(2)=displacement(round(size(grid_y,2)*y(2)/max(max(Y))),round(size(grid_x,2)
*(1-(x(2)/max(max(X))))),1);
quiver(x_original,y_original,U,V);
U=U/frame_rate;
V=V/frame_rate;
channel_width=2;
[x y]=ginput(2);
U=U*channel_width/sqrt((x(2)-x(1))^2 + (y(2)-y(1))^2);
V=V*channel_width/sqrt((x(2)-x(1))^2 + (y(2)-y(1))^2);
Vel_in=[U(1) V(1)];
Vel_out=[U(2) V(2)];
Vs=Vel_out-Vel_in;
sqrt(Vs*transpose(Vs))
```

APPENDIX B

LABVIEW IMPLEMENTATION OF *in-situ* MICROMACHINING DEVICE

The *in-situ* micromachining device was fabricated in house and tested within a FEI Philips XL 30 Scanning Electron Microscope (SEM). The device was operated through an electrical feed through which was installed in a port of the SEM. The feed through consisted of 52 vacant pins capable of carrying 0.1 A at 200 V. As each phase of the stepper motor was rate at 0.3 A, the current for each phase was split into three parts to prevent the feed through from overheating. Fig. 17 shows the block diagram of the setup used for controlling the micromachining device. A LABVIEW implementation was used to control the *n-situ* device; this section provides a detailed description of the implementation.

B.1 TWO AXIS VECTOR CONTROL

The in-built LABVIEW code ‘two_axis_vector_control.vi’ was used to control the stepper motors simultaneously. The Block code is shown in Fig. 43. Speed was converted from physical units to corresponding LABVIEW units before running the motor (50 μm/s was equivalent to 300 units in LABVIEW). The ‘two_axis_vector_control.vi’ was run from within a loop when

repetitive machining passes had to be performed. The LABVIEE block diagram for doing this is shown in Fig. 44.

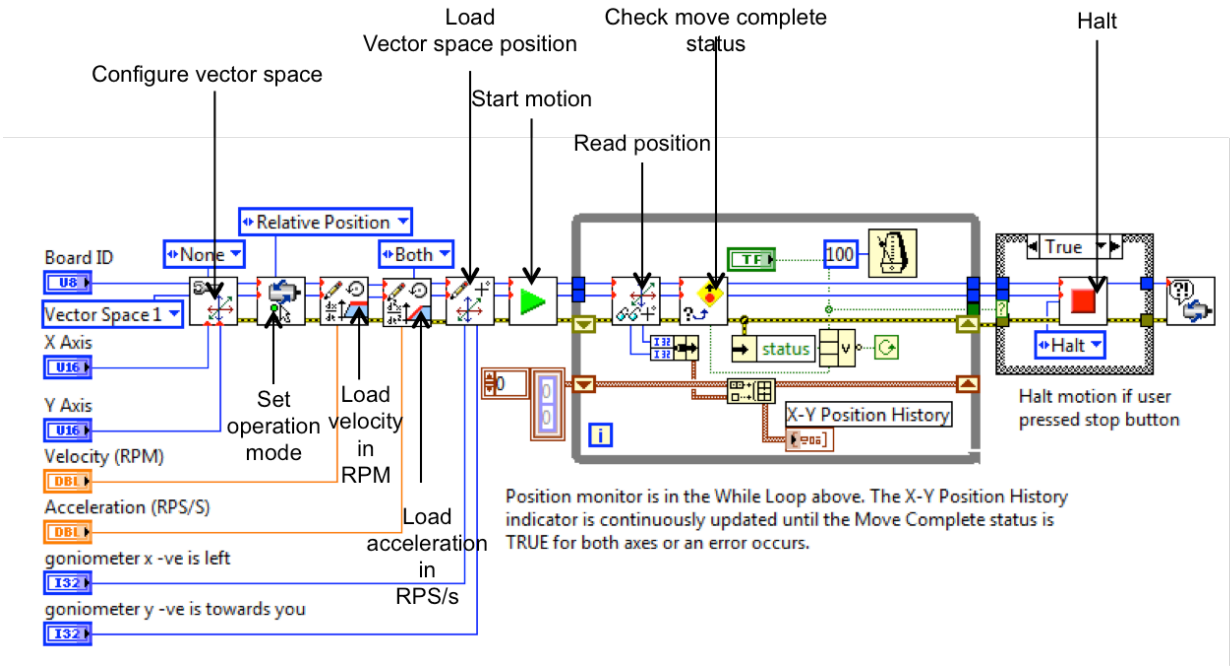

Figure 43: Labview vi block code for performing two axis vector motion control.

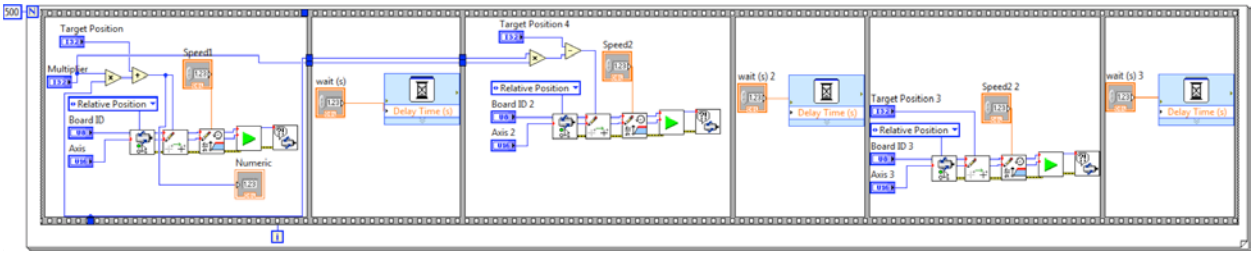

Figure 44: Two axis motion within a loop.

B.2 ACQUIRING FORCES FROM LOAD CELL

Machining (cutting, thrust forces and out of plane) forces were acquired using a strain gauge load cell that was installed on the micromachining device. Fig. 45 shows the LABVIEW block diagram for doing this. The load cell exhibited an offset, which was removed using the vi for display purposes. However, raw data was recorded and any offset was eventually carefully analyzed before discarding. The data was recorded in a native TDMS format (by LABVIEW) and was converted to ASCII format using the LABVIEW block code given in Fig. 46.

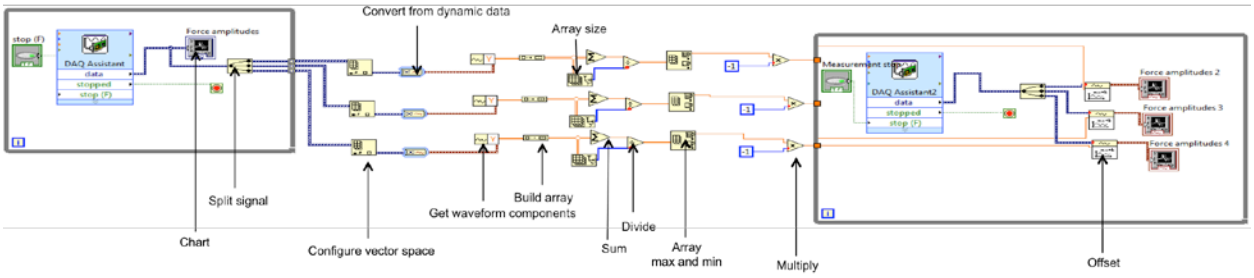

Figure 45: Labview block code for interfacing with load cell.

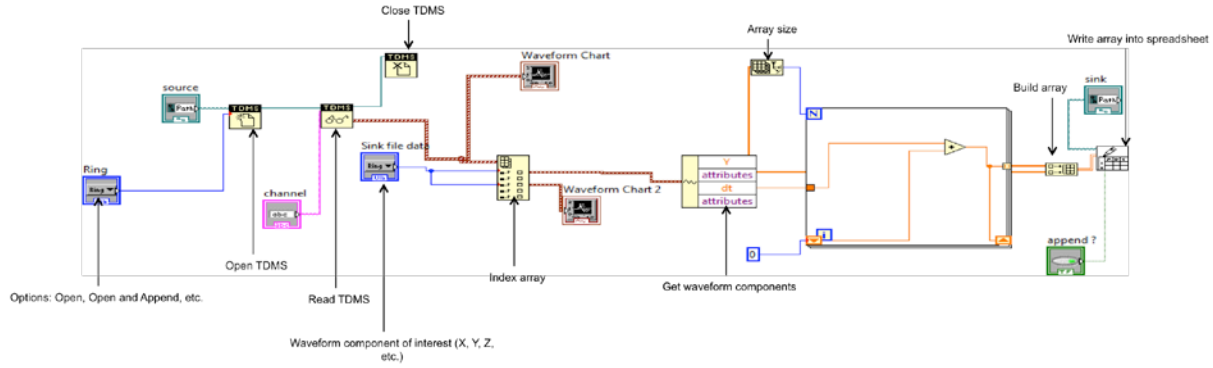

Figure 46: Labview block code for converting force data from TDMS to readable format.

BIBLIOGRAPHY

[1] E. Nes. Modelling of work hardening and stress saturation in FCC metals. *Progress in Material Science*, 41(3):129-193, 1997.

[2] S. Abolghasem, S. Basu, S. Shekhar, J. Cai, M.R. Shankar. Mapping subgrain sizes resulting from severe simple shear deformation. *Acta Materialia*, 60:376-386, 2012.

[3] P. Landau, R.Z. Shneck, G. Makov, A. Venkert. Evolution of dislocation patterns in FCC metals. *IOP Conference Series: Material Science and Engineering*, 3:012004, 2009.

[4] D.A. Hughes, N. Hansen. Microstructure and strength of nickel at large strains. *Acta Materialia*, 48:2985-3004, 2000.

[5] D.A. Hughes, N. Hansen. High angle boundaries formed by grain subdivision mechanism. *Acta Materialia*, 45(9):3871-3886, 1997.

[6] D.K. Wilsdorf, N. Hansen. Geometrically Necessary, Incidental and Subgrain Boundaries. *Scripta Metallurgica*, 25:1557-1562, 1991.

[7] F.J. Humphreys, M. Hatherly, *Recrystallization and related annealing phenomena*, Elsevier, 2004.

[8] R.D. Doherty, D.A. Hughes, F.J. Humphreys, J.J. Jonas, D.J. Jensen, M.E. Kassner, W.E. King, T.R. McNelley, H.J. McQueen, A.D. Rollett. Current issues in recrystallization: a review. *Material Science and Engineering : A*, 238:219-274, 1997.

[9] S. Abolghasem, S. Basu, M.R. Shankar. Quantifying the progression of dynamic recrystallization in severe shear deformation at high strain rates. *Journal of Materials Research*, 28:2056-2069, 2013.

[10] U.F. Kocks, C.N. Tom´e, H.R. Wenk, *Texture and Anisotropy: Preferred Orientations in Polycrystals and their Effect on Materials Properties*, Cambridge University Press, 2000.

[11] S. Li, I.J. Beyerlein, D.J. Alexander, S.C. Vogel. Texture evolution during multi-pass equal channel angular extrusion of copper: Neutron diffraction characterization and polycrystal modelling. *Acta Materialia*, 53:2111-2125, 2005.

[12] S. Li, I.J. Beyerlein, M.A.M. Bourke. Texture formation during equal channel angular extrusion of FCC and BCC materials: comparison with simple shear. *Material Science and Engineering : A*, 394(1-2):66-77, 2005.

[13] J.R. Greer, J.T.M.D. Hosson. Plasticity in small-sized metallic systems: Intrinsic versus extrinsic size effect. *Progress in Material Science*, 56:654-724, 2011.

[14] M.D. Uchic, D.M. Dimiduk, J.N. Florando, W.D. Nix. Sample Dimensions Influence Strength and Crystal Plasticity. *Science*, 305:986-989, 2004.

[15] D.M. Dimiduk, M.D. Uchic, T.A. Parthasarathy. Size-affected single-slip behavior of pure nickel microcrystals. *Acta Materialia*, 53:4065-4077, 2005.

[16] S. Brinckmann, J.Y. Kinm, J.R. Greer. Fundamental differences in mechanical behavior between two types of crystals at the nanoscale. *Physical Review Letters*, 100:155502-4, 2008.

[17] F.F. Csikor, C. Motz, D. Weygand, M. Zaiser, S. Zapperi. Dislocation Avalanches, Strain Bursts, and the Problem of Plastic Forming at the Micrometer Scale. *Science*, 318:251-254, 2007.

[18] T.A. Parthasarathy, S.I. Rao, D.M. Dimiduk, M.D. Uchic, D.R. Trinkle. Contribution to size effect of yield strength from the stochastics of dislocation source lengths in finite samples. *Scripta Materialia*, 56:313-316, 2007.

[19] C. Motz, T. Schoberl, R. Pippan. Mechanical properties of micro-sized copper bending beams machined by the focused ion beam technique. *Acta Materialia*, 53:4269-4279, 2005.

[20] D.M. Norfleet, D.M. Dimiduk, S.J. Polasik, M.D. Uchic, M.J. Mills. Dislocation structures and their relationship to strength in deformed Nickel microcrystals. *Acta Materialia*, 56(13):2988-3001, 2008.

[21] A.S. Budiman, S.M. Han, J.R. Greer, N. Tamura, J.R. Patel, W.D. Nix. A search for evidence of strain gradient hardening in Ai submicron pillars under uniaxial compression using synchrotron X-rat microdiffraction. *Acta Materialia*, 56:602-608, 2008.

[22] R. Maaß, M.D. Uchic. In-situ characterization of the dislocation-structure evolution in Ni micro-pillars. *Acta Materialia*, 60:1027-1037, 2012.

[23] N.A. Fleck, G.M. Muller, M.F. Ashby, J.W. Hutchinson. Strain gradient plasticity: Theory and experiment. *Acta Matallurgica Materialia*, 42(2):475-487, 1993.

[24] W.D. Nix, H. Gao. Indentation size effects in crystalline materials: a law for strain gradient plasticity. *Journal of Mechanics and Physics of Solids*, 46(3):411-425, 1998.

[25] P.J. Apps, J.R. Bowen, P.B. Prangnell. The effect of coarse second-phase particles on the rate of grain refinement during severe deformation processing. *Acta Materialia*, 51:2811-2822, 2003.

[26] M. Ravi Shankar, S. Chandrasekar, A. H. King, W.D. Compton. Microstructure and Stability of Nanocrystalline Aluminum 6061 Created by Large Strain Machining. *Acta Materialia*, 53:4781-4793, 2005.

[27] S. Basu, M.R. Shankar. Microstructure Evolution during Severe Shear Deformation at Small Length-Scales. *Scripta Materialia*, 72-73:51-54, 2013.

[28] M.R. Shankar, B.C. Rao, S. Lee, S. Chandrasekar, A.H. King, W.D. Compton. Severe plastic deformation (SPD) of Titanium at near-ambient temperature. *Acta Materialia*, 54:3691-3700, 2006.

[29] S. Basu, S. Abolghasem, M.R. Shankar. Mechanics of intermittent plasticity punctuated by fracture during shear deformation of Mg alloys at near ambient temperatures *Metallurgical and Material Transactions A*, 44:4558-4566, 2013.

[30] R. Calistes, S. Swaminathan, T.G. Murthy, C. Huang, C. Saldana, M.R. Shankar, S. Chandrasekar. Controlling gradation of surface strains and nanostructuring by large-strain machining. *Scripta Materialia*, 60:17-20, 2009.

[31] P.L.B. Oxley, W.F. Hastings. Predicting the strain rate in the zone of intense shear in which the chip is formed in machining from the dynamic flow stress properties of the work material and the cutting conditions. *Proceedings of Royal Society of London A*, 356:395-410, 1977.

[32] B.F.V. Turkovich, J.T. Black. Micro-machining of copper and aluminum crystals. *Journal of Engineering for Industry*, B-92(1):130-134, 1970.

[33] S. Ramalingam, J.T. Black. An electron microscopy study of chip formation. *Metallurgical Transactions*, 4:1103-1112, 1973.

[34] S. Shekhar, S. Abolghasem, S. Basu, J. Cai, M.R. Shankar. Effect of severe plastic deformation in machining elucidated via rate-strain-microstructure mappings. *Journal of Manufacturing Science and Engineering*, 134:013008-013011, 2012.

[35] I. Groma, A. Borbely. Variance method for the evaluation of particle size and dislcoation density from x-ray Bragg peaks. *Applied Physics Letters*, 79(12):1772-1774, 2001.

[36] R. Hielscher, H. Schaeben. A novel pole figure inversion method: specification of the MTEX algorithm. *Journal of Applied Crystallography*, 41(6):1024-1037, 2008.

[37] I.J. Beyerlein, R.A. Lebensohn, C.N. Tom´e. Modeling texture and microstructural evolution in the equal channel angular extrusion process. *Material Science and Engineering: A*, 345:122-138, 2003.

[38] R.A. Lebensohn, C.N. Tom´e. A self consistent anisotropic approach for simulation of plastic deformation and texture development of polycrystals: application to Zirconium alloys. *Acta Matallurgica*, 41(9):2611-2624, 1993.

[39] C.N. Tomé, R.A. Lebensohn. Manual for Code Visco-Plastic Self-Consistent. 7c, 2010.

[40] C.N. Tom´e, G.R. Canova, U.F. Kocks, N. Christodoulou, J.J. Jonas. The relation between macroscopic and microscopic strain hardening in F.C.C polycrystals. *Acta Matallurgica*, 32(10):1637-1653, 1984.

[41] S. Li, I.J. Beyerlein, M.A.M. Bourke. Texture formation during equal channel angular extrusion of fcc and bcc materials: comparison with simple shear. *Material Science and Engineering: A*, 394(1-2):66-77, 2005.

[42] M.C. Shaw, *Metal Cutting Principles*, Oxford University Press, Inc., New York, 2005.

[43] A.H. Adibi-Sedeh, V. Madhavan, B. Bahr. Extension of Oxley's analysis of machining to use different material models. *Transactions of ASME*, 125:656-666, 2003.

[44] G.R. Johnson, W.H. Cook. A constitutive model and data for metals subjected to large strains, high strain rates and high termperatures. *Proceedings of seventh international symposium on ballistics, The Hague, The Netherlands*, 1983.

[45] L.S. To´th, Y. Estrin, R. Lapovok, C. Gu. A model of grain fragmetation based on lattice curvature. *Acta Materialia*, 58:1782-1794, 2010.

[46] C.F. Gu, L.S. To´th, M. Azraghi, C.H.J. Davies. Effect of strain path on grain refinement in severely plastically deformed copper. *Scripta Materialia*, 64:284-287, 2011.

[47] D.A. Hughes, N. Hansen. High angle boundaries formed by grain subdivision mechanisms. *Acta Materialia*, 45(9):3871-3886, 1996.

[48] Q. Yu, L. Qi, R.K. Mishra, J. Li, A.M. Minor. Reducing deformation anisotropy to achieve ultrahigh strength and ductility in Mg at the nanoscale. *Proceedings of the National Academy of Sciences*, 110(33):13289-13293, 2013.

[49] C. Eberl, Digital Image Correlation & Tracking Example Files and Slides, Mathworks, 2006.

[50] R.K.R. Yarlagadda, *Analog and Digital Signals and Systems*, Springer, 2010.